1. Report No. 425	**2. Government Accession No.**	**3. Recipient's Catalog No.**

4. Title and Subtitle
Improve Highway Safety by Reducing the Risks of Landslides (Phase 1)

5. Report Date
July 31, 2024

6. Performing Organization Code
.

7. Author(s)
Zhuping Sheng, Ph.D. (https://orcid.org/0000-0001-8533-527x)
Oludare Owolabi, D,Sc. (https://orcid.org/0000-0002-1958-6430)
Yi Liu, D. Eng. (https://orcid.org/0000-0002-6861-2914)

8. Performing Organization Report No.
.

9. Performing Organization Name and Address
Department of Civil and Environmental Engineering, Morgan State University, 1700 E. Cold Spring Ln, Baltimore, MD 21251

10. Work Unit No.

11. Contract or Grant No.
Federal Grant No. 69A3552344811

12. Sponsoring Agency Name and Address
Safety21 University Transportation Center
Carnegie Mellon University
5000 Forbes Avenue
Pittsburgh, PA 15213

13. Type of Report and Period Covered
Final Report (July 1, 2023-June 30, 2024)

14. Sponsoring Agency Code
USDOT

15. Supplementary Notes
Conducted in cooperation with the U.S. Department of Transportation.

16. Abstract

To prevent landslides hazards, multiple approaches were integrated to develop a framework for detecting and monitoring slope stability and assessing landslides risks along the state highways and roads. In Phase 1, field investigation and laboratory tests were initiated to gain a better understanding of hydrological and mechanical properties of soils or rocks and slope characteristics. LiDAR and InSAR data were employed to detect and characterize landslides. Precipitation as one of major triggering factors is simulated with numerical models and then used in the slope instability analysis. Physical models for slope stability analysis and their applications in risk assessment of landslides were reviewed and summarized to lay a foundation for further analysis in the next phase. At the end an initial assessment of economic impacts of landslides, both direct and indirect costs were included.

17. Key Words
Landslides, Precipitation, Slope Stability, Geotechnical Engineering, Soil Tests, Light Detection and Ranging (LiDAR), Interferometric Synthetic Aperture Radar (InSAR), Economic Analysis, Risk Assessment

18. Distribution Statement
No restrictions.

19. Security Classif. (of this report) NONE	**20. Security Classif. (of this page)** NONE	**21. No. of Pages** 161	**22. Price** Refers to the price of the report. Leave blank unless applicable.

Form DOT F 1700.7 (8-72)

US DOT National
University Transportation Center for Safety

Improve Highway Safety by Reducing the Risks of Landslides (Phase 1)

Zhuping Sheng, Ph.D. (https://orcid.org/0000-0001-8533-527x)

Oludare Owolabi, Ph.D. (https://orcid.org/0000-0002-1958-6430)

Yi Liu, D. Eng. (https://orcid.org/0000-0002-6861-2914)

FINAL RESEARCH REPORT – July 30, 2024

Contract # 1080468-477269

Contents

Chapter 1

1. Introduction

Geologic hazards including slope failures, landslides, mudflows, debris flows, etc. and hydrological hazards related to floods and stormwater surge can be destructive to transportation infrastructure and threaten property and human life along the highway and roads. Landslides alone cause thousands of deaths and many billions of dollars in damage every year. Therefore, there is a great need in advancing our knowledge in slope instability and failure risks and developing technologies in detecting and monitoring, and preventing landslides, in turn sustaining safety of transportation infrastructure and system operations in changing environment.

As member of the National University Transportation Center (UTC) – Safety 21 led by Carnegie Mellon University, Morgan State University team proposes a multi-phase project focusing on safety of transportation infrastructure systems by preventing geohazard, specifically slope failure and landslides and minimizing impacts of geohazard. This project will employ an integrated approach of geotechnical and AI/Machine Learning methods for assessing conditions of geotechnical assets, such as cut slopes and embankment of the DOT/SHA and delineating landslides and high-risk areas.

This report summaries research findings of the Phase 1 of project titled Improve Highway Safety by Reducing the Risks of Landslides, sponsored by National UTC – Safety 21 program. The report is organized in the following order. We provide a brief background about the project. We follow with field and lab investigation approaches. We then introduce applications of LiDAR and InSAR data in detection and characterization of landslides. Precipitation, one of major triggering factors is simulated with numerical model and used in the slope instability analysis. We then provide a review of physical models for slope stability analysis and their applications in risk assessment of landslides. At the last we introduced an initial assessment of economic impacts.

Chapter 2

2. Background

2.1 Landslides

Geologic hazards, such as land subsidence and earth fissures, landslides, and earthquakes, etc. and hydrological hazards, such as floods and stormwater surge owing to extreme weather events (tropical storms, hurricanes, tornadoes, etc.), compounding with sea-level rising due to global warming and climate change, have caused great impacts on transportation infrastructure and traffic, in turn resulting in great economic damages. Landslides are among the most devastating and costly natural disasters, causing thousands of deaths and many billions of dollars in damages annually [1 – 3].

The majority of landslides are precipitation-triggered [4] even though they occur over a broad range of lithological, climatological, and hydrological conditions, and land use types [5]. However, for most precipitation-triggered landslides, other complex atmospheric, surface, and subsurface conditions also play a role in slope failure by increasing the effects of downgradient forces and/or reducing the strength of the underlying slope soils/rocks [6, 7]. the effect of precipitation from these confounding factors is thus essential both for enhancing fundamental understanding of landslides and for evaluating the impact of climate change on slope failure.

2.2 Landslides detection and warning smart system framework

We noted that it is common practice in many regions around the world to create an inventory of landslide, debris flow and/or slope failure occurrence. In addition, many studies have attempted to quantify the likelihood of the occurrence of landslides or identify areas that are susceptible to slope failures or instability, e.g., landsides susceptibility (LS) analysis based on GIS models and machine learning models [8]. MDOT/SHA manages an extensive portfolio of geotechnical assets, including slopes, embankments, and ground modifications, along the State of Maryland's roadway infrastructure. Its geotechnical asset management plan (AMP) establishes MDOT SHA's asset class strategy with a robust plan to guide infrastructure decisions; optimize the total cost of ownership; and meet performance, reliability, and risk objectives [9]. With MDOT/SHA sponsorship, MSU and Carnegie University initiated a project for incorporating precipitation data into the geotechnical asset management.

With additional support from National UTC Safety 21 program, Morgan State University team proposed a multi-phase (multi-year) project focusing on safety of transportation infrastructure systems by preventing geohazard, specifically slope failure and landslides and minimizing impacts of geohazard. This project will employ an integrated approach of geotechnical and AI/Machine Learning methods for assessing conditions of geotechnical assets, such as cut slopes and embankment of the DOT/SHA and delineating landslides and high-risk areas. Figure 2.1 shows a framework for landslides detection and monitoring smart system. It will be built on GIS platform.

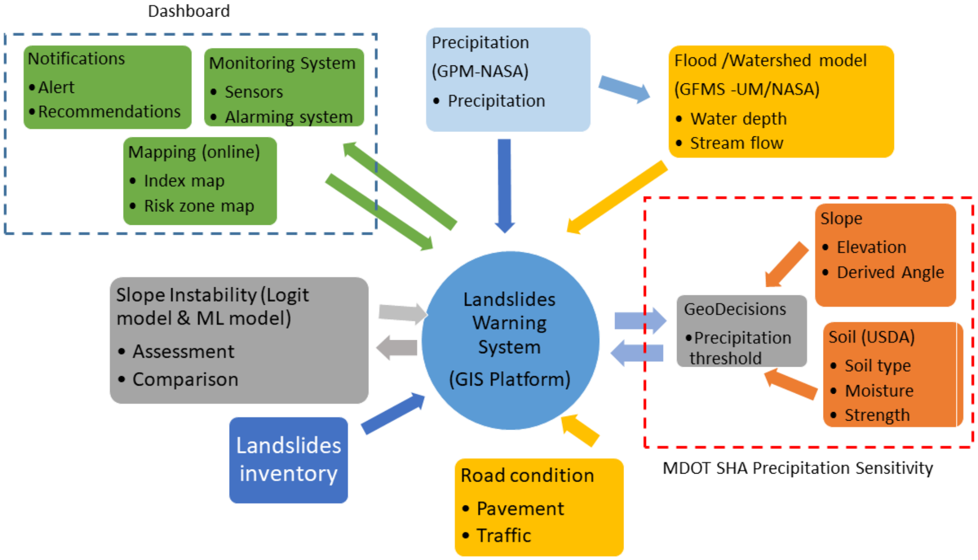

Figure 2.1: Framework for landslides risk assessment and monitoring smart system.

2.3 Objectives of Studies

This project is unique by integrating geotechnical and machine learning approaches in assessing slope instability and risk of landslides and mapping high-risk areas. This project is built upon ongoing project sponsored by Maryland Department of Transportation/State Highway Administration (MDOT/SHA) project.

The objectives of the proposal include: (1) with AI/Machine Learning approaches assess the risks of landslides based on soil/rock types, weather conditions, mechanical properties of slope materials, and the status of existing retaining structures along the selected highway sections, using Maryland as case studies, (2) identify and map the high-risk areas based on controlling factors such as geometry and mechanical properties of soil or rock, and triggering factors, including gravitational and hydraulic forces, using available survey data, remote sensing and LIDAR data and other factors like transportation modes, (3) design and test protocols for real time monitoring at selected sites in consultation with DOT SHA staff, and (4) recommend strategies for reducing the risks of landslides with real-time monitoring for the high-risk areas, and improving the safety of the transportation infrastructure. All the methods and strategies can be transferred to other states or regions with similar geological conditions and engineering configurations. Phase 1 of this project will primarily cover task 1 and part of task 2.

2.4 Alignment with the USDOT strategic plan

The proposed project will address transportation safety, especially physical infrastructure systems and roadway design, covering the following US DOT goals:

- Update roadway design standards to protect vulnerable road users and vehicle occupants.
- Use regulatory and policy tools to advance roadway safety to reduce fatalities and injuries across modes.
- Support the adoption and maturation of safety management systems across modes.
- Use data and data analytics to take proactive actions to address emerging safety risks and support compliance.

The project will provide technical assistance to better identify, assess, and address critical physical vulnerabilities.

- Incorporate physical protections in the standards for design of emerging automated and connected systems and technologies, such as real time sensing and monitoring systems.
- Strengthen system response and recovery plans and protocols to minimize the effects of system
disruptions and hasten system recovery from the natural disasters.
- Promote guidelines on vulnerability assessments with enhancement of AI/ML approaches.

The project will assess and mitigate the vulnerability of transportation infrastructure to climate change and natural disasters:

- Assess the vulnerability of assets and identify novel climate adaptation and mitigation strategies.
- Enhance resilience throughout transportation planning and project development processes by updating guidance and regulations.
- Conduct case studies and pilot projects to develop and evaluate new and innovative adaptation and resiliency technologies, tools, and opportunities, such as motion sensors and early warning systems.

This project will build research capacity in the critical area of designing resilient infrastructure for geohazards and changing climate conditions. It will also provide educational opportunities for graduate and undergraduate students to gain knowledge and experience in this important new area for sustainable and resilient engineering. Thus, the project will also build human capacity to address the challenge of geohazards adaptation related to transportation systems.

Chapter 3

3. Field and Laboratory Investigation

Sunil Lamsal, Atieh Hosseinizadeh, Yi Liu, Zhuping Sheng, Oludare Owolabi

3.1 Background

Understanding and reducing the risk of landslides and other geotechnical hazards requires an understanding of slope stability and soil properties. Extensive soil sampling and laboratory analysis yield the crucial information required for an appropriate assessment of these components. This chapter details the methodologies and results of soil sampling and subsequent laboratory works conducted to assess slope stability and various soil parameters.

The study focuses on the systematic collection of soil samples from strategically chosen locations, considering factors such as topography, vegetation, and land use. Each sample undergoes a series of tests to determine key soil properties, including moisture content, grain size distribution, soil cohesion, internal friction angle, and bulk density. These parameters are integral to slope stability analysis, which typically involves assessing the shear strength of the soil and its ability to resist slope failure under different loading conditions.

The integration of field data with laboratory results facilitates a thorough evaluation of slope stability. By understanding the physical and mechanical properties of the soil, we can apply more landslide models to simulate historical slope failure and predict potential slope failures with climate change and suggest effective mitigation strategies. This report aims to present a detailed account of the soil sampling process, the laboratory procedures employed, and the preliminary findings that contribute to the overall assessment of slope stability in the study area.

In conclusion, this chapter not only documents the methodologies and findings but also underscores the importance of soil analysis in geotechnical engineering. The insights gained from this study are expected to enhance our understanding of slope stability and inform the development of more resilient infrastructure and land-use planning strategies.

3.2 Methodology

To assess soil properties and suitability, soil testing is crucial. For this research, we test our collected samples to find out their basic, mechanical, and hydraulic properties. Finding each property requires different types of laboratory analysis and this report discusses several methodologies we used in laboratory soil testing. They include basic soil properties: Particle Size Analysis, Atterberg limit test, and mechanical properties: direct shear and triaxial tests and hydraulic properties (See more details in Appendix 3A).

3.3 In-Situ Observations and Measurements

3.3.1 Summary for Day 1, Monday, June 24, 2024

Site 1 (39° 03.168 N, -76° 58.611 W)

Site 1 comprises two locations, Site 1A and Site 1B, approximately 500 feet apart. They are situated on the southbound slope of Columbia Pike in Fairland, Montgomery County and can be accessed via a back road. A trail leads to the site, and we located its starting point for easier access in the future.

Site 1A: This location features a manhole and culvert on an embankment slope covered with dense vegetation, making fallen slopes difficult to detect. Initial reason was reported due to the failure of drainage structure (pipes and manhole). The slope failure is reported as progressive and is being repaired as of June 2014 (Table 3.1).

Table 3.1: Historical information provided by SHA for site 1A

PROJECT ID	PROJECT ROAD	FAILUREDATE	LOCATION and DETAILS	FAILURE TYPE	INFORMATION	SLOPETYPE	SOIL TYPE	SUGGESTED	REPAIR STATUS
46	US 29 SWM Retrofit	2/1/2012	Erosion was due to failure of drainage structures (pipe and Manhole)	Erosion-Body; Erosion-Head; Erosion-Toe	Slope Failure has been progressive. OHD developed a project to retrofit the SWM facility in the area and repair the slope failure. Being repaired as of 6/10/14.	Fill	Boulders/ cobbles; Silty sand; Other	Soil Nailing	Post Construction Monitoring

The samples collected contain topsoil, fill materials with gravel and silty soil.

- GPS Coordinates: 39° 03.168 N, -76° 58.611 W
- Elevation: 400 ft
- Slope Length: 63 ft
- Slope Width: 41 ft
- Slope Angle: 25°
- Samples: Site 1A Sample 1 & 2 (Figure 3.1 – 3.3)

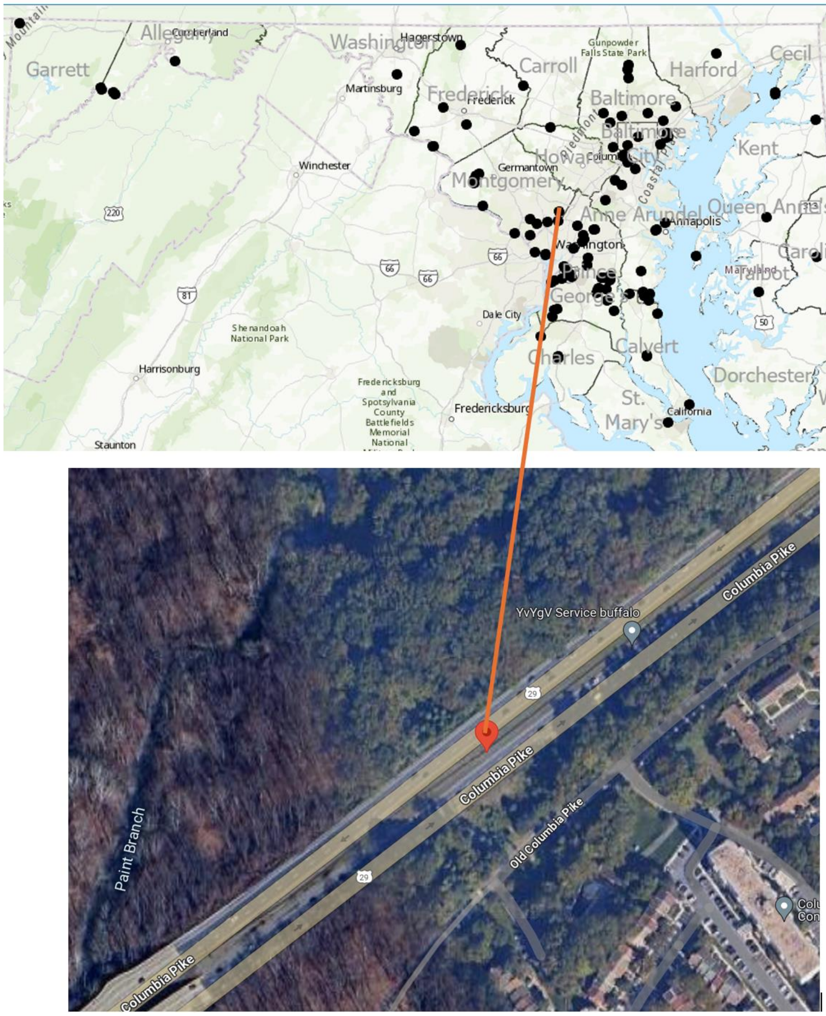

Figure 3.1: The location of site 1A.

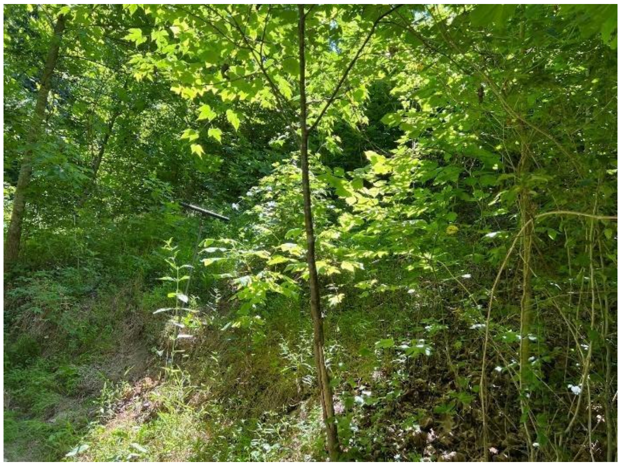

Figure 3.2: Site 1A slope.

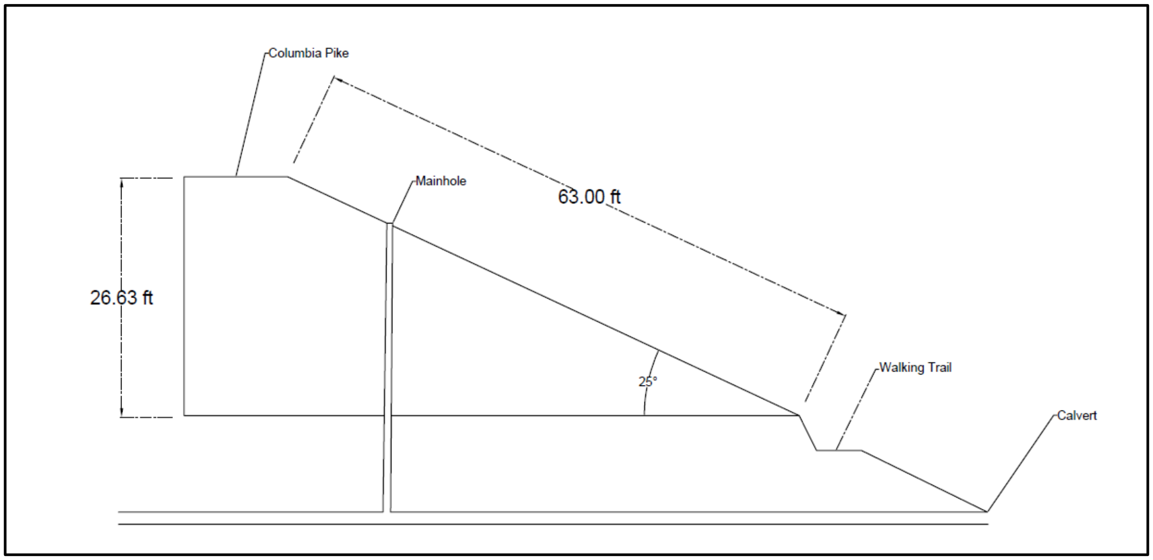

Figure 3.3: Slope sketch of site 1A.

Site 1B: Located 500 feet away from Site 1A along the trail, this area is free of vegetation, with an outward 4ft shift of trail horizontally due to fallen slopes, which indicates the landslide (Table 3.2). The failure of slope is below the roadway. The sample collected contains sandy silt materials.

Table 3.2: Historical information provided by SHA for site 1B

PROJECTID	PROJECT ROAD	FAILURE DATE	FAILURE TYPE	INFORMATION	SLOPE TYPE	SOIL TYPE	SUGGESTED	REPAIR STATUS
47	US 29 SWM retrofit	2/9/2012	Compound/Complex; Deep Non-circular Rotational failure; Erosion-Head	Repair done as of 6/10/14.	Fill	Silty sand	Regrading or Flattening Slope	Post Construction Monitoring

The samples details:

- Slope Length: 119 ft
- Slope Width: 42 ft
- Samples: Site 1B Sample 1, 2 & 3 (Figure 3.4 and 3.5)

Figure 3.4: Site 1 B slope, clear difference in vegetation.

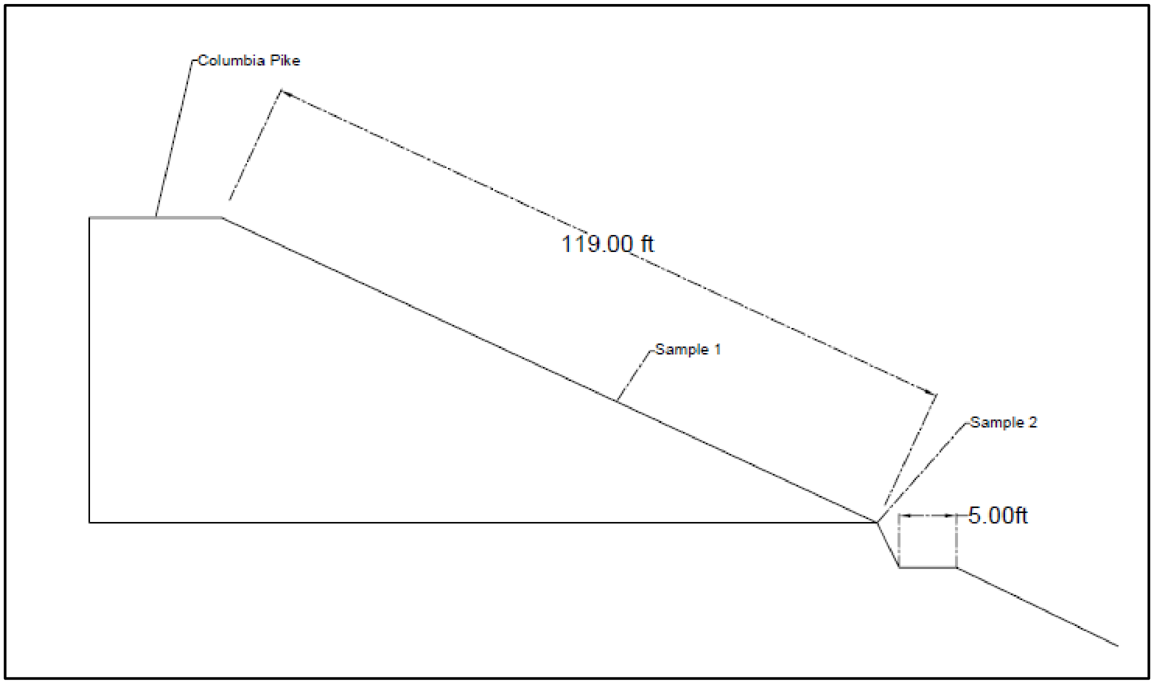

Figure 3.5: Slope sketch of Site 1 B.

Site 2 (39°01.221 N, -76°58.841 W)

Site 2 presents a more concerning situation with visible tree roots hanging, indicating erosion at the foot of the slope. It is situated on the opposite side of the highway from the original GPS coordinates, on the I-495 capital beltway outer loop Silver Spring (Figure 3.6, Table 3.3), Montgomery County. The erosion is reported due to the drainage failure. It is accessible with a parking permit from the nearby facility. The samples contain topsoil, residual soil, samples of weathering bedrock and other materials.

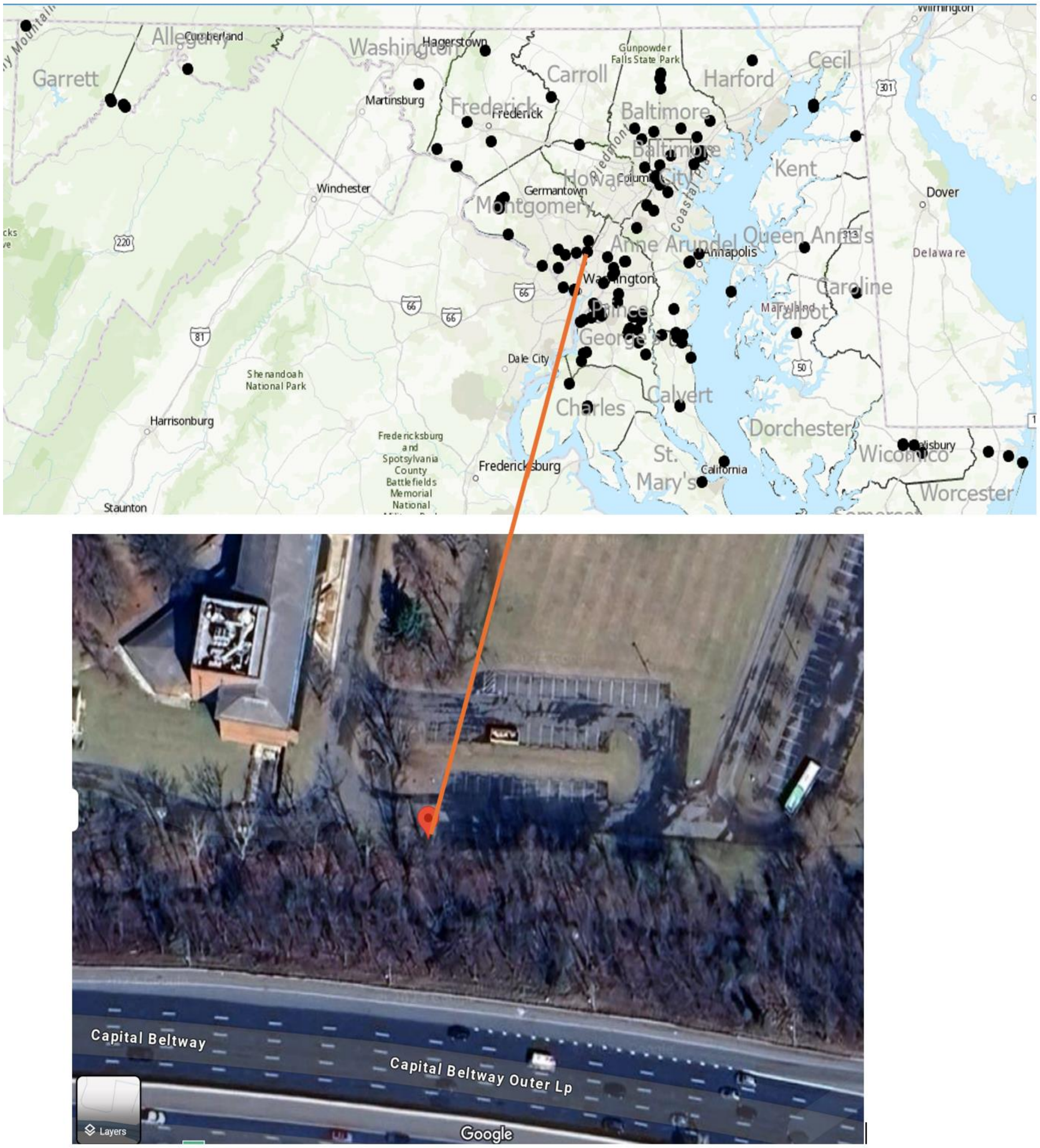

Figure 3.6. The location of site 2.

Table 3.3: Historical information provided by SHA for site 2

PROJECT ID	PROJECT ROAD	FAILURED ATE	LOCATION and DETAILS	FAILURE TYPE	INFORMATION	SLOPE TYPE	SOIL TYPE	REPAIR STATUS
19	Slope Failure on I-495 @ MP 28	10/1/2009	drainage pipe failure	Erosion-Body	multiple locations (4)	Fill	Silty sand	Design

The samples details:

- GPS Coordinates: 39°01.221 N, -76°58.841 W
- Slope Length: 53 ft
- Slope Width: 42 ft
- Slope Angle: 35°
- Samples: Site 2 Samples 1, 2, 3 & 4 (Figure 3.7 and 3.8)

Figure 3.7: Site 2 landslide looks active and needs immediate attention.

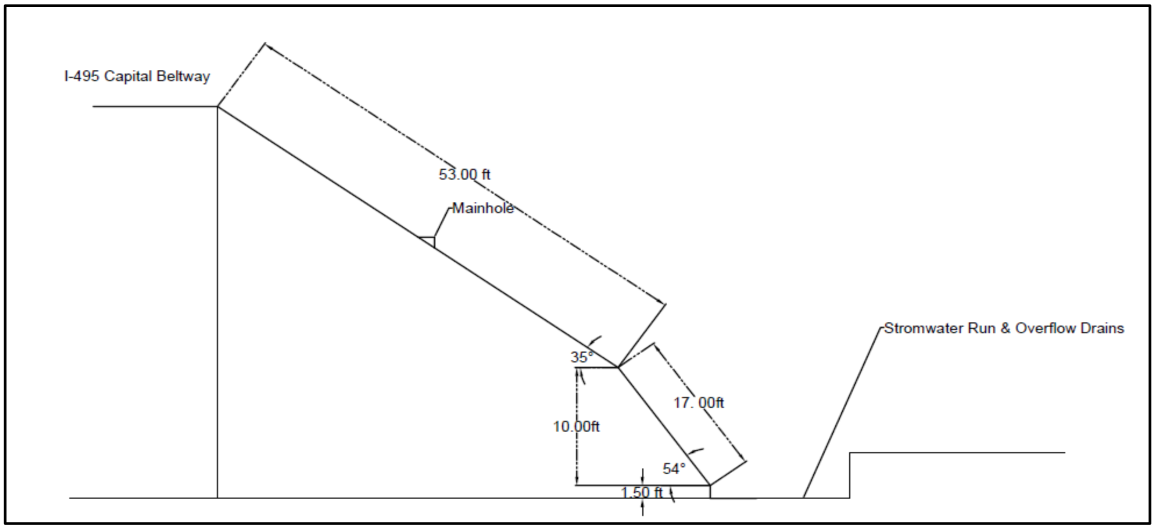

Figure 3.8: Slope sketch of site 2.

Site 3 (39° 0.9336, -77° 1.827)

This site is in the capital beltway I-495 inner loop Silver Spring, Montgomery County. The site is reported to be repaired using riprap as of June 2014 (Table 3.4). Access to Site 3 requires permission from the golf course owner via a back road or traffic control via the highway. An alternative route through a paved drainage ditch is blocked by dense vegetation and a wire fence (Figure 3.9).

Table 3.4: Historical information provided by SHA for site 3

PROJECT ID	**PROJECT ROAD**	**FAILUREDATE**	**FAILURE TYPE**	**INFORMATION**	**SLOPE TYPE**	**SOIL TYPE**	**SUGGESTED**	**REPAIR STATUS**
45	Slope failure on I-495 at m.p 11.06	11/3/2011	Erosion-Body	revisit on 6/27/14. Repaired with riprap (dumped)	Cut and Fill	Silty sand	Rip-rap	Post Construction Monitoring

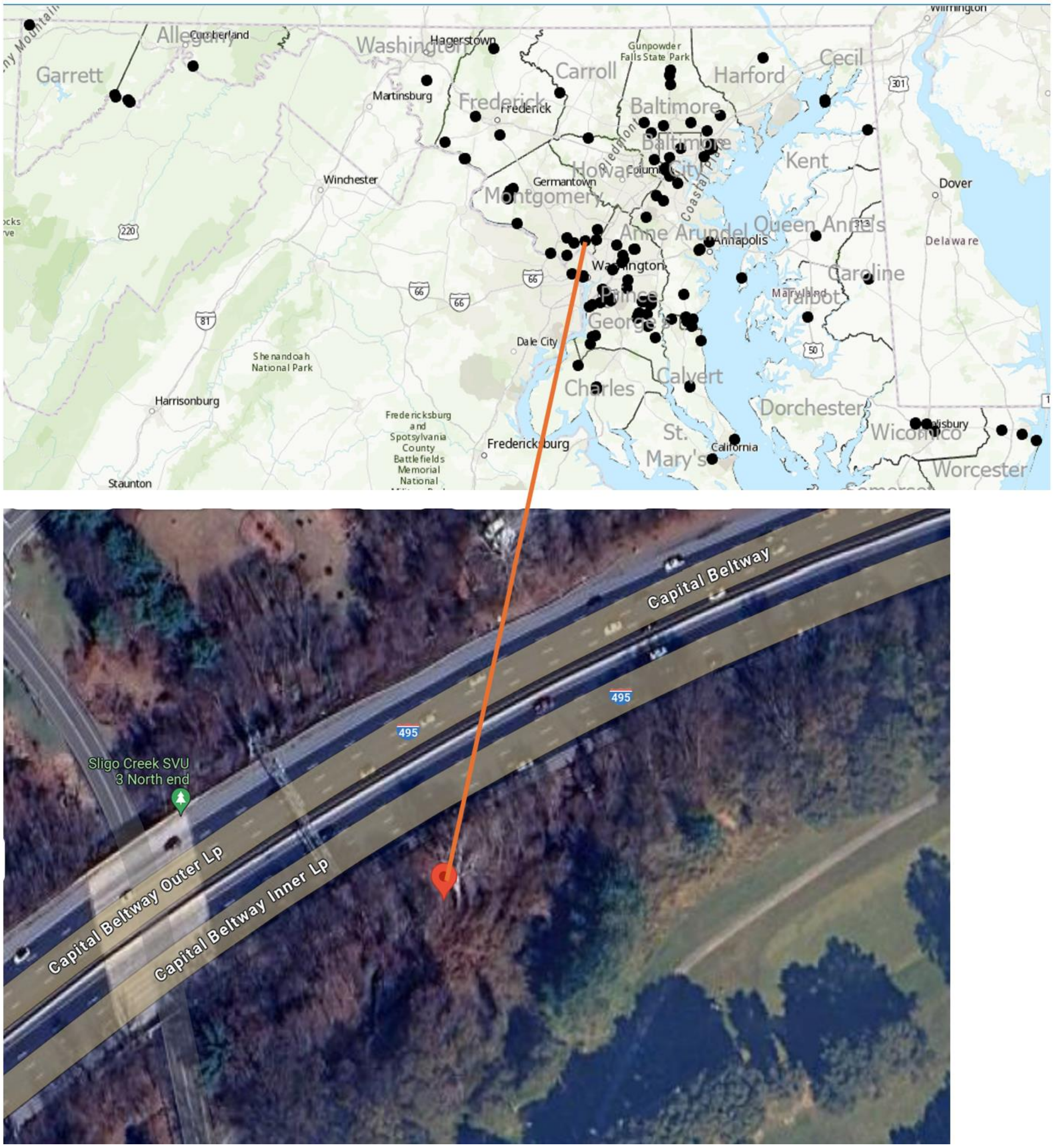

Figure 3.9: The location of site 3.

Site 10 (38° 59.3232, -77° 13.3656)

Site 10 was not visited during this trip and is scheduled for a future visit. It is located on the side of Belfast RD in Potomac, Montgomery County.

3.3.2 Summary of Day 2, Tuesday, June 25, 2024

Site 12 (39°24.266 N, -77°23.584 W)

Site 12 is easily accessible via a back road, situated between the slopes of Highway 40 West and Monocacy Boulevard near Frederick, Fedrick county. Parking is available nearby, potentially across the street in a nearby business area. The slope is an embankment that has been stabilized with riprap covered in stone. Soil samples collected appear to be silt in nature (Figure 3.10).

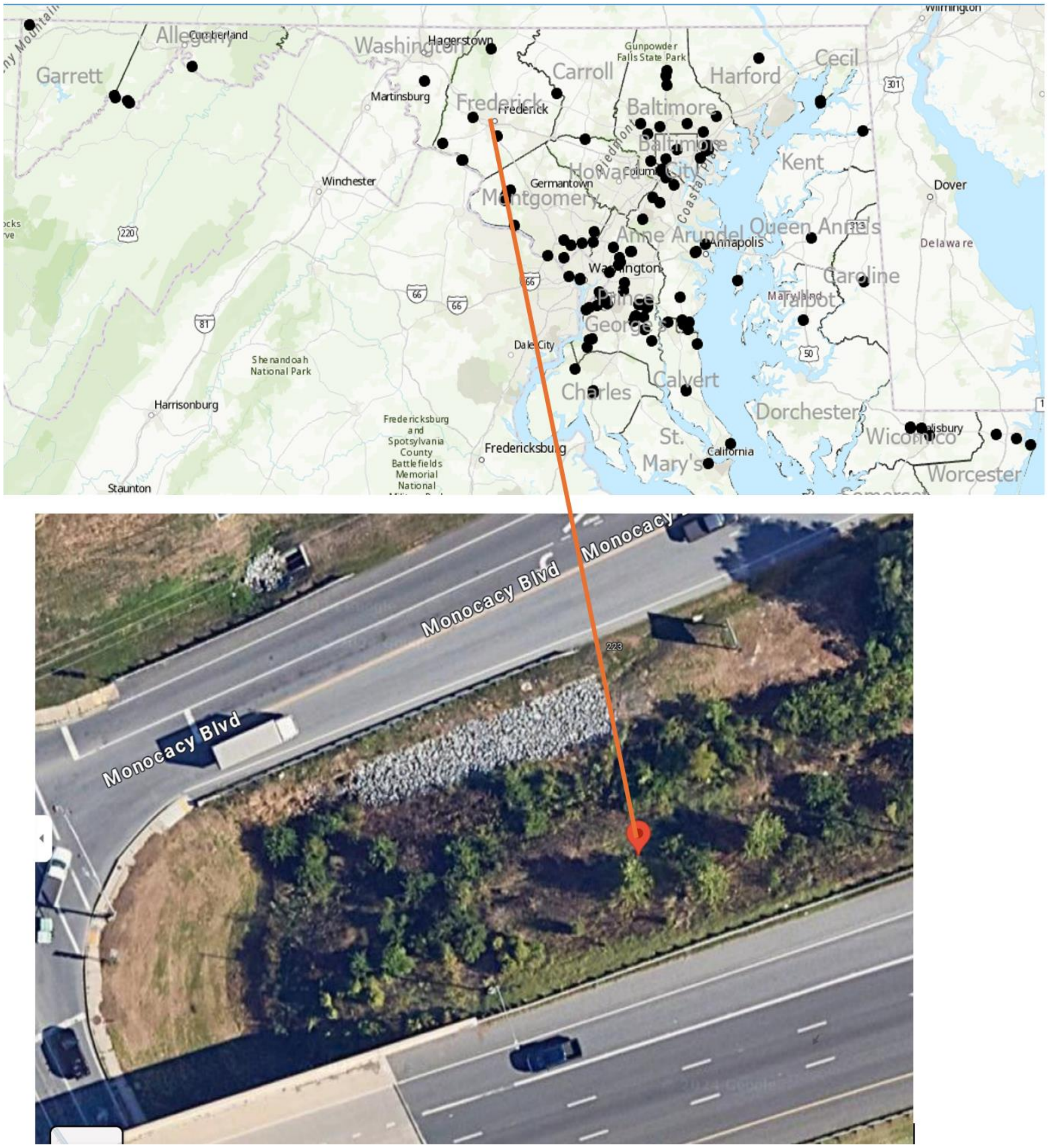

Figure 3.10: The location of site 12.

The samples details:

- GPS Coordinates: 39°24.266 N, -77°23.584 W
- Elevation: 302 ft
- Slope Length: 41.6-9-41.3 ft
- Slope Width: 42 ft
- Slope Angles: 39.5° & 40.5°
- Samples: Site 12 Samples 1, 2 & 3 (Figure 3.11 and 3.12)

Figure 3.11: Collection of soil sample, and the view slope in site 12.

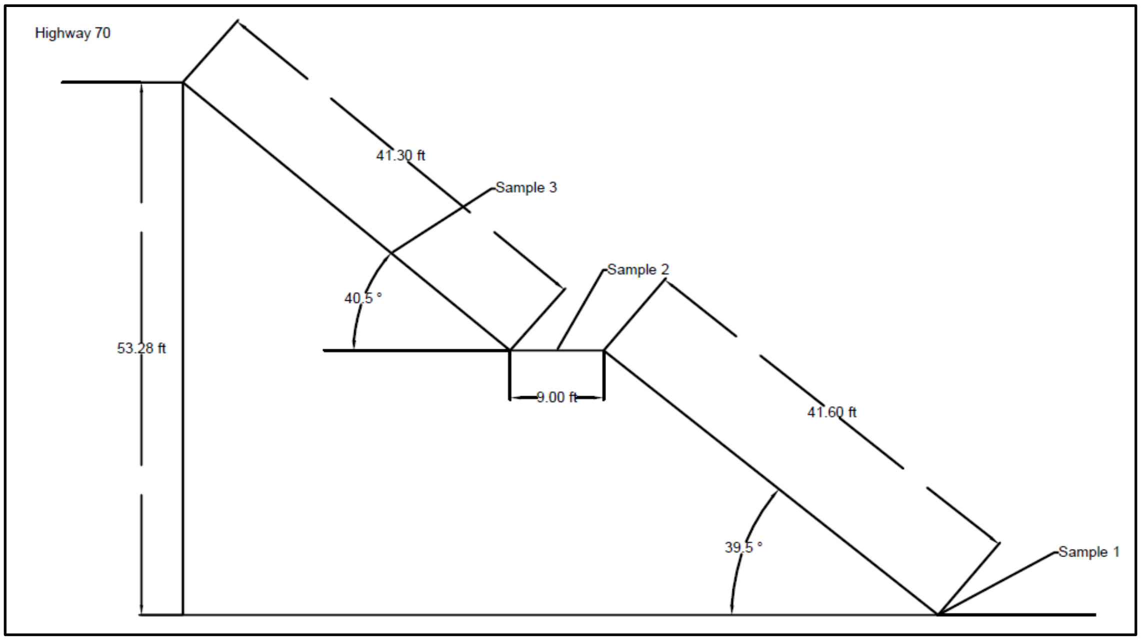

Figure 3.12: Slope Sketch of site 12.

Site 13 (39°38.563 N, -78°47.780 W)
Site 13 is approximately a 1.5-hour drive from Site 12, located on Rt68 National Freeway in Cumberland, Allegany County. The large slope has experienced collapse, with mitigation efforts including soil nailing and benching. The stones present are brittle in nature. Parking is available alongside the road but may require traffic control. Samples collected include stone samples, brittle topsoil, and original soil from tree roots (Figure 3.13 to 3.17).

The samples details:

- GPS Coordinates: 39°38.563 N, -78°47.780 W
- Elevation: 930 ft
- Slope Length: 28 ft (first slope), 10 ft (second slope at west) / 76 ft and 22 ft
- Slope Angles: 47.5° & 36.5° (slope at west) / 26.3° and 32.2°

- Samples: Site 13 Samples 1, 2 & 3 (Figure 3.13 to 3.17)

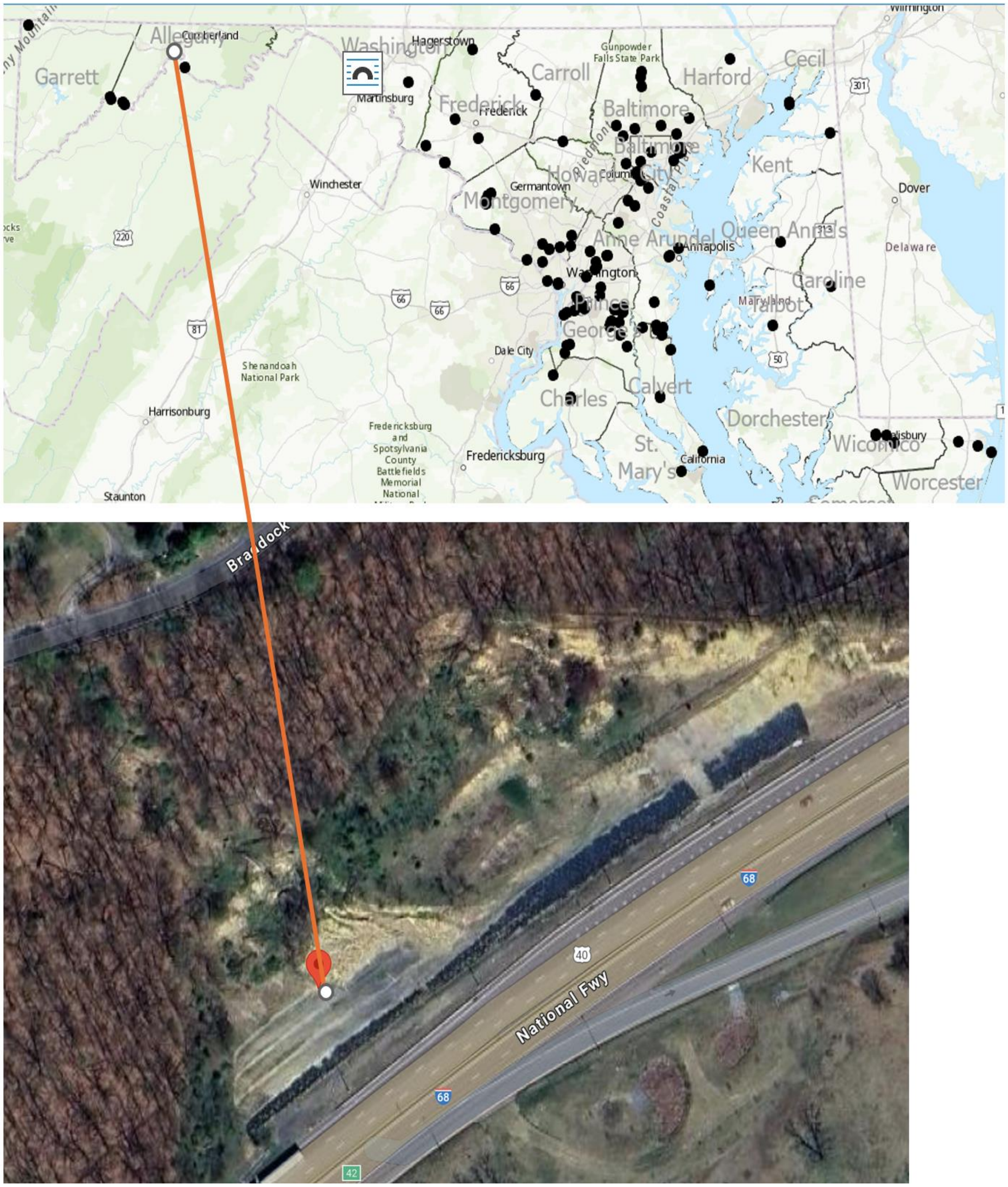

Figure 3.13: The location of site 13.

Figure 3.14. Soil nailing to mitigate landslide at site 13.

Figure 3.15: Starting point of landslide at the top (left) and benches built during the mitigation.

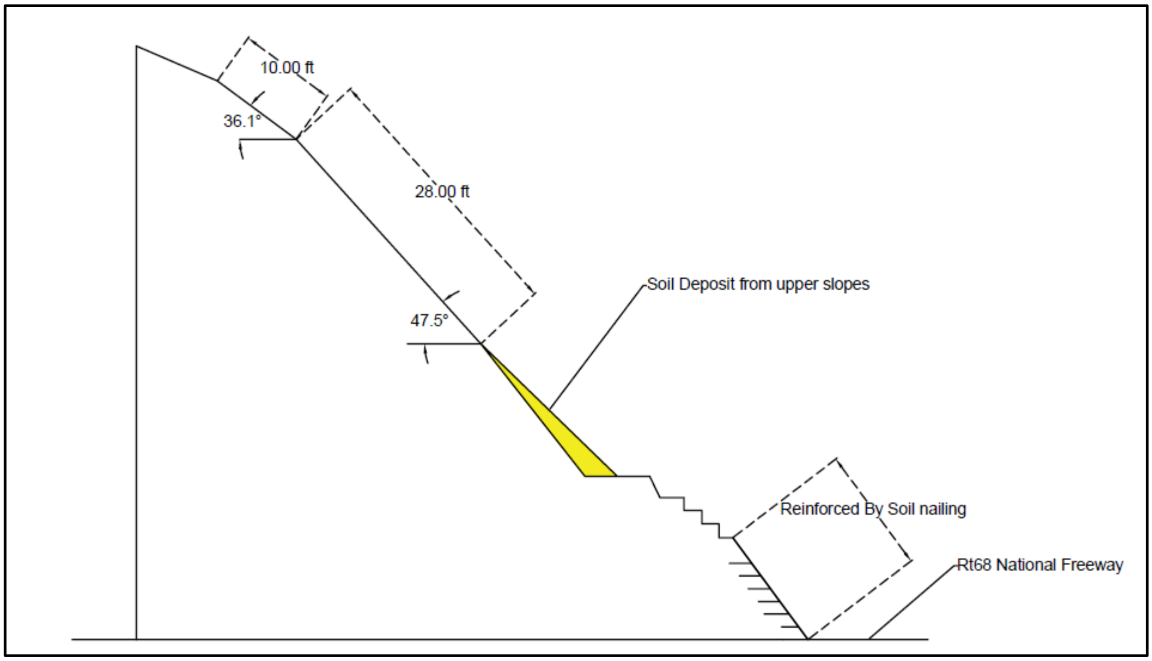

Figure 3.16: Slope Sketch of site 13 (west side).

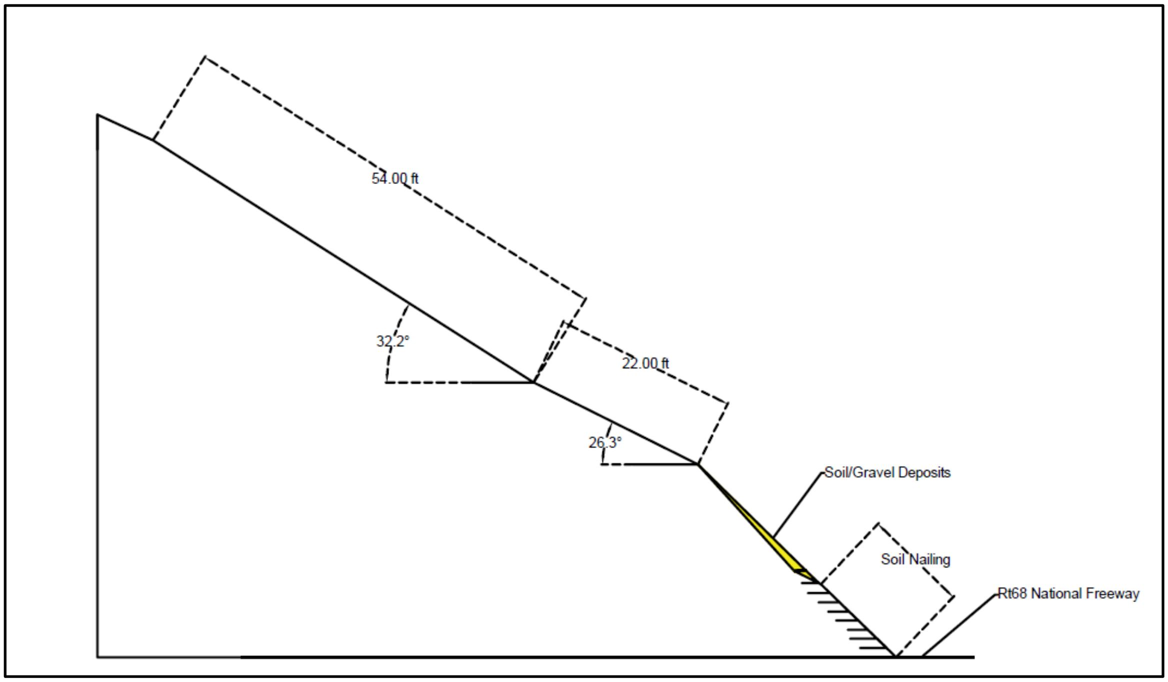

Figure 317: Slope Sketch of site 13 (East side).

Site 11 (39° 13.75397436N, -76° 41.58593298W)

Site 11 is located near Catonsville on southeastern Blvd, Baltimore County. Due to time constraints, detailed samples and measurements were not taken at Site 11.

However, visual observations suggest the slope is stabilized using riprap. Photographs were taken for future reference and analysis. (Revisit /Traffic Control & Utilities Marking) (Figure 3.18 and 3.19).

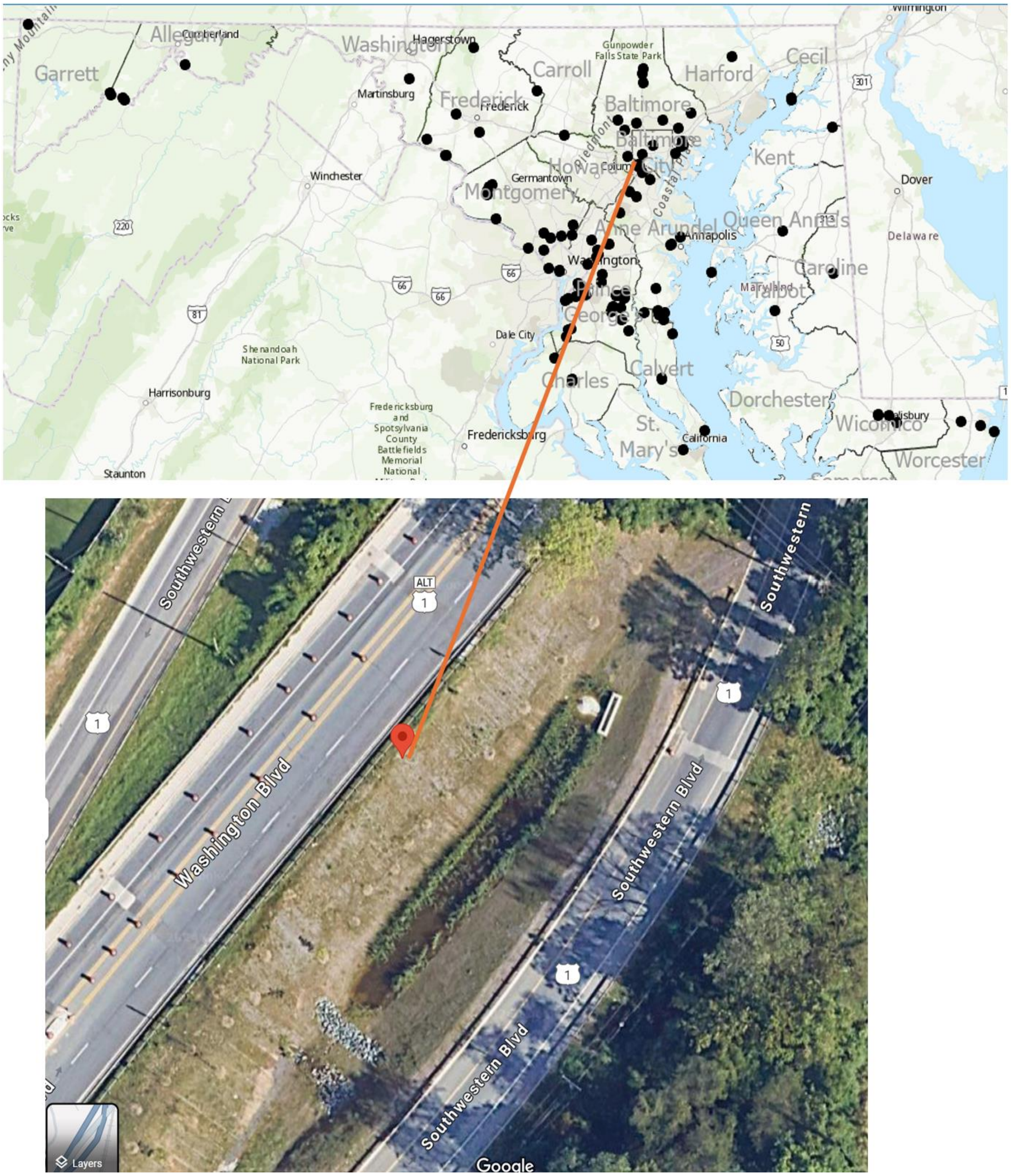

Figure 3.18: The location of site 11.

Figure 3.19. Landslide happened on April 4, 2024, at site 11.

3.3.3 Summary of Day 3, Wednesday, June 26, 2024

Site 8 (38° 59.997801, -76° 53.5477128)

This site is located on the slope of I-495 Capital Beltway Outer Loop at Exit 23 in Greenbelt, Prince George's County, Site 8 is accessible via a back road. Parking is available at a nearby business complex. Clear cutting of vegetation provides a walking path to the site. The site is reported to be fixed using riprap previously but again has fallen (Table 3.5). Unfortunately, no fallen slopes were discovered during this visit. The fence has already been cut, facilitating easy access for further investigation (Figure 3.20).

Table 3.5: Historical information provided by SHA for site 8

PROJECT ID	PROJECT ROAD	FAILURE DATE	LOCATION	FAILURE TYPE	INFORMATION	REPAIR STATUS
230	Ramp from I-495OL to MD 201 Slope Failure	11/14/2018		Erosion-Body; Erosion-Head	Slope previously fixed with riprap failed again	Design Complete and Waiting for Construction

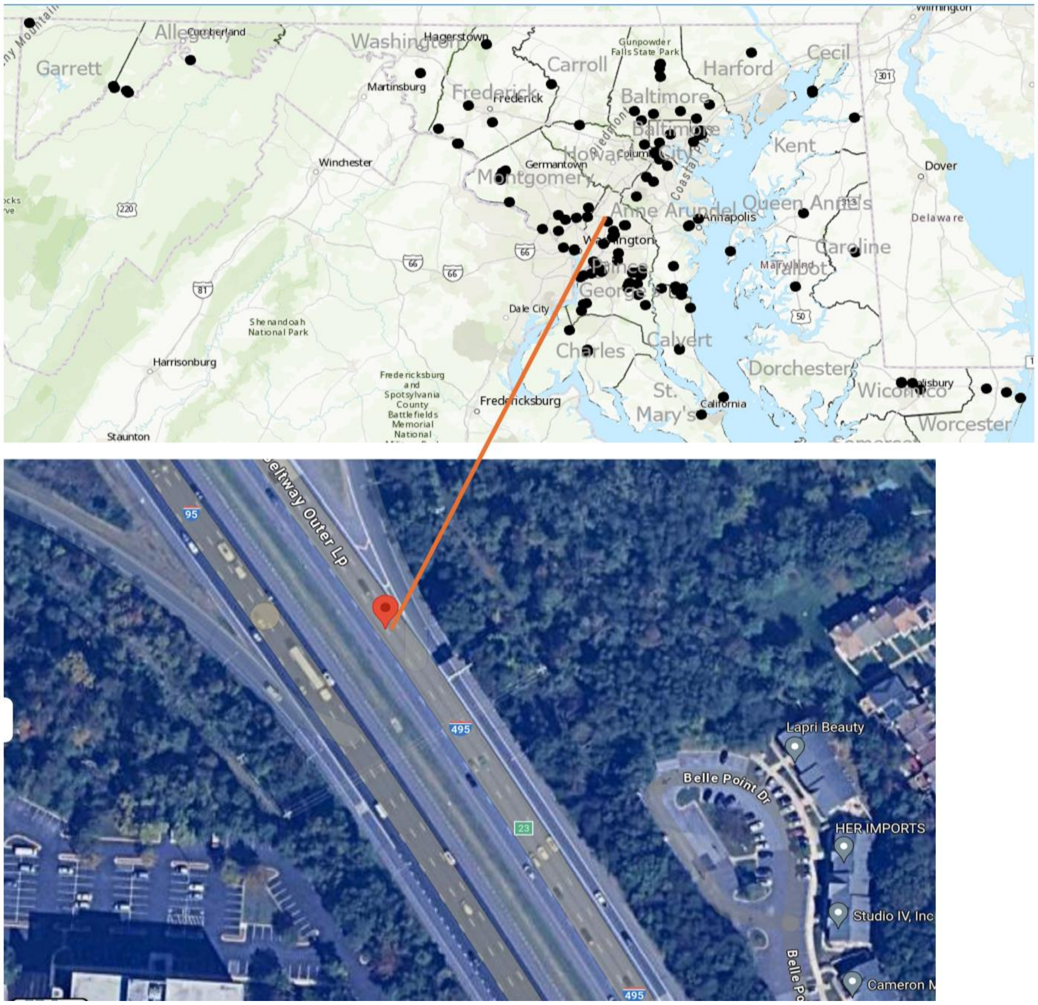

Figure 3.20. The location of site 8.

Site 7 (38° 58.1124996, -76° 52.1010792)

This site is situated on I-95 Capital Beltway Outer Loop near New Carrollton, Prince George's Maryland (Table 3.6). Site 7 is currently inaccessible due to a wire fence on the back road. This site has I-95/495 Slope and Drainage Failures between US 50 and MD 295. Parking options include the temple parking space if accessed from the back road (Figure 3.21 and 3.22). Traffic control is necessary for further investigation of this site.

Table 3.6: Historical information provided by SHA for site 7

PROJECT ID	PROJECT ROAD	FAILURE DATE	FAILURE TYPE	INFORMATION	REPAIR STATUS
227	I-95/495 Improvements from US 50 to MD 295	1/11/2019	Erosion-Body	I-95/495 Slope and Drainage Failures between US 50 and MD 295	In Review

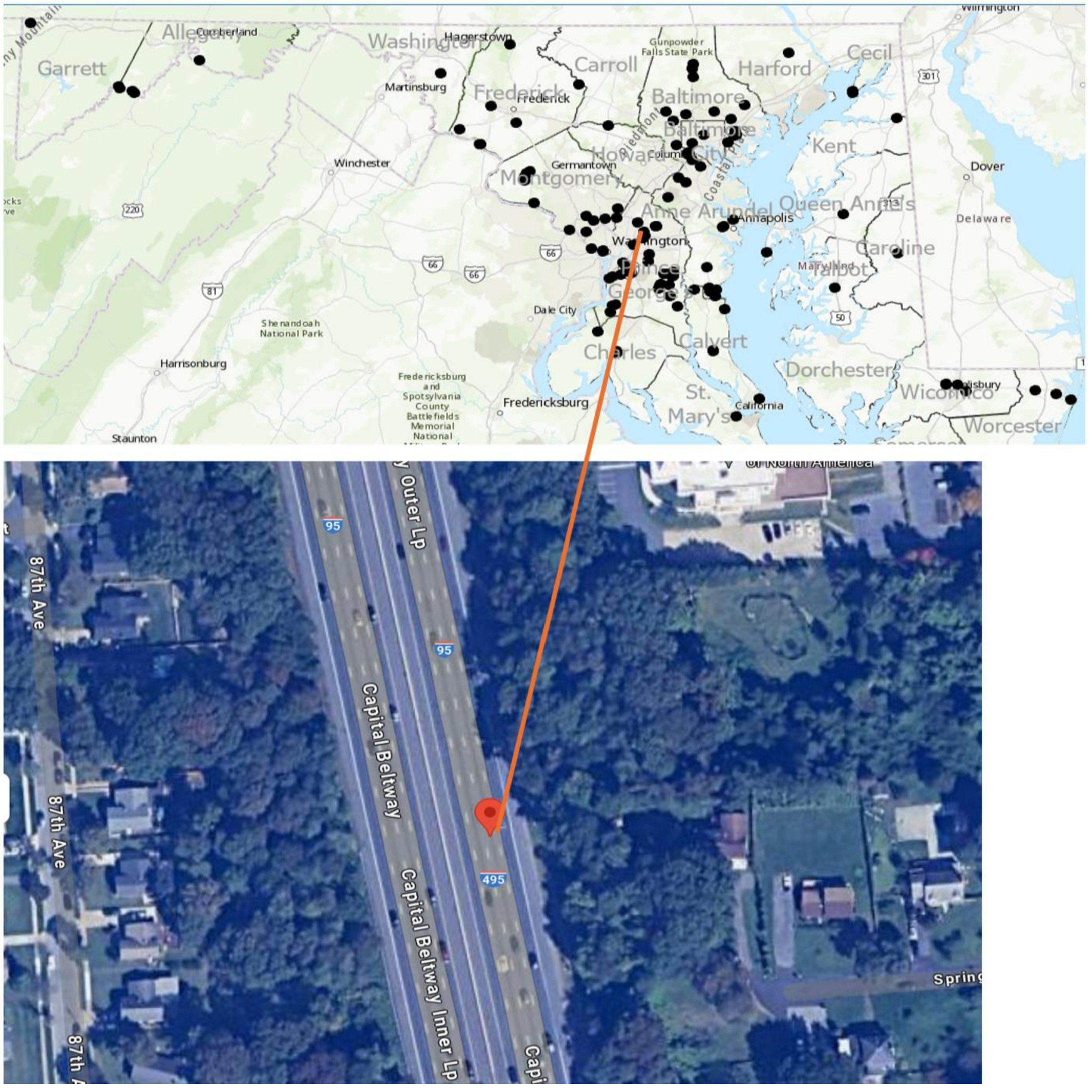

Figure 3.21: The location of site 7.

Figure 3.22: Site 7 behind the wire fence.

Site 6 (38° 57.2620944, -76° 51.7830684)

This site also is located on I-495 Capital Beltway Outer Loop near New Carrollton, Maryland, Site 6 features large walls on the highway side and a wire fence on the back road. It is reported that Slope failure is due to drainage pipe failure (Table 3.7). To investigate this site, we may request SHA (State Highway Administration) assistance to access the site. Approval from property owners may also be required to traverse through their backyard (Figure 3.23).

Table 3.7: Historical information provided by SHA for site 6

PROJECT ID	PROJECT ROAD	FAILURE DATE	LOCATION and DETAILS	FAILURE TYPE	INFORMATION	SLOPE TYPE	SOIL TYPE	SUGGESTED	REPAIR STATUS
151	Slope failure on 95 at m.p 19.2	3/27/2014	drainage pipe failure caused a erosion at the top	Erosion -Head	Slope failure due to drainage pipe failure (24 inch CMP)	Fill	Silty sand	Soil Nailing	Design

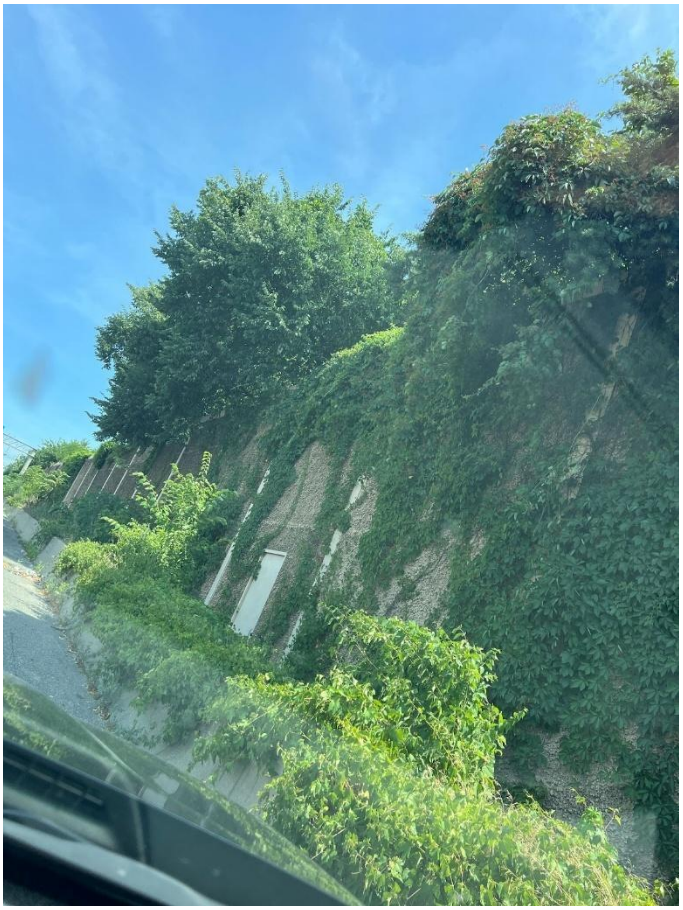

Figure 3.23. Site 6 from the beltway.

Site 5 (38° 56.6474736, -76° 52.4194362)
This site is situated on US-50 John Hanson Way, on the side slope of Beaverdam Creek in Ardwick Park, PG county Maryland. This site is reported to have minor erosions and is fixed using riprap (Table 3.8). This site requires traffic control for access. It is not accessible via the back road (Figure 3.24).

Table 3.8: Historical information provided by SHA for site 5

PROJECT ID	PROJECT ROAD	FAILURE DATE	FAILURE TYPE	INFORMATION	SLOPE TYPE	SOIL TYPE	REPAIR STATUS
122	Slope failure on US 50 at m.p 4.5	1/29/2014	Erosion-Head	Minor erosion. revisit on 4/10/14. No repair and similar condition. Temporary fix around lamp pole with riprap.	Natural	Silty sand	Design

Figure 3.24: Site 5 when seen from bridge at John Hanson way.

3.3.4 Summary of Day 4, Thursday, June 27, 2024

Site 9 (38° 41.60128758, -76° 43.63729926)

This is located near the slope of Croom Road in Dunkirk, PG county, Maryland, Site 9 allows parking on the shoulder of the road. Traffic control or continuous monitoring of traffic may be necessary due to its proximity to the road. The slope appears fixed using riprap and new pavement was done recently; however, erosion is evident due to poor drainage. Rainwater runoff has caused significant erosion on the slope (Figure 3.25 and 3.26).

- Slope Length: 19 ft
- Slope Angle: 30.2°
- Samples: Site 9 Samples 1, 2 & 3

Before repair (August 24, 2023)

After repair: The side slope is already eroded by bad drainage (June 27, 2024)

Figure 3.25. Site 9 slope.

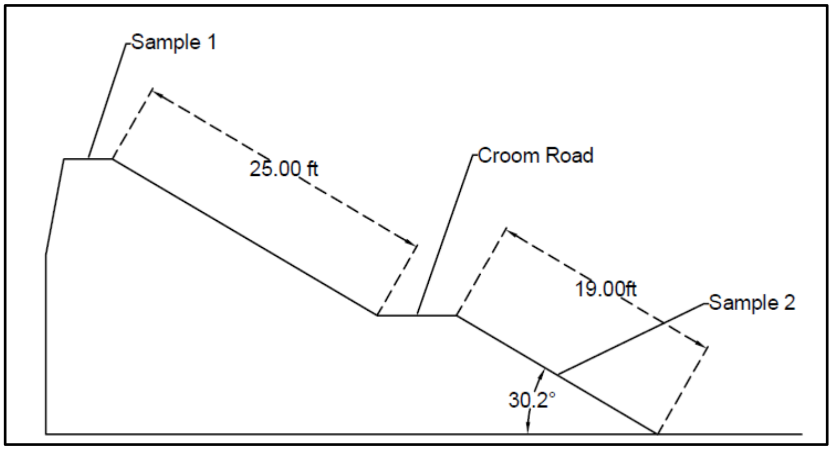

Figure 3.26. Slope sketch of site 9.

Site 4 (38° 55.1824128, -76° 54.5872188)

This is situated on John Hanson Way in Cheverly, Maryland, Site 4 requires traffic control for access and cannot be reached via the back road (Figure 3.27 and Table 3.9).

Figure 3.27: Site 4 as seen from satellite image. This site is not accessible through the back road.

Table 3.9: Historical information provided by SHA for site 4

PROJECT ID	PROJECT ROAD	FAILURE DATE	FAILURETYPE	INFORMATION	SLOPE TYPE	SOIL TYPE	SUGGESTED	REPAIR STATUS
123	Slope failure on US 50 at m.p 1.8	1/28/2014	Erosion-Body	Slope failure, Revisit on 4/10/14, repaired with riprap.	Cut	Silty soil	Rip-rap	Post Construction Monitoring

Chapter 4

4 Characterization and detection of landslides with LiDAR and InSAR data

Adebayo Olude, Ahmir Muley, Katherine Nieto Correa, Oludare Owolabi, Yi Liu, Zhuping Sheng,

4.1 Background

Landslides are a common natural disaster that can occur anywhere in the world. A landslide occurs when soil, rocks, or debris are pulled down a slope by gravity. Between 1998 and 2017, landslides affected approximately 4.8 million people and resulted in more than 18 000 deaths. Climate change and rising temperatures are expected to trigger more landslides [10]. Although landslides are a natural phenomenon that will likely always occur globally, scientists continue to develop new methods to prevent and detect landslides before they occur.

The world's remote sensing methods have continued to improve drastically as new technologies are developed to assist with them. In recent years, the use of Light Detection and Ranging (LiDAR) and Interferometric Synthetic Aperture Radar (InSAR) imagery has proven to be efficient in providing highly detailed imagery of areas with potential landslides. LiDAR is a form of remote sensing that uses light in the form of a pulsed laser to measure ranges (variable distances) to the Earth. These light pulses—combined with other data recorded by the airborne system—generate precise, three-dimensional information about the shape of the Earth and its surface characteristics. [11]. The three-dimensional images provided by LiDAR can be used to examine the topography of different areas.

InSAR is also a form of remote sensing. InSAR can detect small differences in the distance between its position and the ground as the land surface moves—whether up, down, or sideways. InSAR shows spatial patterns of deformation in remarkable detail [12]. InSAR’s ability to detect slope failures in the ground is a key benefactor for detecting landslides, as one of the major contributors to landslides occurring is slope failures in the soil. When using both Lidar and InSAR, along with other remote sensing techniques, scientists have a much higher chance of predicting potential areas where a landslide can occur.

The goal of this research is to process highly detailed topographic imagery on the various counties in Maryland using geospatial technologies and remote sensing methods for the purpose of determining which areas are the most susceptible to landslides.

4.2 Literature Review

4. 2.1 LiDAR

LiDAR uses laser beams to determine distances to the Earth's surface, resulting in detailed 3D terrain models. A detailed overview of LiDAR concepts and uses in landslide investigations was presented in [13]. The technology is implemented in two major ways: Airborne LiDAR Scanning (ALS) has been proven to be successful in mapping large-scale landslides and recognizing minor geomorphological characteristics, as demonstrated by [14]. Terrestrial LiDAR Scanning (TLS)'s applications for monitoring deformations in rock slopes and detecting movements might help predict future occurrence [15]. Despite the advantages of LiDAR, it has some limitations and knowledge gaps that need to be addressed. Challenges in data collection, such as vegetation cover, cloud cover and accessibility can affect the accuracy and precision of the terrain models. Combining LiDAR data with additional datasets such as hydrological, geological and land use data is often needed to gain a better understanding of landslides mechanism and susceptibility. It is essential to validate the identification and monitoring methods for slope failure using remote sensing by conducting field surveys. This validation is necessary to verify the accuracy and dependability of the results. Furthermore, the process of measuring and determining the specific properties of landslides, such as their size, speed, and other attributes, is still being actively studied. Creating precise predictive models for landslide susceptibility using only LiDAR data might be difficult, and using advanced analytical approaches may be necessary to improve the model's dependability.

4.2.2 InSAR

InSAR detects surface deformations using phase difference between radar signals. Ferretti et al. [16] explored a comprehensive analysis of the fundamental principles and practical uses of InSAR in the context of monitoring landslides. Several techniques include: Differential Interferometric Synthetic Aperture Radar (DInSAR) is a technique used to map the movement of landslides in urban settings with low velocity. Evidence of the effectiveness of DInSAR in this application were provided by [17]. Persistent Scatterer InSAR (PSI) was introduced by [18] and has since been widely used for long-term deformation monitoring. Small baseline subset technique (SBAS) used for time series analysis of SAR (Synthetic Aperture Radar) images is particularly effective for monitoring and measuring ground deformation over time [19].

Indeed, the SBAS technique is of main interest for this study due to its advanced applicability and the direct relationship with the goals of our study. This technique selects pairs of SAR images that have small spatial and temporal baselines. A small spatial baseline means the images are taken from nearby satellite positions, while a small temporal baseline minimizes temporal decorrelation caused by changes on the Earth's surface. SBAS generates interferograms by using this SAR data reducing the spatial and temporal decorrelation [20].

The SBAS approach is used in various applications, including monitoring urban subsidence, detecting ground movements in mining areas, assessing the stability of infrastructure, and studying volcanic and seismic activity [21, 22]. Despite its advantages [21] highlighted several limitations of the classic SBAS technique. One major issue is that the method often results in sparse coverage of high-coherence points (HPs), especially in vegetated, forested, or low-reflectivity areas, reducing the method's effectiveness for measuring deformation in such regions. Additionally, the method's dependence on the selection of stable points means that any inadequacy in this selection can lead to inaccuracies in deformation measurements. Furthermore, the method is also limited by its reliance on single-polarization, single-mode, and single-channel information from SAR satellites, which fails to fully exploit the advanced capabilities of newer multi-polarization and multi-mode satellite data. These inherent limitations have led to the development of various improved SBAS methods aimed at enhancing the technique's applicability and accuracy in diverse scenarios.

The application of InSAR SBAS analysis has grown significantly over the years, establishing itself as a reliable method for investigating landslides worldwide. This time series technique was used to study slow-moving landslides in the Zhouqu region of China [23]. Their research identified 11 active earthflows and 19 active landslides, each with deformation rates exceeding 100 mm/year. Furthermore, they added 20 new instabilities to the existing landslide inventory map. The study highlighted the impact of seasonal variations and the accelerated deformation following the Wenchuan earthquake on these earthflows and landslides.

Alternatively, both SBAS and PSI techniques [24] were employed and their accuracy against were evaluated with various contextual geodetic data, including permanent GNSS records. The study found a high degree of similarity between the displacement velocity estimates from the PSI and SBAS approaches, with a standard deviation of 6 mm/year for vertical rate differences. This consistency confirms the reliability of both InSAR methods for monitoring ground displacement. The accuracy assessment revealed that the standard deviations in vertical displacement estimates were 9-10 mm/year when compared with GNSS benchmarks and 8 mm/year against leveling data. Importantly, relative errors were less than 20% for locations experiencing subsidence greater than -15 mm/year, demonstrating that the InSAR techniques are particularly effective for detecting significant vertical displacement.

A recent study of the East Coast of the United States has highlighted subsidence hazards affecting communities and infrastructure, particularly in metropolitan areas like New York, Norfolk, and Baltimore. Vertical land motion rates were assessed using a combination of InSAR data and observations from GNSS stations [25]. The study found that as subsidence rates increase, the area affected by severe subsidence hazards decreases. Although a large portion of land is subject to subsidence, the regions experiencing the highest rates of subsidence are relatively limited. This suggests that while subsidence is widespread along the US East Coast, the most severe impacts are concentrated in fewer areas. This finding underscores the need for a detailed understanding of subsidence rates at the county level and highlights the importance of defining appropriate thresholds for subsidence rate concerns.

4.2.3 Integration of LiDAR and InSAR

Several studies have investigated the utilization of Lidar and InSAR for evaluating slope collapse. Lidar data, known for its detailed topographic data, has been utilized to identify terrain features that affect slope instability, including scarps, cracks, and variations in slope gradient [13, 16]. Nevertheless, they also recognized the constraints associated with the complexity of data processing, the impact of vegetation, and the expenses involved [26]. The study highlights areas of knowledge gaps in the most effective methods for processing data, integrating data, transferring data, and assessing the accuracy and validity of data. In contrast, InSAR has the capability to identify small surface deformations that could potentially indicate slope movement. This makes it an invaluable tool for continuously monitoring the stability of slopes over a period [16, 27].

A large and growing body of literature has investigated several techniques to combine Lidar and InSAR data to improve the detection of possible areas where slopes may collapse. Methods such as analyzing Lidar data over many time periods, combined with measuring displacements using InSAR, have demonstrated encouraging outcomes in the mapping and surveillance of slope instability [28, 29]. Although research from [28] have demonstrated encouraging findings in integrating LiDAR and InSAR data, there is a need for a standardized approach to merge the data. This involves resolving discrepancies in spatial and temporal resolutions and creating algorithms that can automatically integrate and analyze the data from both remote sensing technologies.

4.3. Methodology

This research involved acquiring LIDAR data for counties in Maryland from the Maryland LIDAR data website. For our investigation, LIDAR maps from different years were used for comparison. The list of obtained LIDAR maps is presented in Table 4.1. Figure 4.1 shows the methodological flowchart for the LiDAR data Map.

Table 4.1: List of LiDAR Data Maps Obtained from Maryland LiDAR data

S/N	County	DEMs	Year
1	Prince George	0.9m	2014
		0.6m	2018
2	Montgomery	1.2m	2013
		0.6m	2018
3	Calvert	2m	2011
		0.3m	2017
4	Caroline	2m	2003
		1m	2013
5	Carroll	1m	2006
		0.7m	2015
6	Cecil	1m	2005
		1m	2020
7	Charles	2m	2004
		0.9m	2014
8	Dorchester	2m	2003
		0.9m	2013
9	Garrett	3m	2005
		1m	2015
10	Harford	1.5m	2013
		1m	2020
11	Howard	2m	2011
		0.6m	2018
12	Kent	2m	2006
		7m	2015
13	Montgomery	1.2m	2013
		0.6m	2018
14	Prince George	0.9m	2014
		0.32m	2020
15	Somerset	1m	2012
		1m	2020
16	Talbot	2m	2004
		0.7m	2015
17	Wicomico	1m	2012
		1m	2020

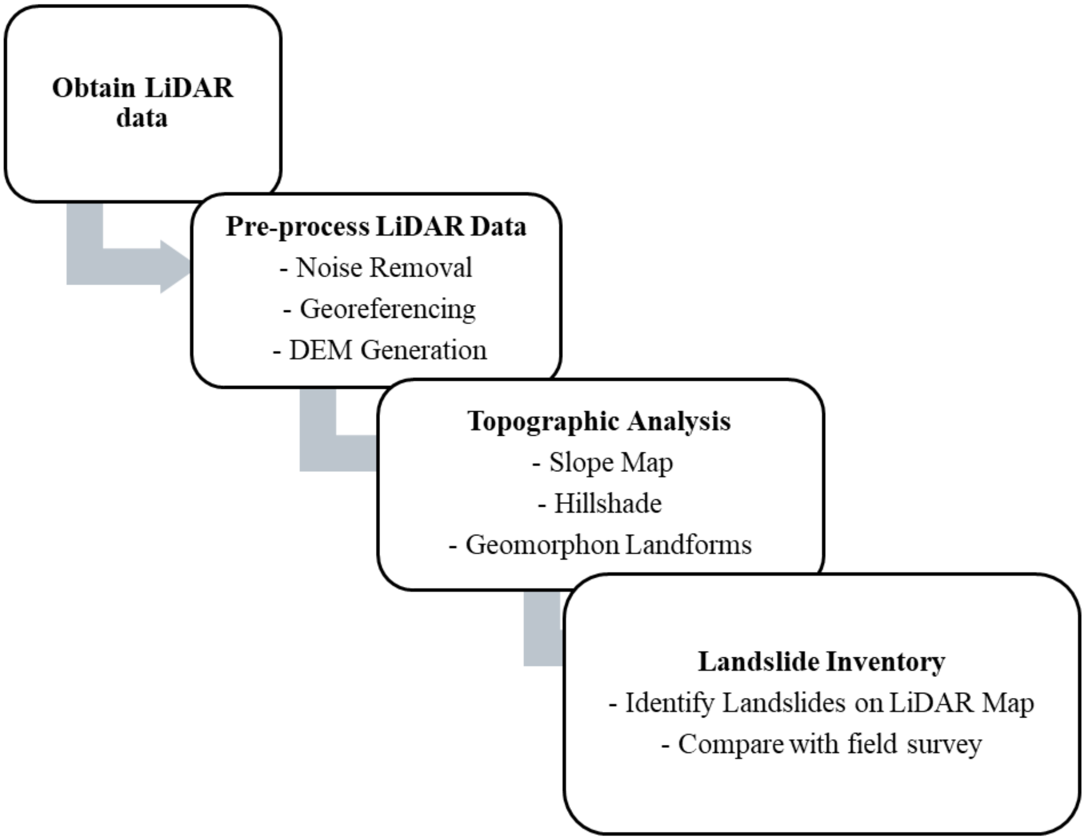

Figure 4.1: LiDAR Data Analysis Flowchart

4.3.1 LIDAR Acquisition and Processing

Figure 4.2 displays Montgomery County, while the others are included in the appendix section. ArcGIS Pro was utilized for image analysis. The LIDAR maps were acquired over different years with varying Digital Elevation Models (DEMs). The 2013 and 2018 LIDAR maps were analyzed in ArcGIS Pro with DEMs of 1.2m and 0.6m, respectively. The 2013 map, with its high-resolution DEM, was primarily used for analysis. However, images from both years were compared using the raster calculator feature in ArcGIS Pro to identify elevation differences. ArcGIS Pro was also used to analyze the county's hill shade, slope maps, and landforms, along with the identified landslide location.

Montgomery County

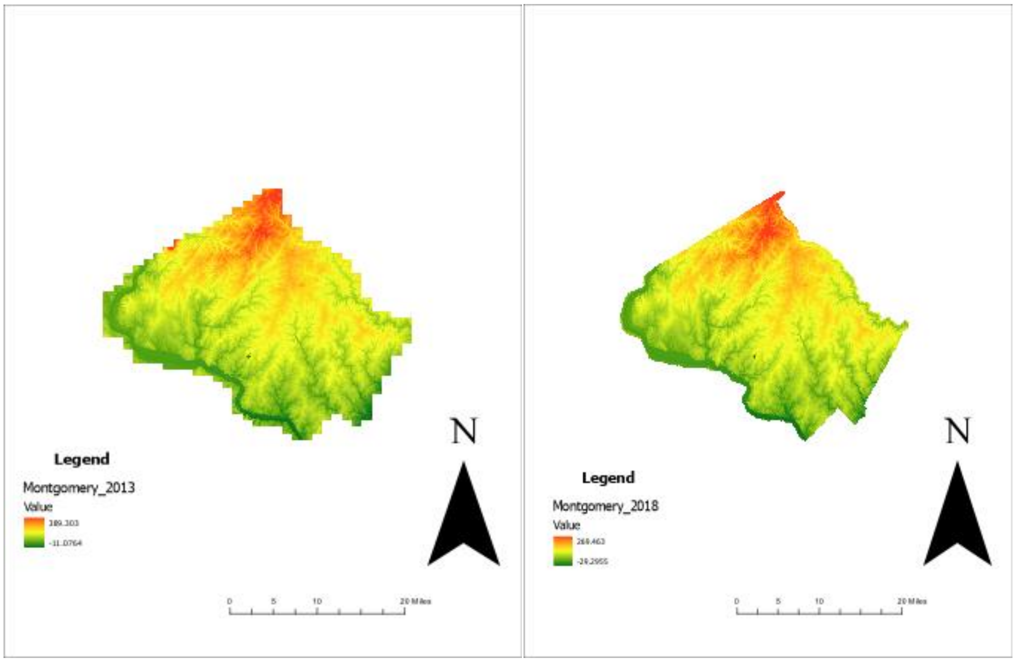

Figure 4.2: Lidar Map for Montgomery County

4.3.2 Resolution of Lidar DEM data

The digital elevation model (DEM) represents topographic relief and ground elevation. Different resolution DEMs have been compared, as shown in Figure 4.1. The 0.6m resolution DEM for Montgomery County in 2018 is depicted in Figure 4.3a, while the 1.2m resolution DEM for the same county in 2013 is shown in Figure 4.3b. Since high-resolution DEMs are more effective in identifying topographic features such as linear structures, the 1.2m resolution LIDAR data from the Maryland LIDAR map was used in this research.

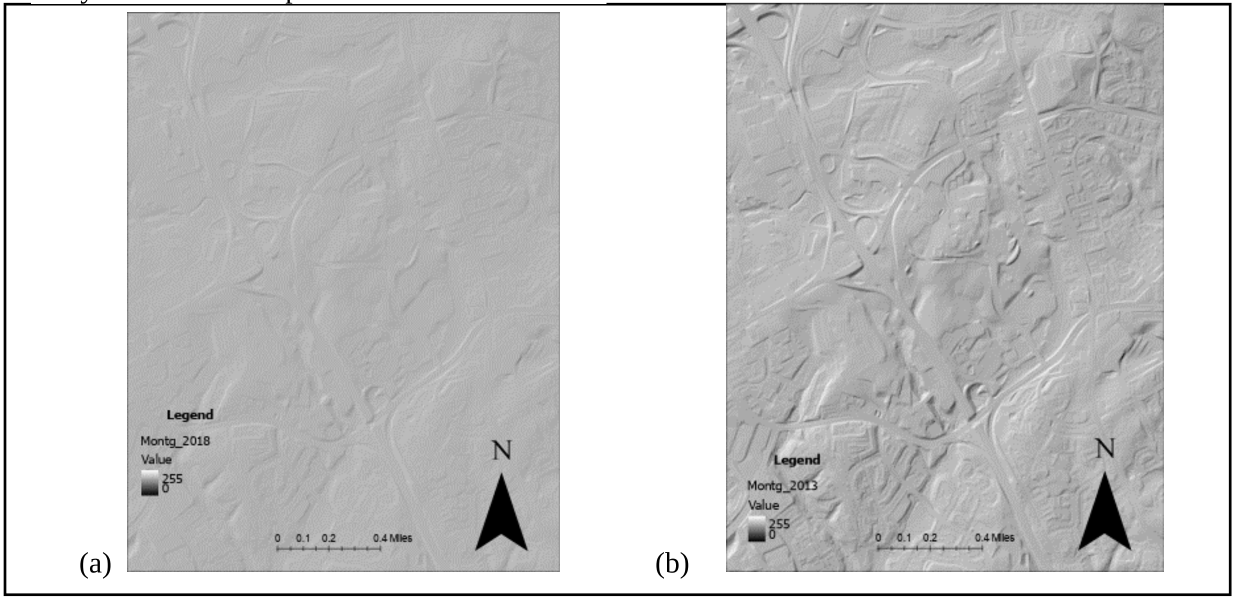

Figure 4.3: Hillshade for Montgomery County for resolution of 0.6m and 1.2m respectively.

4.3.3 InSAR Acquisition and Processing

In this study, we obtained InSAR images from the Alaska Satellite Facility (ASF) (https://search.asf.alaska.edu/#/), which specializes in collecting, processing, archiving, and distributing SAR data. The ASF also provides data recipes, tutorials, and OpenSARlab, offering easy avenues for data processing. We conducted a geographical search of counties on the website and obtained the interferograms of SAR images. The Miami InSAR time-series software in Python (MintPy), developed by [30], was utilized, applying a SBAS approach. MintPy was run on a Jupyter notebook to prepare a Hyp3 Stack (all interferograms) and perform the time-series analysis. We had to subset the stack to the area of interest, establish a high-coherence reference point, analyze the time series, and reduce errors.

The workflow involved inverting the interferogram stack to obtain the raw phase time-series, correcting for deterministic phase components to reduce noise, and estimating the average velocity by excluding noisy SAR acquisitions. In this study, the Sentinel-1 network used small spatial-temporal baselines (max 150 meters spatial, 24 days temporal), with buildings as reference points for calculating relative line-of-sight velocities. This technique allowed for the comparison of images collected from different seasons from 2016 to 2024 over regions including Allegany, Talbot, Montgomery, Baltimore Counties, and Baltimore City to quantify the vertical velocity and changes in the ground surface. More than 100 interferograms from the Sentinel-1 satellite were acquired, each with a 30-meter pixel resolution, covering all specified regions. Figure 4 summarizes the flow of the applied process to perform the InSAR technique.

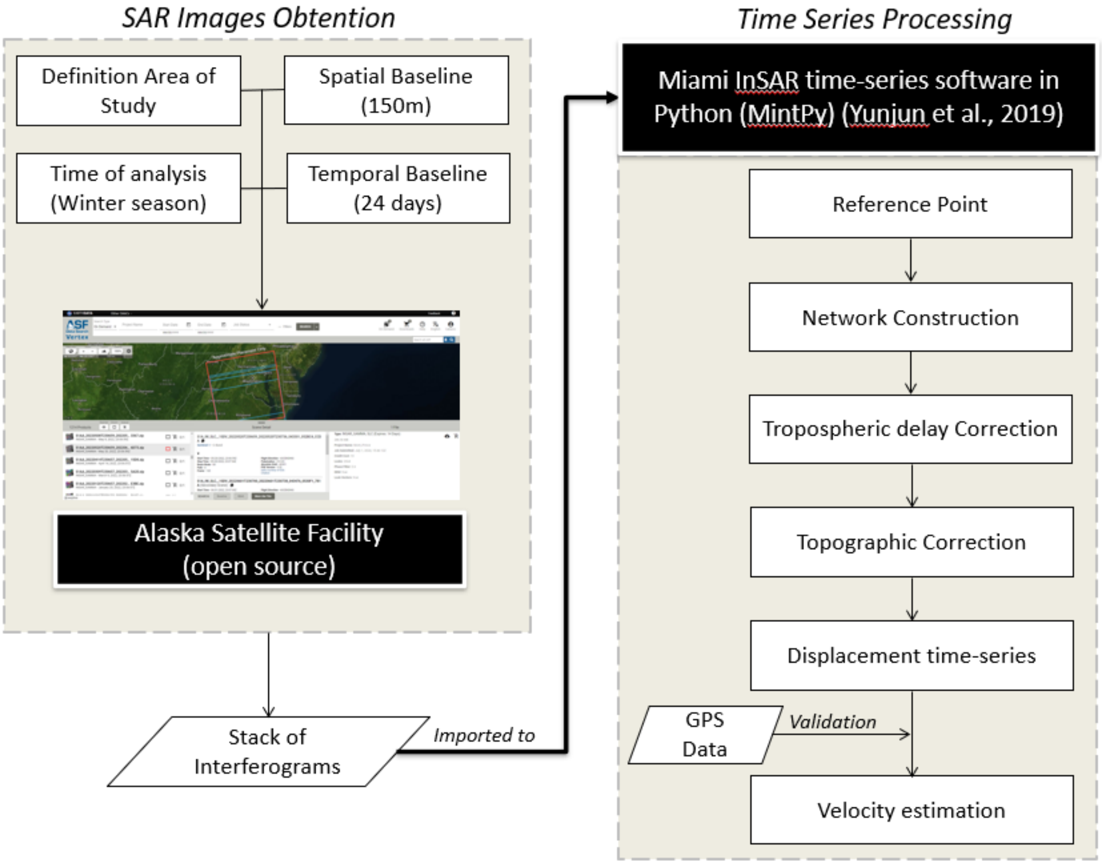

Figure 4.4: InSAR time series process.

Figure 4.5 shows the calculated coherence for each studied county. MintPy evaluated the raw phase by calculating the temporal coherence, using a threshold of 0.7. To avoid outliers from decorrelation, it offers a masking option based on spatial coherence, with a threshold of 0.4 [21]. Tropospheric delay components were not considered in this study. Water bodies were masked out using a DEM-based water mask.

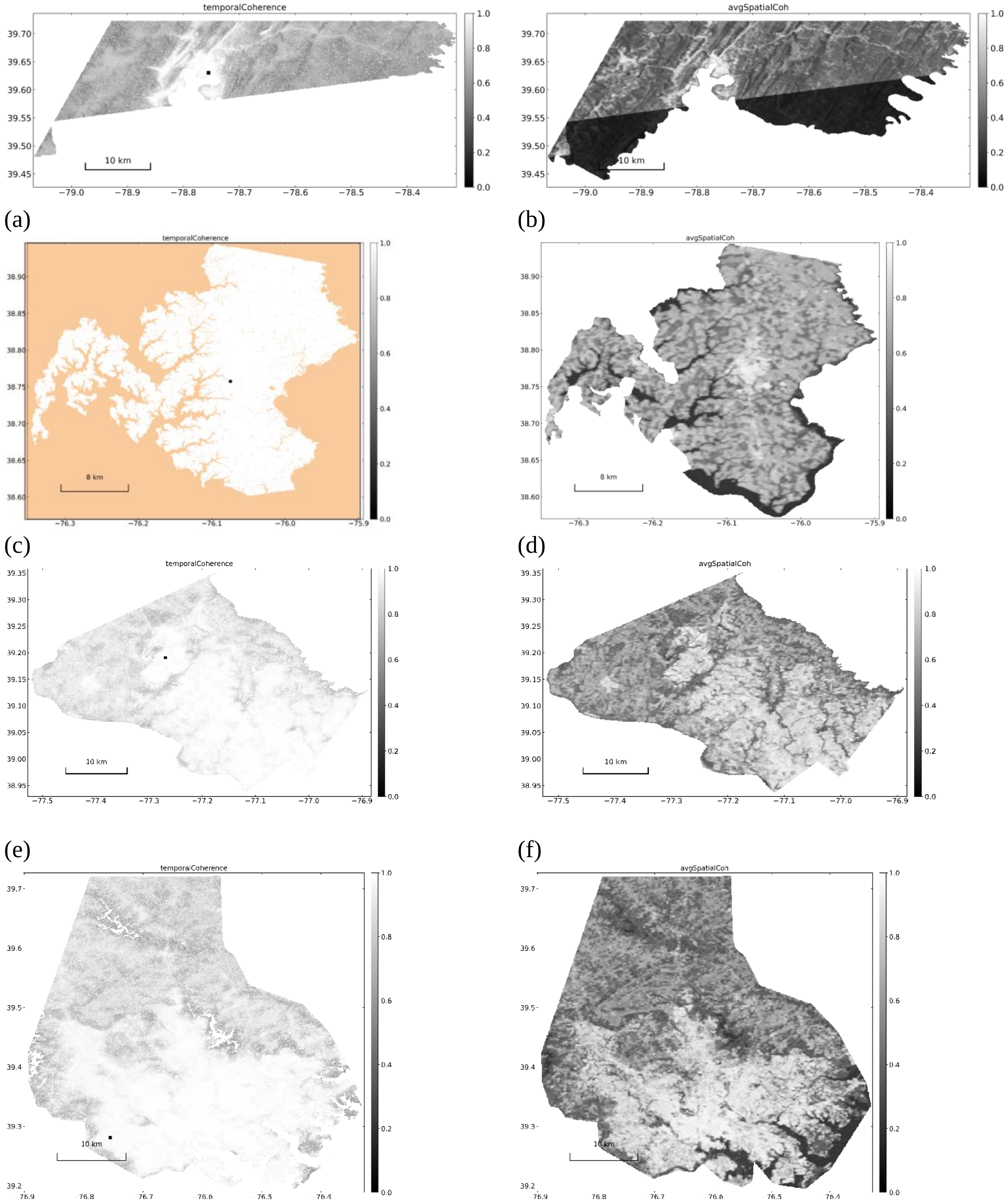

(a) (b) (c) (d) (e) (f) (g) (h)

Figure 4.5: (a) Computed temporal coherence for Allegany County. (b) Computed spatial coherence for Allegany County. (c) Computed temporal coherence for Talbot County. (d) Computed spatial coherence for Talbot County. (e) Computed temporal coherence for Montgomery County. (f) Computed spatial coherence for Montgomery County. (g) Computed temporal coherence for Baltimore County & City. (h) Computed spatial coherence for Baltimore County & City.

4.3.4 Landslide Inventory and Land Use Acquisition

For this study, a record of landslides from the past 20 years was compiled (Figure 4.6). These records are used as a baseline for comparing the results of the Lidar and InSAR assessments. Furthermore, an analysis of the highest vertical velocities from the InSAR process was carried out using ArcGIS and Google Earth tools. This analysis included identifying activities at each site to validate and complement the recorded velocities.

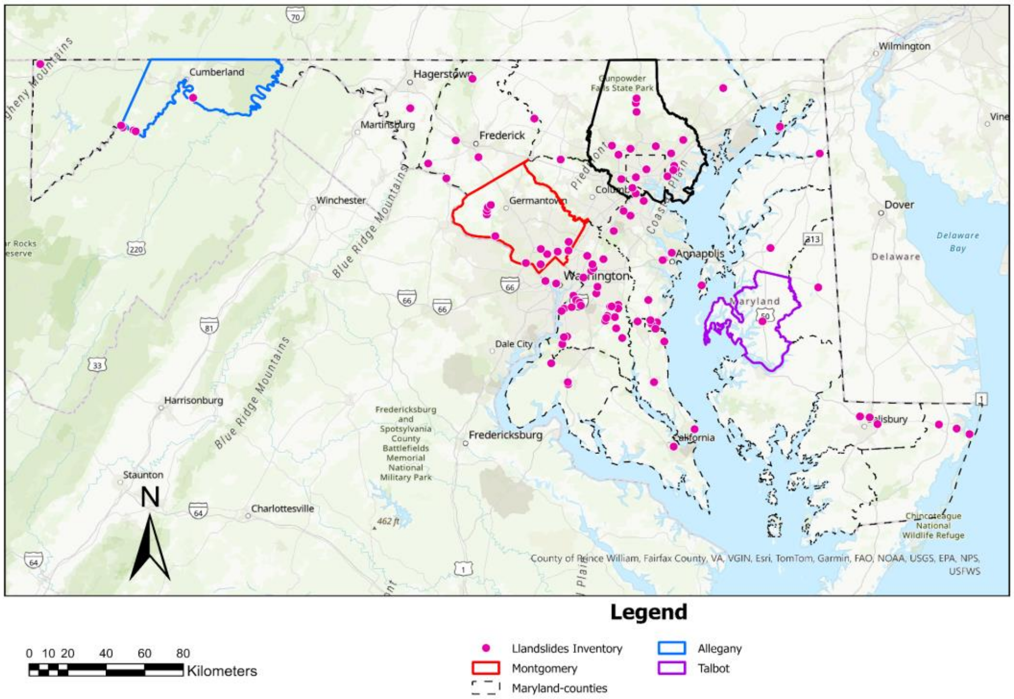

Figure 4.6: Landslides Inventory in Maryland.

Additionally, Land Use and Cover data from the Maryland Department of Planning was obtained to highlight development trends in the study areas. The 2010 update classified 13 types of land use, including various residential densities, commercial and industrial areas, and different land covers like agriculture and forest. These categorizations were used to evaluate the impact of land cover on the rate of ground deformation in some of the studied counties. Figure4.7 illustrates the process followed for land use and landslide inventory assessment, complemented by tools such as ArcGIS Pro and Google Earth Pro software.

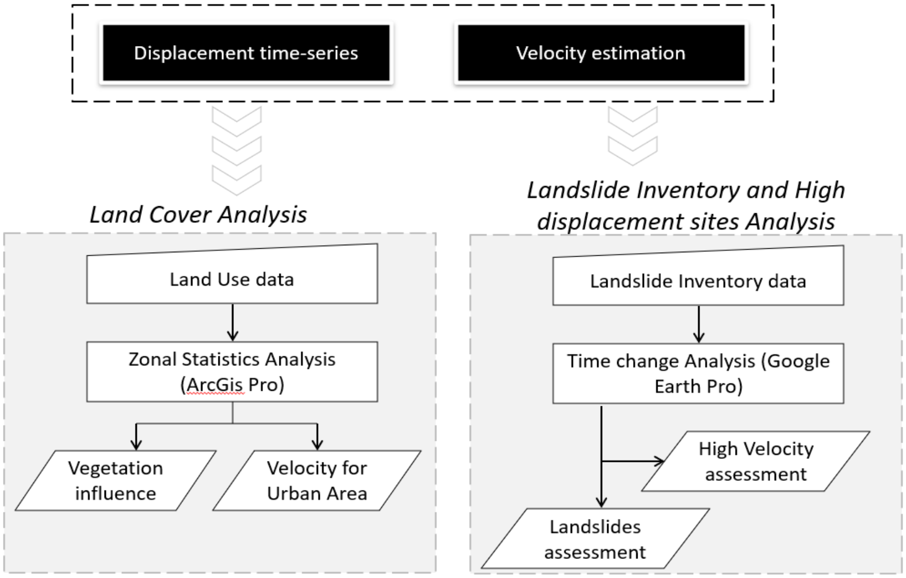

Figure 4.7: Landslides Inventory and Land cover analysis process.

4.4. Results

4.4.1 Lidar Map: Montgomery County

In Figure 4.8, the Lidar data map shows a DEM resolution of 1.2m for 2013 and 0.6m for 2018. Figure 8a presents an elevation range from 18.0764 ft to 589.305 ft, while Figure 8b shows a range from 29.5505 ft to 244.463 ft. The maps indicate that green areas correspond to lower elevations, whereas red and yellow areas represent higher elevations, offering a clear depiction of the county's topography. Both maps emphasize diverse terrain, featuring distinct valleys and elevated regions.

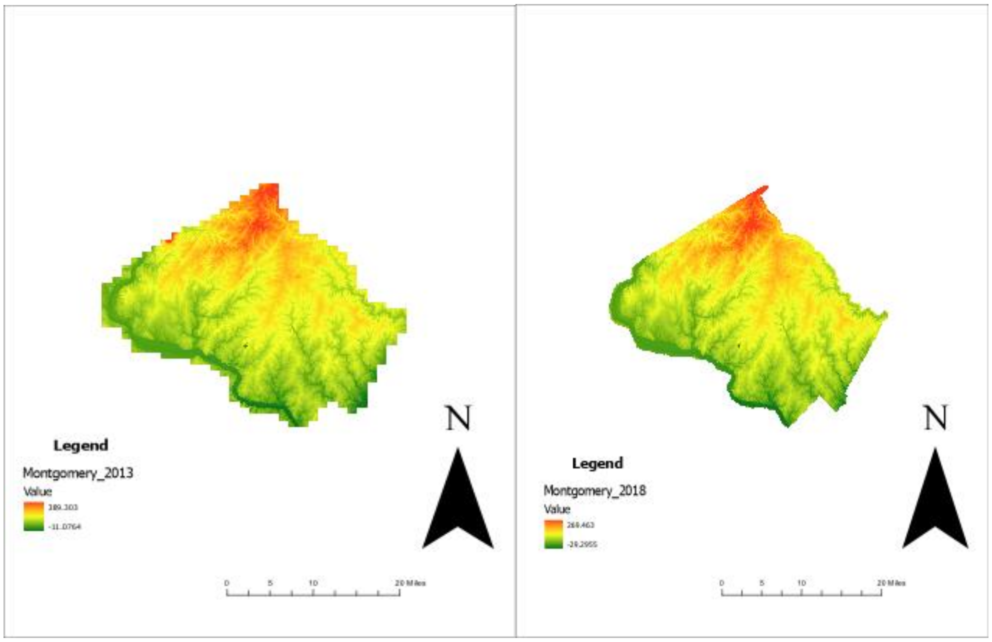

Figure 4.8: Images of Lidar Data Maps obtained.

Figure 4.9a illustrates the Hillshade map from the Lidar data, identifying landslide occurrences, while Figure 4.9b highlights the differences between the Lidar images from 2018 and 2013. The figures display landslide data and elevation changes in Montgomery County. The red dots indicate the geographical distribution of landslide locations within and around the county, providing a visual representation of the spatial distribution of landslides and elevation changes. The field survey reveals GPS coordinates at 39° 03.168' N, -76° 58.611' W.

- Elevation: 400 ft
- Slope Length: 63 ft
- Slope Width: 41 ft
- Slope Angle: 25°

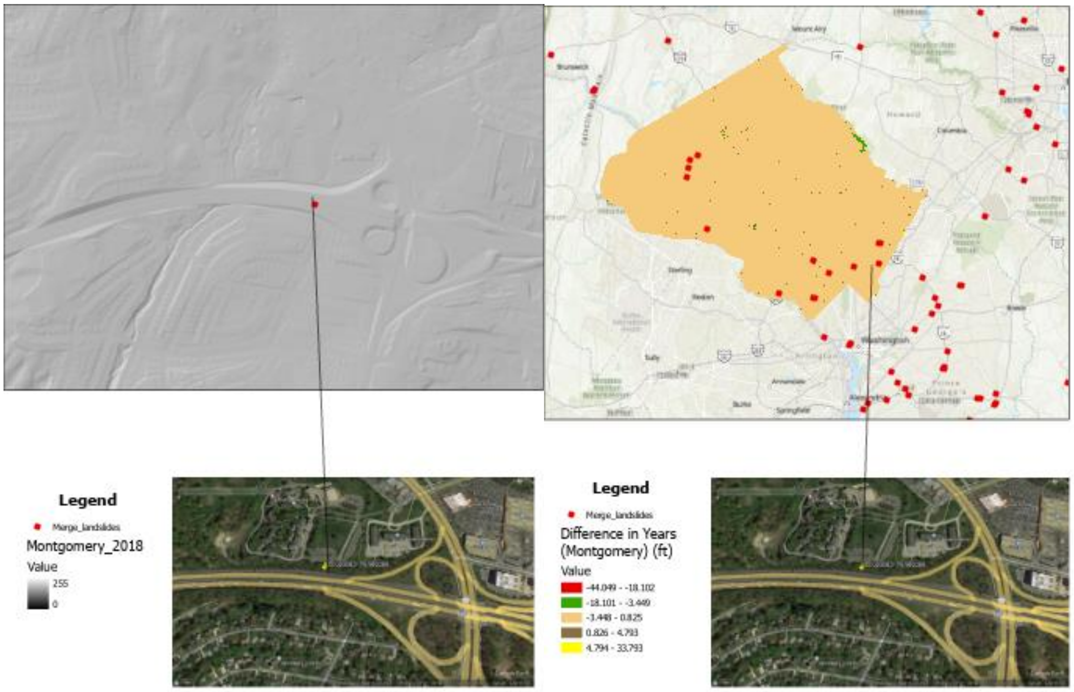

Figure 4.9: Hillshade Map, Landslide data and Elevation Changes.

4.4.2 Slope Map

This map shows the features of the terrain and the steepness of the slopes at a specific location. The image displays a high-resolution topographic depiction obtained from LiDAR data, providing intricate details on the landscape and terrain characteristics. Figure 4.10 highlights areas with varying degrees of slope, which are represented by distinct color gradations. The color scale suggests that the darker shades correspond to steeper slopes, while the lighter areas have gentler slopes. Additionally, the map identifies and outlines an area that is potentially susceptible to slope failure. This information is likely valuable for evaluating and overseeing the stability of slopes in the area. This information is highly significant for the purpose of infrastructure development, hazard mitigation, and risk management in regions that are susceptible to landslides or other geohazards connected to slopes.

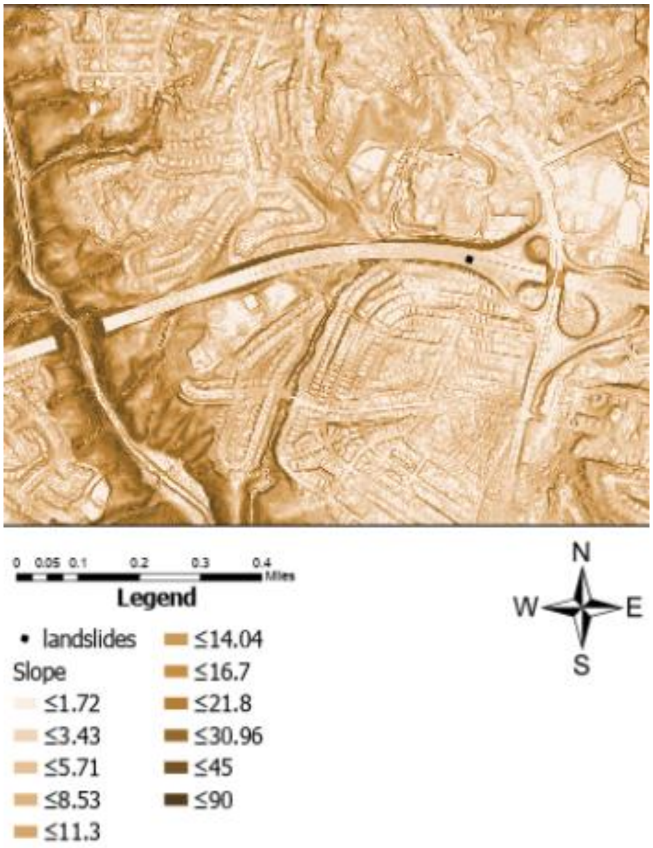

Figure 4.10: Slope Map for an Identified Location.

4.4.3 Geomorphon Landforms

The landform for Montgomery County is shown in Figure 4.11 depicting the representation of landscape based on the difference in elevation. The geomorphological map classifies the land surface based on its shape and features. The map indicates that most of the area consists of spur and slopes, valleys are clearly visible, forming a network across the landscape. The regular pattern and straight lines suggest significant human impact on the landscape, possibly representing urban to suburban development. Overall, the figure shows the distribution of slopes which are prime locations for potential landslides. Also, the relationship between slopes and valleys is evident thus identifying areas where water might accumulate and destabilize slopes. Peaks and ridges were identified which could be areas of concern for rock falls or other types of mass movements.

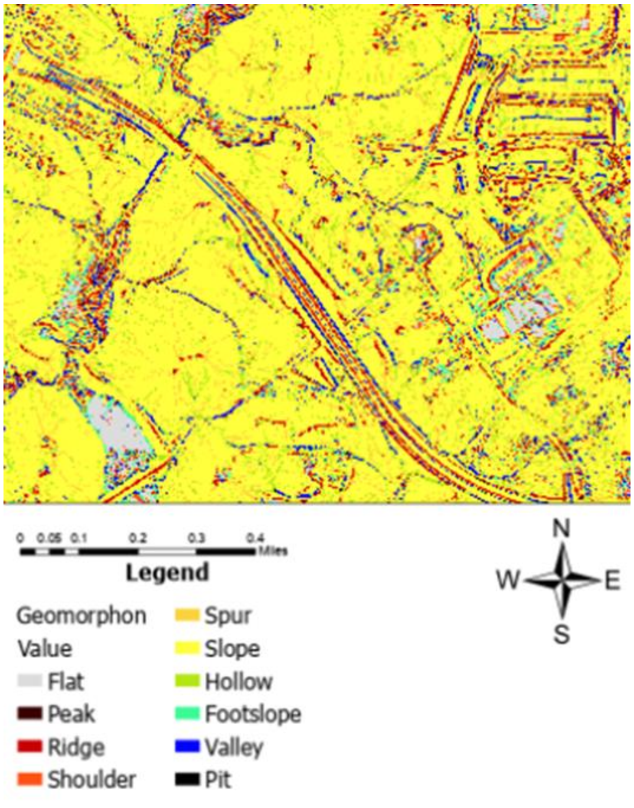

Figure 4.11: Map of the Identified Landslide produced by geomorphons method.

4.4.4 InSAR Analysis

The resulting images represent the vertical velocity change obtained for the studied counties based on the Satellite Sentinel-1 SAR images processed. The negative values tending to blue colors represent land subsidence, while positive signs tending to red colors represent uplift. Additionally, the appendix section (Appendix A) includes displacement graphs for each analyzed county, showing changes over time relative to the respective start dates.

Allegany County

Figure 4.12 shows the resulting vertical velocities derived from the Sentinel-1 satellite, based on 145 processed SAR interferograms from September 9, 2016, to October 21, 2024. From Figure 5 (a) and (b) the areas with coherence higher than the established thresholds are limited, therefore the results exhibit a significant area with no data (blank spaces). It can be observed that the western region exhibits subsidence, while the rest of the area shows a tendency to uplift.

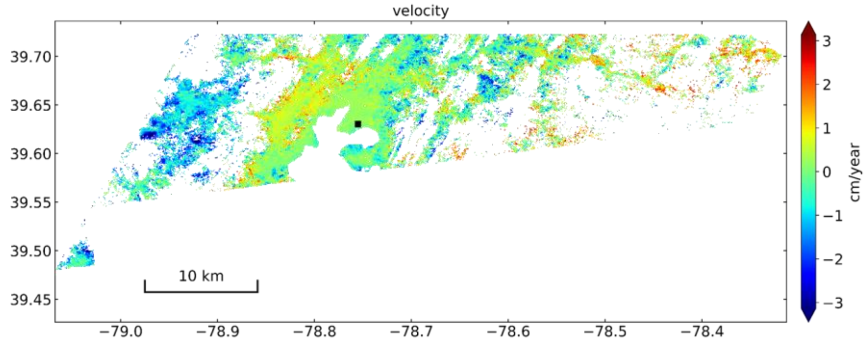

Figure 4.12: Allegany County velocities derived from Sentinel-1 path 145 ascending images (From 2016 to 2024)

In this county, historical landslides occurred in areas with insufficient coherence, making it impossible to assess those sites. However, sites in the western area, where the highest subsidence was recorded, were analyzed and compared with Google Earth timeline imagery. This comparison revealed material exploitation sites, as shown in Figure 4.13. Additionally, the displacement and trend velocity at this site were obtained, demonstrating a vertical change of at least 65 cm over the last 8 years, as shown in Figure 4.14.

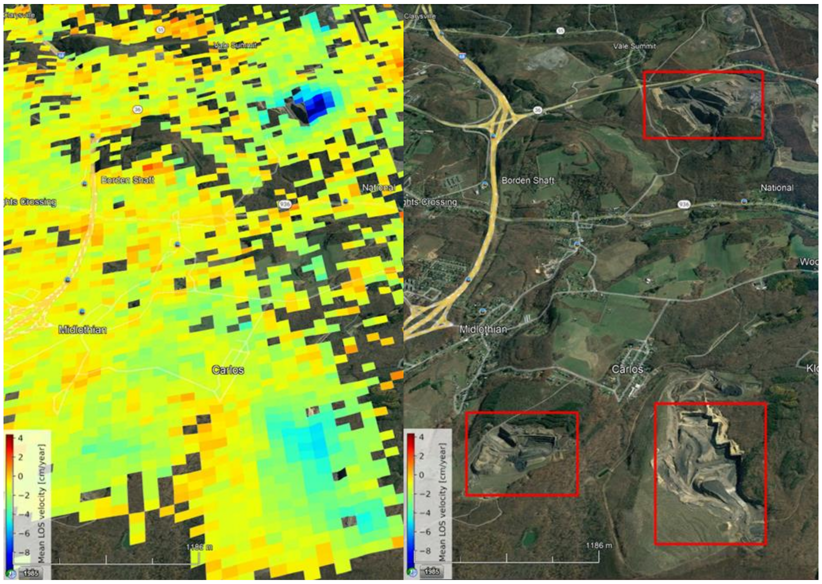

Figure 4.13: Velocity Assessment in Allegany County over highest recorded subsidence sites and Google Earth site recognizance.

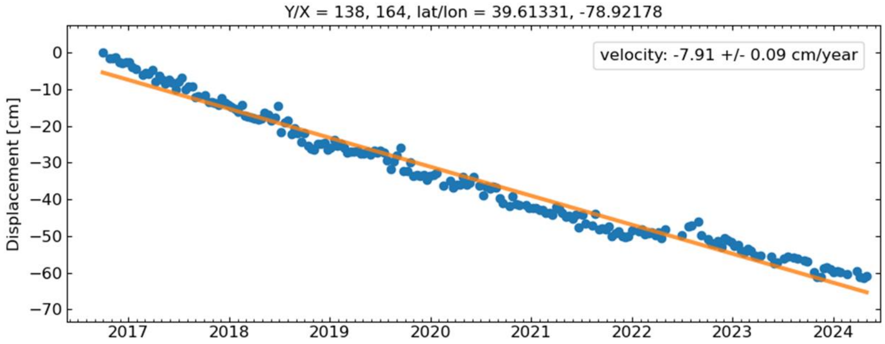

Figure 4.14: Velocity and Displacement Assessment in Allegany County over highest recorded subsidence sites.

Talbot County

Figure 4.15 shows the resulting vertical velocities derived from the Sentinel-1 satellite, based on 214 processed SAR interferograms from October 1, 2016, to December 24, 2023

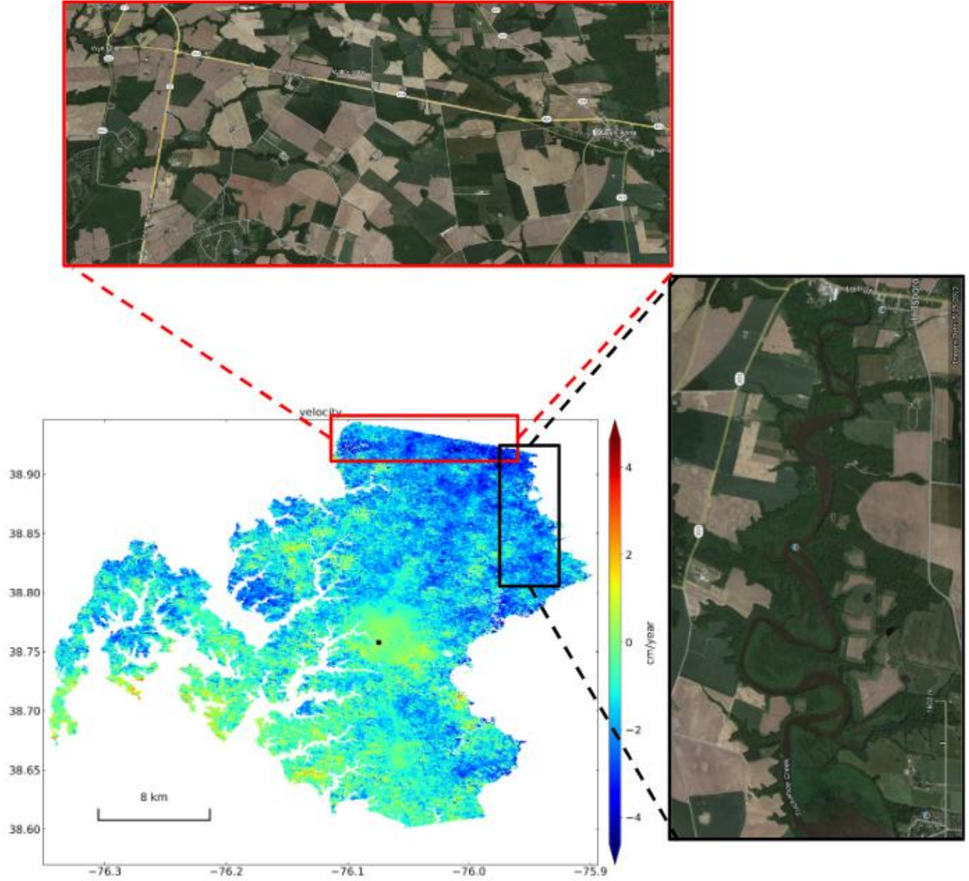

Figure 4.15: Talbot County velocities derived from Sentinel-1 from 2016 to 2024 and Assessment.

From Figures 4.15 (c) and (d), Talbot County exhibits the highest coherence across most of the area, with results indicating a strong tendency toward subsidence and only small areas showing uplift. The mean velocity for the county is approximately -5 mm/year, with a range from -14 to 4 mm/year. The extreme values in the northern region, where marked subsidence occurs, can be attributed to significant agricultural activity and seasonal variations in the meander river level, as illustrated in Figure 15. Similarly, in the southwestern area, which shows a tendency toward uplift, the variations in the bordering river level are influencing the observed trends.

Montgomery County

Figure 4.16 shows the resulting vertical velocities derived from the Sentinel-1 satellite, based on 101 processed SAR interferograms from November 11, 2016, to February 03, 2024. The northwest and eastern parts of the county display notable patterns of both subsidence and uplift. In contrast, the central and southern regions show more uniform changes, with velocities near 0. The maximum observed velocity is 33 mm/year, indicating uplift, while the minimum is -27 mm/year, indicating subsidence.

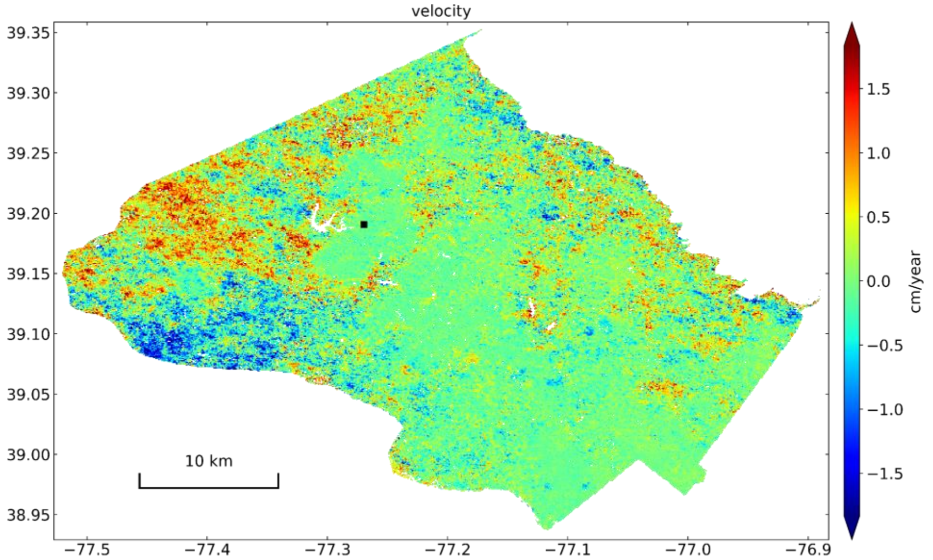

Figure 4.16: Montgomery County velocities derived from Sentinel-1 path 101 ascending images.

Based on the available data of the land cover and use of the county, an assessment was performed to identify and avoid considering velocities potentially affected by existing vegetation. Figure 4.17 shows the resulting map of velocity data, considering areas with vegetation such as forests and agriculture, and the locations of landslides. Figure 4.18 shows the Google Earth imagery of the selected sites with its estimated displacement obtained using the InSAR technique. This method was employed to evaluate known landslide locations and detect any additional significant movements. Since most landslide sites were situated in dense forest areas, only a few could be assessed.

Figure 4.17 shows forested, and agricultural areas directly connected with significant uplift and subsidence velocities, while urban areas exhibit lower velocity magnitudes, ranging from 4.1 to -3.9 mm/year, with an average of -0.1 mm/year. Around 60% of the values indicate subsidence (yellow), while the remaining areas, marked in purple and near green zones, indicate uplift. These findings are consistent with results from a previous InSAR study on subsidence along the US East Coast [24].

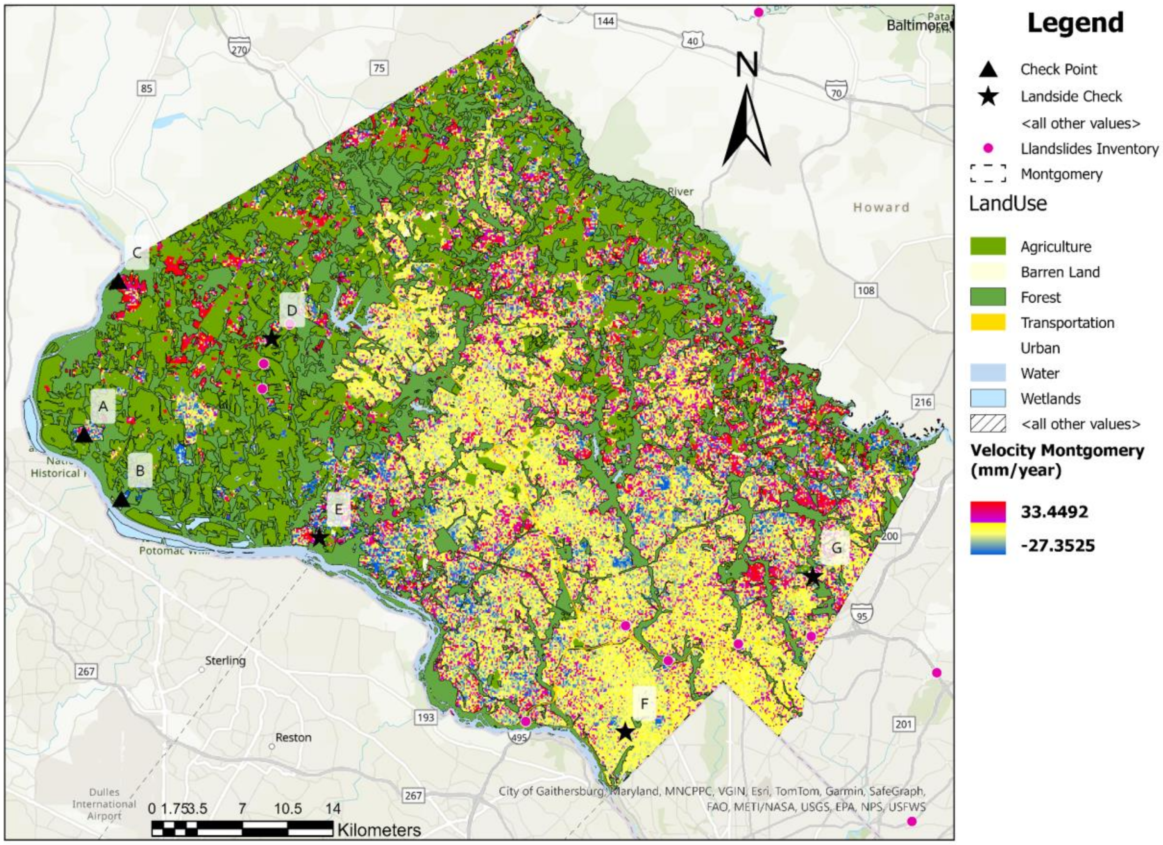

Figure 4.17: Land Cover and Use, Velocity Data, and Known Landslide Locations for Displacement and Velocity Assessment in Montgomery County.

Figure 4.18 evaluates landslides at sites D to G, showing the estimated velocities and displacements from 2016 to 2024. Site D had a velocity trend of -1.7 mm/year with a vertical displacement of about 2 cm. Site E experienced a higher velocity of -5.9 mm/year and a displacement of around 5 cm. Site F had a velocity of -1 mm/year and a displacement of approximately 1 cm. Conversely, Site G exhibited a positive velocity of 6.8 mm/year with a vertical displacement of about 6 cm. Google Earth Timeline observations revealed that sites F and G are significantly influenced by vegetation, which causes greater variability in displacement measurements and affects velocity accuracy. Sites D and E, with cleaner slopes, might still be impacted by the 30m-by-30m pixel size, potentially including vegetation areas in the velocity calculations.

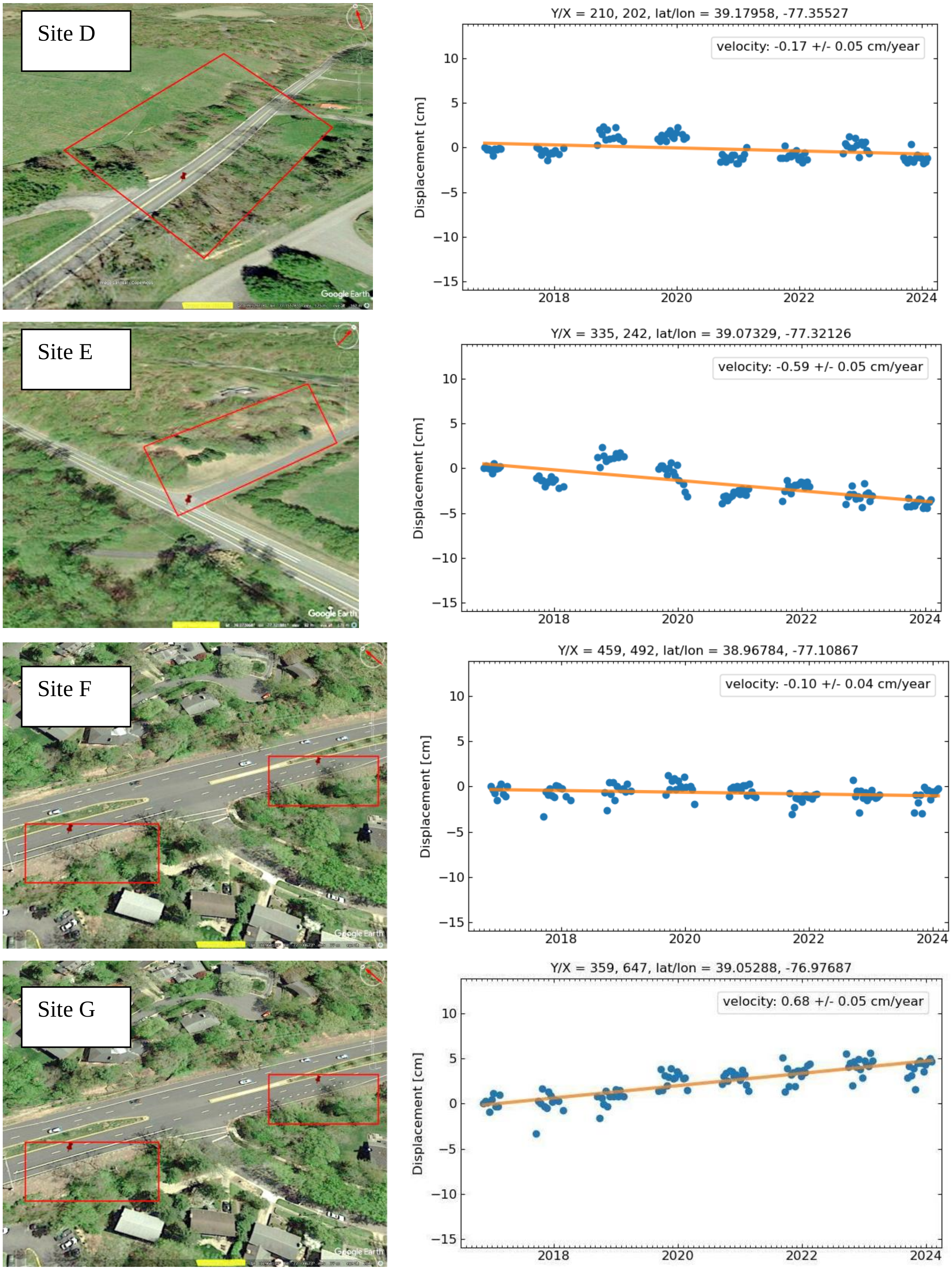

Figure 4.18: Velocity and Displacement Assessment in Montgomery County over Selected Known Landslide Sites.

Figure 4.19 shows the analysis of selected sites with high velocities for uplift and subsidence and correspond to urban areas in the north and northwest region. At Site A, the change rate was approximately 10 mm/year, with a vertical increase of 10 cm. The site evolved from unused land to material storage in 2020 and housing development by 2024. Site B exhibited a velocity of about -14 mm/year and a displacement of around 10 cm, suggesting significant erosion over time influenced by the nearby lake and creek. Site C displayed a velocity of 13 mm/year and a 10 cm displacement. The site, originally a dumpsite for a power plant, expanded over time and was closed by 2024, as shown by a stable velocity trend in recent years.

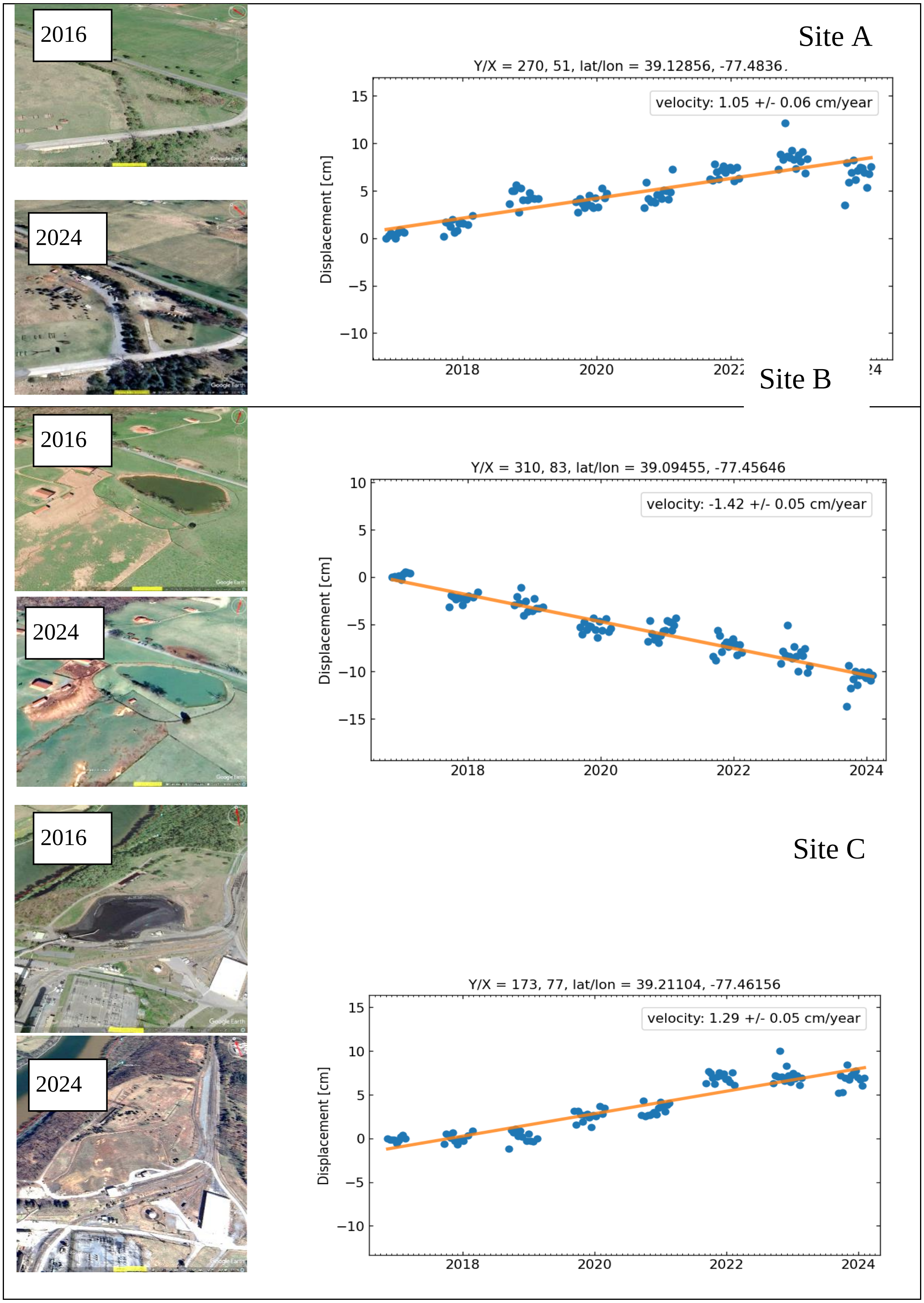

Figure 4.19: Velocity and Displacement Assessment in Montgomery County over selected high measured values; and comparison in google earth for different years.

Baltimore County and City

Figure 4.20 shows the resulting vertical velocities derived from the Sentinel-1 satellite, based on 101 processed SAR interferograms from November 11, 2016, to February 03, 2024. From the central to the north regions of Baltimore, patterns of both subsidence and uplift are highly noted. In contrast, the central and south regions show more uniform changes, with a tendency to subsidence. Additionally, the comparison and validation with GPS stations available from The Nevada Geodetic Laboratory GPS Network Map is shown in this figure.

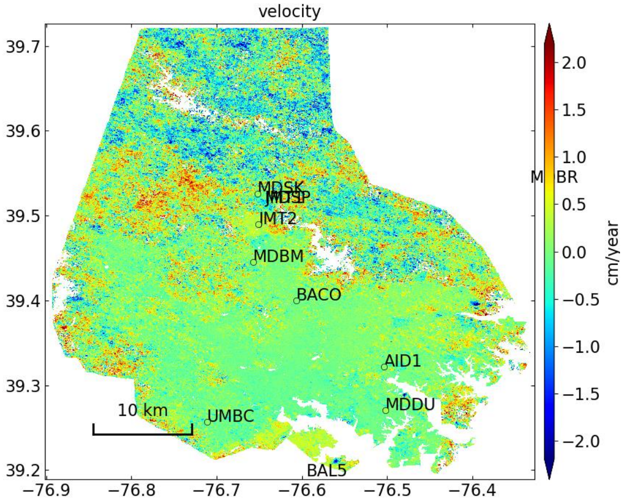

Figure 4.20: Baltimore County and city velocities derived from Sentinel-1 path 101 ascending images (Winter season 2016–2024) and GPS stations in the area.

Figure 4.21 demonstrated the direct connection of forested and agricultural areas with the zones of major uplift and subsidence velocities, while urban areas exhibit lower velocity magnitudes, with a mean value of -0.7 mm/year and a standard deviation of +/-2.2 mm/year. More than 60% of the urban areas indicate subsidence (yellow), while the remaining areas marked in purple indicate uplift. These findings are consistent with results from a previous InSAR study on subsidence along the US East Coast [16].

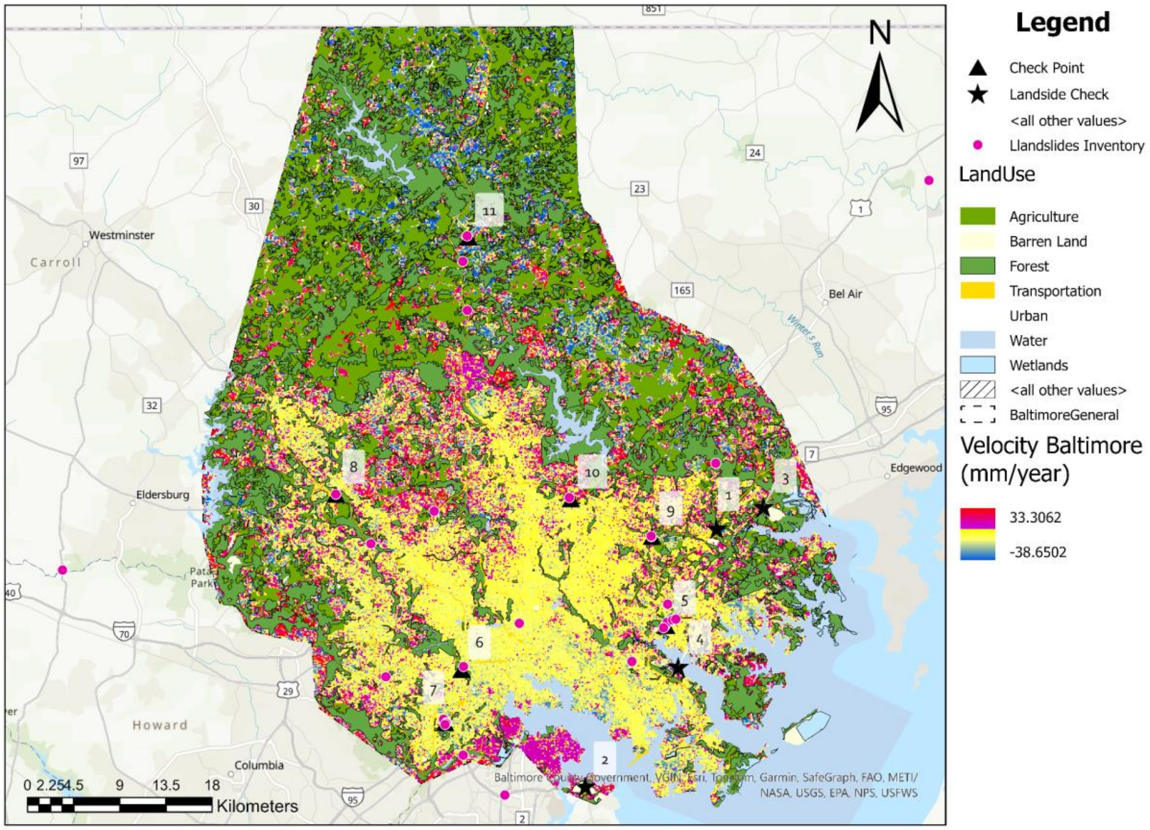

Figure 4.21: Land Cover and Use, Velocity Data, and Known Landslide Locations for Displacement and Velocity Assessment in Baltimore County and City.

Figure 4.22 and 4.23 shows the Google Earth imagery of the selected locations from the landslides inventory with its estimated displacement obtained using the InSAR technique. It evaluates the estimated velocities and displacements from 2016 to 2024. Site 5 had a velocity trend of -11 mm/year with a vertical displacement of about 8 cm. Site 6 experienced a velocity of -8 mm/year and a displacement of around 5 cm. Site 7 had a velocity of -4.4 mm/year and a displacement of approximately 4 cm. Site 8 exhibited a velocity of -3 mm/year with a vertical displacement of about 1 cm. Site 9 had a velocity trend of -1.7 mm/year with a vertical displacement of about 1 cm. Site 10 had a velocity trend of -2.1 mm/year with a vertical displacement of about 2 cm. Site 11 had a velocity trend of -8.8 mm/year with a vertical displacement of about 6 cm.

Despite the resulting displacement reflecting slow movement with negative vertical change, commonly known as subsidence, this can be used to assess slope changes at sites where landslides have been recorded. The displacement graphs often show scattered points, which may represent times of failure or repair. For instance, site 10 experienced a failure in 2019, according to Google Earth imagery, and reinforcement was introduced in 2022, which is reflected in the displacement plot. Therefore, while scattered points can indicate large movements, the overall trend should still be considered as the subsidence velocity of the area.

Additionally, Google Earth Timeline observations show that the sites are significantly influenced by vegetation, which can cause variability in displacement measurements and affect velocity accuracy. In contrast, site 6, where the slope has been exploited and reshaped, shows higher displacement and velocity, effectively representing the more significant changes in that area.

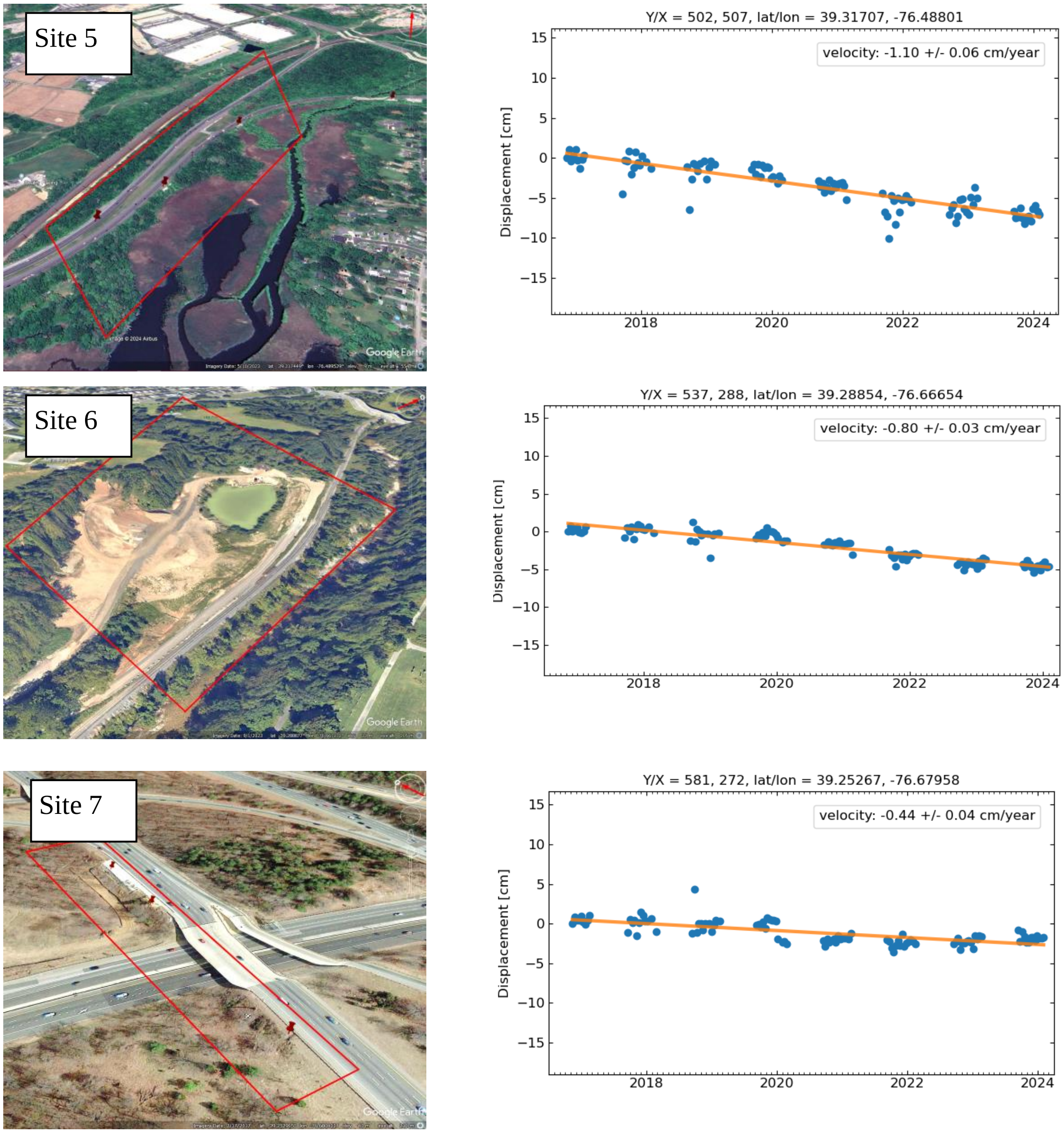

Figure 4.22: Velocity and Displacement Assessment in Baltimore County over Selected Known Landslide Sites 5, 6 and 7.

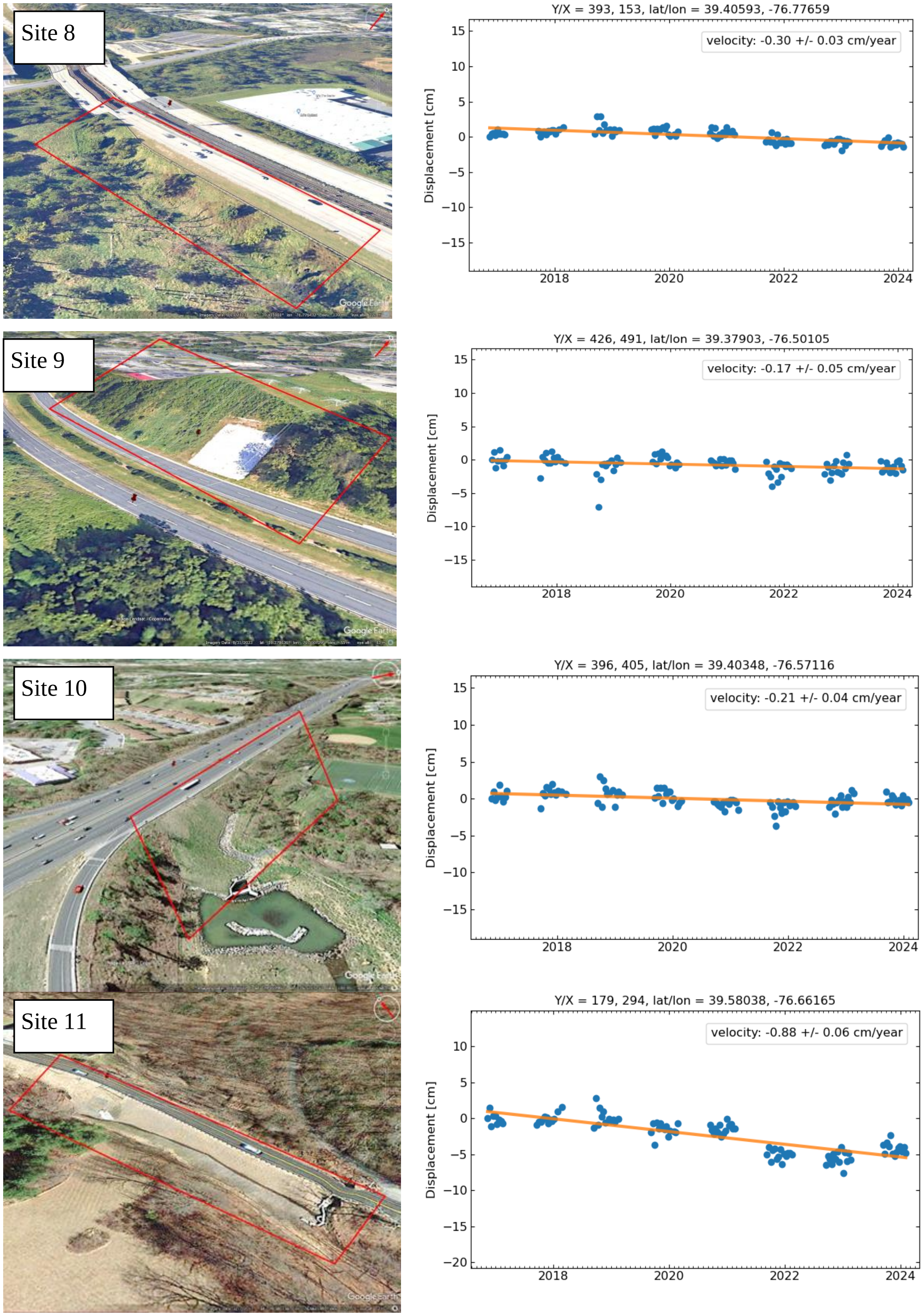

Figure 4.23: Velocity and Displacement Assessment in Baltimore County over Selected Known Landslide Sites 8 through 11.

Figure 4.24 and 4.25 shows the analysis of selected sites with high velocities for subsidence. At Site 1, the change rate was approximately -18 mm/year, with a vertical decrease of 14 cm. Site 2 exhibited a velocity of about -18 mm/year and a displacement of around 15 cm. Site 3 displayed a velocity of -26 mm/year and an 18 cm displacement. Similarly, Site 4 exhibited a velocity of about -26 mm/year and a displacement of around 25 cm. All these sites correspond to landfills of different materials that are in constant re-accommodation. This is represented by the scattered displacement graphs, but the overall negative trend may be reflected due to weight or subsidence in the area.

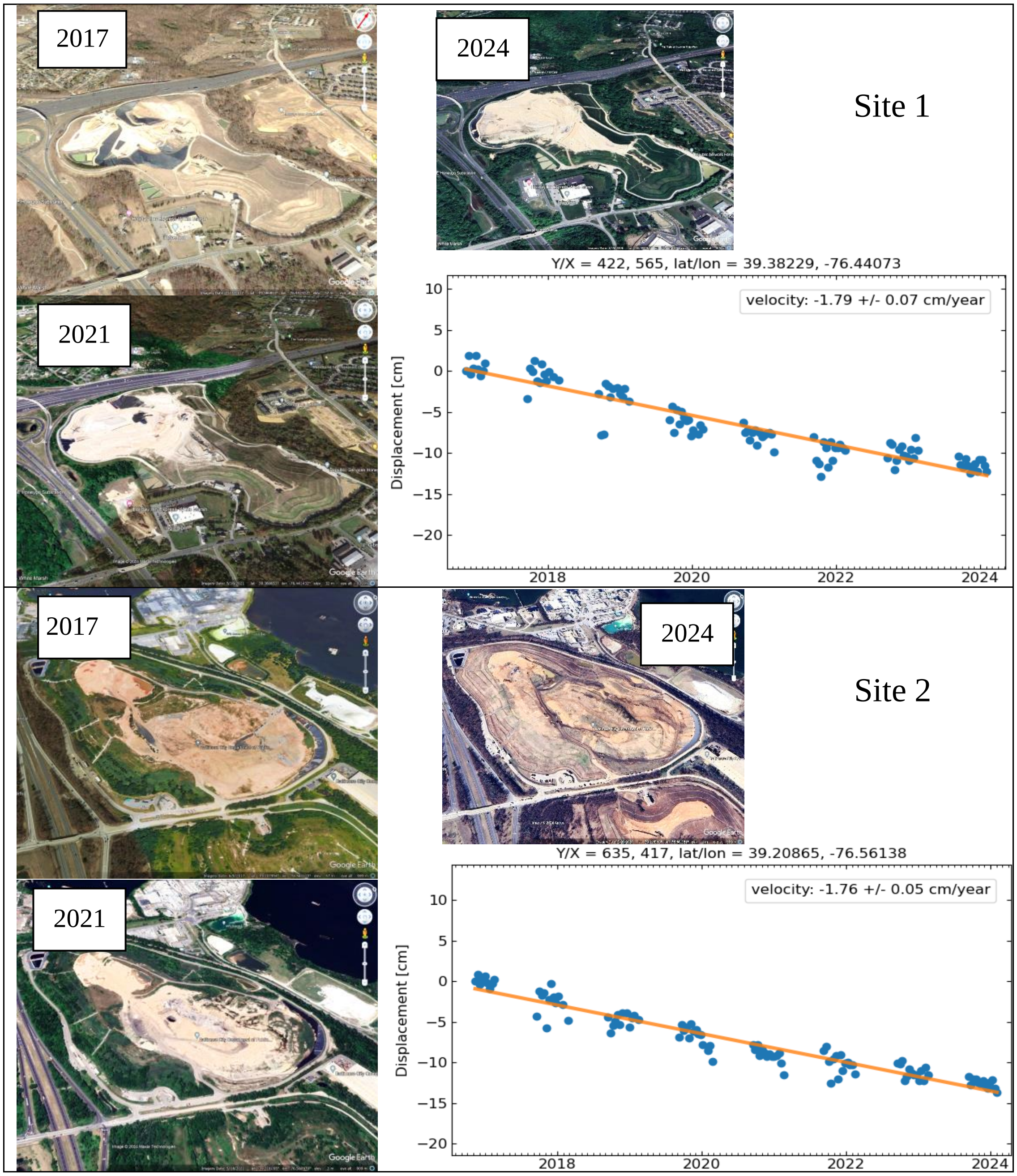

Figure 4.24: Velocity and Displacement Assessment in Baltimore County over selected sites 1 and 2; and comparison in google earth for different years.

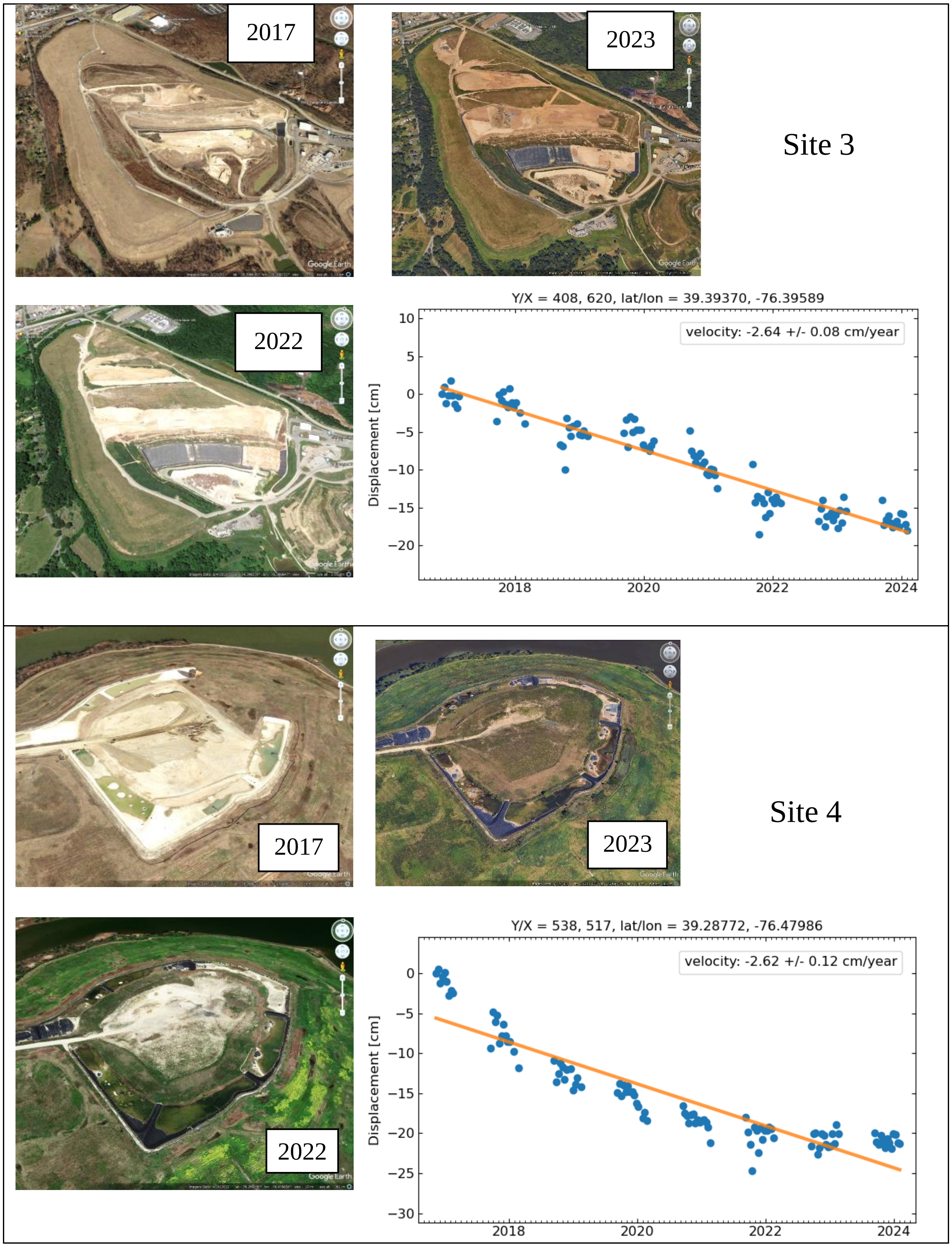

Figure 4.25: Velocity and Displacement Assessment in Baltimore County over selected sites 3 and 4; and comparison in google earth for different years

4.5 Conclusions

The study demonstrated the efficacy of using LiDAR and InSAR techniques to identify and analyze potential slope failures in Montgomery and Baltimore County.

The LiDAR data provided high resolution topographic maps, while InSAR data provided the monitoring of ground deformation over a period.

The assessment of different counties through InSAR technique allowed us to recognize the benefits and limitations of this technique in the ground change study. First, the importance of access to the Satellite data and the accuracy of it, has major significance due to the impact over a time series analysis, which is directly related to the coherence with the SAR imagery. This tool facilitated site reconnaissance across various Counties and helped identify areas that have been used for the management, removal, or filling of significant amounts of material. Examples include the quarry sites in Allegany and multiple landfill sites in Baltimore. Additionally, it identified natural slopes undergoing erosion in Montgomery. These sites cover large areas, making them prominent in the analysis and overcoming the cell pixel size limitations of InSAR resolution. Although these sites may be operating at rates higher than the measured values, the tool was instrumental in locating them. Coupled with Google Earth tools, it provided a comprehensive understanding of the dynamics and activities occurring in these areas. This combination allows for a better assessment of changes and movements, highlighting the utility of integrating various tools for effective monitoring and analysis.

A significant finding from this analysis was the direct relationship between land use and the higher measured velocities. This reflects the substantial influence of vegetation when using InSAR techniques. In areas like Montgomery and Baltimore, the satellite waves' penetration capacity was affected by forest density, often measuring the forest canopy height rather than the ground surface. This highlights the need to account for vegetation cover when interpreting InSAR data to ensure accurate assessment of ground deformation. Meanwhile, in urban areas, the analysis confirmed that a significant portion was undergoing subsidence. The estimated velocity range aligned with the results from a previous InSAR subsidence study in this region [24].

In reference to the assessment of the landslide inventory, it was observed that significant site displacement was registered at specific times, generating scatter plots. However, these specific measures can be influenced by various factors and may not solely represent landslide performance. In many cases, the estimated velocity values fall within the range of the site's subsidence, which may not reflect the actual velocity of slope movement. This indicates that the InSAR pixel resolution may not be sufficient to capture significant land deformation over the small dimensions of landslides. Consequently, while InSAR is a valuable tool, it has limitations in detecting and accurately assessing the dynamics of smaller-scale landslide events.

The study’s results revealed that the use of the remote sensing techniques facilitated a more extensive comprehension of the topography, patterns of surface deformation, and potential mechanism of failure. This technique can aid the development and implementation of tailored mitigation plans to improve public safety and the resilience of infrastructure.

4.6 Future Research

Below are some investigative tasks:

The current study focused on one of the identified landslides in the Montgomery region. Future research will broaden the geographical scope to encompass a wide area or other regions that are known to have slope stability issues.

Explore combining InSAR with LiDAR to enhance the detection and analysis of small-scale landslides and subsidence. Integrating LiDAR's high-resolution topographic data with InSAR’s wide-area displacement measurements could improve the accuracy and detail of ground deformation assessments. This combined approach would help address the limitations of InSAR in detecting small-scale movements and the effects of vegetation.

Future research will focus on the development of resilient algorithms that can automatically combine multi-temporal LiDAR data with other remote sensing techniques to conduct thorough slope stability assessments. Exploring the possibility of utilizing machine learning to detect and monitor slope stability could simplify the processing and analysis of data, thus making slope stability evaluations more effective and adaptable.

Chapter 5

5 Precipitation – triggering factor for slope instability

Atieh Hosseinizadeh, Fauziyah Isola, Zhuping Sheng, Yi Liu, Oludare Owolabi

5.1 Background

Landslides represent a significant geohazard that poses risks to human lives, infrastructure, and ecosystems. These mass movements of rock, soil, and debris can be triggered by various factors, including heavy rainfall events that saturate the soil and reduce its stability [31, 32]. The combination of steep slopes, weak geological formations, and intense precipitation events creates conditions conducive to landslide initiation. Understanding the mechanisms underlying landslide hazards is crucial for effective risk assessment, early warning systems, and land use planning to mitigate potential impacts on communities living in landslide-prone areas.

Challenges posed by rainfall-induced slope failures are particularly pronounced in regions with abundant rainfall, and this issue is exacerbated during periods of intense precipitation attributed to climate change [33 - 37]. The significance of rainfall as a pivotal factor in landslide occurrence is emphasized in the literature [38, 39]. The intricate interplay between rainwater infiltration and runoff assumes a crucial role in determining slope stability, impacting both unsaturated and saturated zones [40, 41]. Rainfall infiltration has the potential to jeopardize slope stability by modifying suction in the unsaturated zone and elevating pore pressure in the saturated zone [42]. This dual influence on soil conditions markedly contributes to the vulnerability of slope failure [43 - 45].

In studies concerning rainfall-induced slope instability, the precise assessment of infiltrated water is often oversimplified. Traditionally, it has been common to either consider the entire rainfall volume as equivalent to infiltrated water or estimate a percentage of rainfall, disregarding the angle of the slope, as a proxy for infiltrated water. These assumptions introduce errors in calculations, particularly in regions with heavy rainfall, yielding less reliable results [42]. These simplifications contrast with considerations such as equating rainfall infiltration to rainfall intensity or factoring in the component of rainfall intensity perpendicular to the slope boundary. These assumptions are particularly problematic and leading to less reliable results in regions with heavy rainfall because the amount of infiltration is really smaller than rainfall [46]. To address this, a numerical simulation model is proposed in this study to concurrently consider surface and subsurface flow, acknowledging their complex interactions as intricate environmental systems.

5.2 Literature Review

5.2.1 Reviewed Papers on Hydrological Models

Belhadj et al. [47] utilized 16 months of hourly measurements of rainfall and flow rates, a six-parameter conceptual model was developed to simulate rainfall-induced infiltration in a small sewer system. Sensitivity analysis demonstrated the model's effectiveness under various calibration conditions but revealed high parameter interactions, posing a potential limitation for specific model applications. When applied to another sewer network, the model showed good agreement between observed and simulated flows. However, further validation on other sites is needed to confirm its suitability.

Chu & Mariño [48] developed a new infiltration model, based on the Green–Ampt approach, for simulating infiltration into nonuniform/uniform soils with arbitrary initial moisture distributions during steady/unsteady rainfall events. The model accommodates ponding and non-ponding conditions and transitions between them. It was tested against different cases, showing good agreement with field measurements and existing models. The developed model addresses limitations in previous Green–Ampt-based models, offering a generalized algorithm for determining ponding conditions and simulating infiltration. The study focused on the vertical variability in soil hydraulic properties and complex changes in rainfall intensities. Evaporation/evapotranspiration and soil water redistribution were considered insignificant in this study but will be explored in future studies on infiltration into layered soils under complex rainfall patterns.

Ebel [49] employed an infiltration model to analyze seven years of post-fire infiltration measurements and their temporal correlations with soil-hydraulic properties in the Colorado Front Range, USA. Utilizing point-scale Green-Ampt simulations across diverse rainfall events, the study assessed variations in infiltration and surface runoff generation thresholds over time since the fire. Both measured and simulated infiltration consistently demonstrated a progressive recovery trend with increasing time since the fire. This underscores a diminishing vulnerability to infiltration-excess runoff generation over time, with the most pronounced risk observed in the initial two-years post-fire. Importantly, the study highlights that the infiltration model effectively captures these dynamics, revealing how the threshold for infiltration-excess runoff shifts over time. By the third year following the wildfire, only extreme events lead to surface runoff, and by the fifth and seventh years, even extreme rainfall fails to generate surface runoff according to the model's simulations.

Hawkins & Cundy [50] establish an envelope for the steady-state surface runoff response on a hillslope, considering the probability distribution and spatial arrangement of individual point infiltration capacities along with rainfall intensity. The analysis reveals that minimum overland flow occurs when point infiltration capacities are ordered with the highest at the slope bottom, while maximum overland flow happens when the highest point capacities are at the top of the slope. Equations for envelope curves are developed for both continuous distributions and discretely sampled data, with provided examples for each case. The study discusses the application of this analysis as a rainfall-runoff model.

Jain et al. [51] explored a research study aiming to assess the inherent representation of physical processes in a watershed within a trained Artificial

Neural Network (ANN) rainfall-runoff model. The investigation involves analyzing statistical measures of the strength of the relationship between the disintegrated hidden neuron responses of the ANN model and its input variables. Additionally, deterministic components of a conceptual rainfall-runoff model are considered. The case study focuses on the Kentucky River watershed. The findings suggest that the distributed structure of the ANN effectively captures certain physical behaviors of the rainfall-runoff process. The hidden neurons in the ANN model approximate various components of the hydrologic system, including infiltration, base flow, delayed and quick surface flow, etc.

Mardhel et al. [52] Determined the spatial distribution of infiltration and runoff that is achieved through the IDPR (Network Development and Persistence Index). This index applies a specific metric to assess the disparities between the theoretical drainage system, generated by automated analysis of a digital model, and the actual field representation marked by branching rivers. The metric measures the difference between a simplified model of water pathways, assuming homogeneous and isotropic terrain, and the intricate network observed in nature, influenced by the properties of the land surface it traverses.

Qi et al. [53] compared four surface runoff and infiltration partition methods—Daily Curve Number (DCN-RSWAT), Hourly Curve Number (HCN-RSWAT), Green-Ampt (GA-RSWAT), and Effective Infiltration Capacity (EIC-RSWAT)— within a Richards-equation-based SWAT model (RSWAT). These versions, along with a Daily Curve Number based original SWAT (DCN-SWAT), were applied to simulate daily stream flow and baseflow from 2001 to 2015 in two watersheds. Global sensitivity analysis and the Sequential Uncertainty Fitting algorithm were employed to identify sensitive parameters and analyze uncertainty. The results emphasize the sensitivity of watershed modeling to differences in surface runoff and infiltration partition methods. DCN-RSWAT outperformed other versions and the standard SWAT model, exhibiting reduced flow rate prediction uncertainty and improved simulation of daily baseflow in both test watersheds. The study aims to inform better practices in selecting these methods for SWAT and other watershed models, contributing to sustainable water resources assessment and management.

5.2.2 Reviewed Papers on Investigation Slope Instability and Landslide

Cho and Lee [54] explained that landslides triggered by rainfall usually occur when surface soils become saturated, leading to a loss of matric suction near the surface. They discussed a technique by Pradel and Raad for predicting such slope failures. For a rainfall-triggered landslide to happen, the rainfall intensity must exceed the infiltration capacity, and the duration of rainfall must exceed a certain minimum period. The authors indicated that by understanding this, along with the hydraulic properties of the soil, it becomes possible to create a rainfall intensity curve that identifies a rainfall event capable of causing landslides.

Chleborad et al. [55] used the empirical rainfall thresholds to predict landslides in Seattle. A formula combining rainfall over 3 days and 15 days was developed from historical data. This formula captures over 90% of historical landslide events. However, additional criteria are needed for confident forecasting. Another threshold based on rainfall intensity and duration predicts a higher probability of landslides but fewer occurrences. Both thresholds must be used together for effective landslide forecasting in Seattle.

Godt et al. [56] presented an empirical method to predict shallow landslides by analyzing 25 years of rainfall data and landslide occurrences. Our approach combines a water balance to gauge moisture conditions and a rainfall intensity-duration threshold to identify potential landslide periods. While successful for widespread events, the accuracy is lower for isolated landslides.

Guzzett et al. [57] collected data on 2,626 rainfall events that caused shallow landslides and debris flows from around the world. By analyzing the relationship between rainfall intensity and duration, they found that as rainfall lasts longer, less intense rain can trigger slope failures. They identified the minimum rainfall needed to start shallow landslides and debris flows. They used statistical methods to create a threshold curve based on the rainfall data.

Aydilek and Ramanathan [58] created a soil management system (SMS) for Maryland by combining GIS data and map overlays. They used these data maps to find potentially unstable highway slopes through spatial and statistical analysis. Their approach involved a semi-quantitative index overlay method to evaluate slope stability. They also used a qualitative index overlay to understand past instability events and identify slopes with similar conditions that could be at risk of failure.

Pennington et al. [59] examined the impact of prior rainfall on landslides in the UK. A notable rise in landslides during 2012-2013 due to heavy rainfall emphasized the role of hydrogeological factors. To plan and respond effectively, accessible indicators of potential landslides are crucial. The study explores whether past effective rainfall can predict landslide likelihood. Long-term antecedent precipitation is important for all landslides, while small ones follow heavy rainfall quickly. Deeper, rotational landslides take longer due to complex hydrogeological responses. Analysis of data and weather records aids in predicting landslide probabilities. This research contributes to tools for anticipating regional landslides in the UK.

Ramanathan et al. [60] introduced a framework for studying slope instability in Maryland. Using a GIS database, 48 slope failures were examined to find links between physical characteristics and instability patterns. Six factors were analyzed for their impact on soil slope stability near highways: event precipitation, geological formation, land cover, slope history, ground slope, and elevation. Combining GIS data for these factors reveals noteworthy trends and significant correlations.

Lee et al. [61] aimed to establish the criteria for a landslide early warning system (LEWS) by deriving optimal thresholds for the cumulative event rainfall–duration (ED) and identifying the characteristics of the rainfall variables associated with a high probability of landslide occurrence via a Bayesian model. The study uses rainfall and landslide data for Chuncheon, Republic of Korea.

Bezak & Mikoš [62] evaluated changes in the frequency and intensity of rainfall events above selected empirical rainfall thresholds at the pan-European level. The study focuses on areas classified as at least moderately susceptible to landslides and evaluates changes for the 1961–2018 period using regional rainfall reanalysis data.

Abraham et al. [63] attempts to improve the performance of conventional meteorological thresholds by considering the effect of soil moisture, using a probabilistic approach. The study focuses on Idukki district in southern India, which is highly susceptible to landslides.

5.2.3 Reviewed Papers on Slope Instability by Considering the Role of Infiltration

Numerous studies have delved into the risks of slope instability by considering the role of infiltration. Chiu et al. [64] developed a custom model that integrates the shallow water equation with Richards' equation to evaluate landslide potential using an infinite slope stability analysis. Their simulation, based on actual catchment topography, demonstrated variations in runoff and safety factors during storm events. Dolojan et al. [65] combined the Green-Ampt infiltration equation with an infinite slope stability model to study shallow slope failures induced by rainfall, taking into account rainfall intensity, soil characteristics, and topography. They used the modified Green-Ampt equation to estimate infiltration capacity and depth, determining the safety factor through a GIS-based time-series visualization of spatiotemporal safety factor variations. Chansorn et al. [66] used TOPMODEL to evaluate landslide occurrences in Thailand’s Huai Nam Phung Subbasin by examining temporal changes in groundwater levels and calculating slope stability safety factors. Their study found that landslide frequency increased in 2017 due to higher water volumes, affecting both steep and gentle slopes. Cui et al. [67] investigated the spatiotemporal variation of wetting front depth during rainfall events using the recursive first-order reliability method (FORM) in their PRL-STIM model, which accurately predicted rainfall-induced landslides in a representative area in China. He et al. [66] conducted a detailed simulation of runoff, infiltration, and slope instabilities in both wide and narrow areas of Hokkaido, Japan, using a model that combines surface flow, subsurface flow, and soil mechanics. This study emphasized the dynamic interaction between runoff and infiltration under heavy rainfall, highlighting the successful modeling of runoff generation and the effects of artificial structures, such as asphalt pavement, on runoff dynamics, as well as the impact of clogged ditches on slope failure.

While many studies have explored rainfall-induced landslides by estimating infiltration using equations or basic hydrological models, few have employed a comprehensive model that accounts for the entire hydrological cycle to achieve more accurate infiltration simulations. In this research, we used the Soil and Water Assessment Tool (SWAT) to simulate infiltration and runoff from rainfall throughout the Anacostia watershed in Maryland, US, considering the full hydrological cycle. We then developed a GIS-based model to map the Factor of Safety (FS) and evaluate landslide risk, integrating the infiltration data derived from SWAT. This methodology offers a more comprehensive and precise assessment of landslide risks linked to rainfall events.

5.3 Materials and Methods

5.3.1 Study Area

The study area is the Anacostia River watershed, located in Maryland near Washington, DC. This watershed feeds into the tidal portion of the Anacostia River, eventually joining the Potomac River segment of the Chesapeake Bay [68] (Figure 5.1). The Anacostia River watershed encompasses 13 subwatersheds, extending across the state of Maryland and Washington, DC, USA. Covering a total drainage area of 471 km2 (in Maryland), approximately 60% of the basin is classified as urban or suburban [69]. Within the tidal Anacostia River, water residence times fluctuate between 35 to 100 days, a variation influenced by the significant tidal volume to inflow ratio [70].

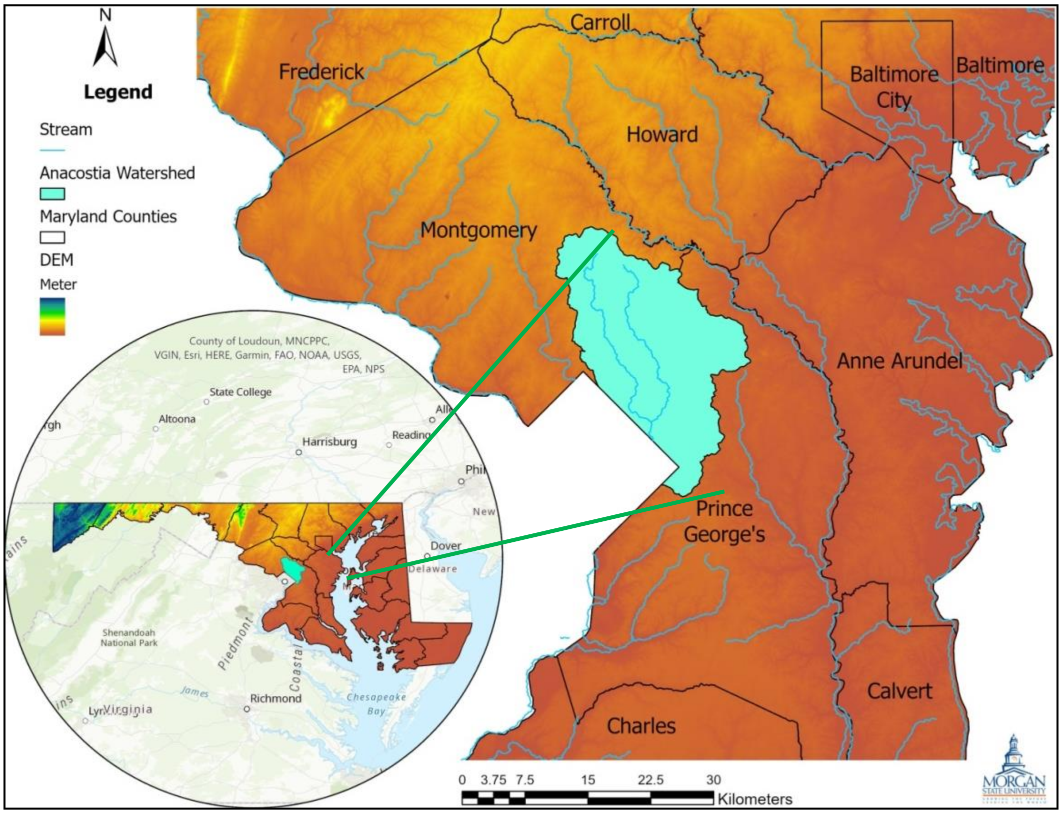

Figure 5.1: Location of the study area, Anacostia River watershed in Maryland.

The selection of this area for study is motivated by the historical prevalence of landslides in Maryland, particularly within the watershed. This decision is informed by the map created using landslide inventory location provided by MDOT SHA (Maryland Department of Transportation, State Highway Administration), highlighting the significance of the chosen watershed in understanding and addressing landslide occurrences (Figure 5.2).

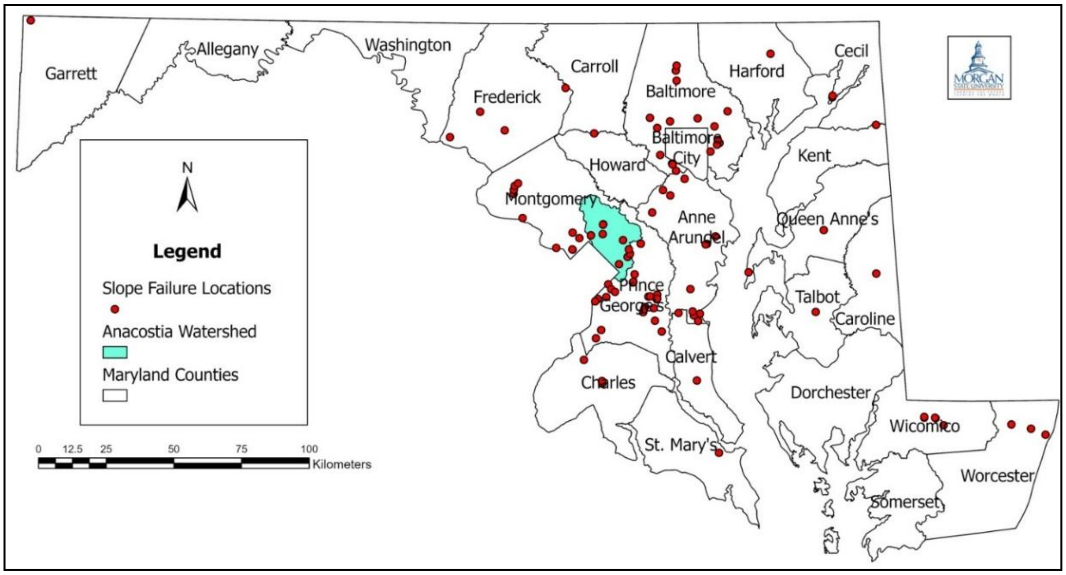

Figure 5.2: The historical landslides location in Maryland provided by SHA.

5.3.2 Data Preparation

5.3.2.1 Hydrological Model Data

The implementation of the SWAT+ model in our study involves a comprehensive data collection process, emphasizing detailed information on climate, soils, and land use specific to the chosen site. Flow rate data from USGS gauge stations in the Anacostia region is essential for model calibration. To establish a precise soil map, we rely on the Maryland Soil Survey Geographic Database (SSURGO). Topographical features are delineated using 1/3 arc-second Light Detection and Ranging (LiDAR)-based Digital Elevation Models for Maryland. Daily weather inputs for SWAT, encompassing precipitation, temperature, solar radiation, relative humidity, and wind speed, are derived from the NASA Power Larc Project for Takoma Park Station. This meticulous data integration ensures the accuracy and reliability of our SWAT model for simulating runoff and infiltration dynamics in the Anacostia watershed.

We obtained the land use map for Maryland from the Maryland Department of Planning (MDP). The MDP data, a GIS land use and land cover product, was initially created through aerial photographic interpretation, with subsequent updates using LANDSAT satellite imagery. Regular updates aim to enhance landscape characterization, with a significant improvement in 2010 involving the use of enhanced 2007 aerial imagery from the National Agriculture Imagery Program (NAIP) and the 2008 MDProperty View product.

The 2010 dataset's quality was notably enhanced, incorporating higher resolution imagery and additional parcel data. The introduction of new land use categories (Very Low Density Residential and Transportation) posed challenges in direct statistical comparisons across different timeframes. To address this, MDP integrated improvements into the 2002 land use dataset using GIS analysis tools, NAIP imagery, and MDProperty View data. This process included adding new categories, rectifying classification inconsistencies, and refining the mapping of agricultural and forest lands. The resulting GIS datasets for 2002 are available upon request but are not intended to replace the existing 2002 GIS files. After downloading shape file map of land use based on the map classification definition we added one column to this shape file to introduce the SWAT Code for land use (Table 5.1). Then we converted the shape file to the raster map to import to our SWAT model (Figure 5.3).

Table 5.1 SWAT code for land use map

LU - Code	SWAT Code	Description
11	URLD	Low-density residential
12	URMD	Medium-density residential
13	URHD	High-density residential
14	UCOM	Commercial
15	UIDU	Industrial
16	UINS	Institutional
17	OAK	Extractive
18	FESC	Open urban land
21	AGRL	Cropland
22	PAST	Pasture
25	AGRR	Row Crops
41	FRSD	Deciduous forest
42	FRSE	Evergreen forest
43	FRST	Mixed Forest
50	WATR	Water
60	WETL	Wetlands
73	SWRN	Bare ground
80	UTRN	Transportation

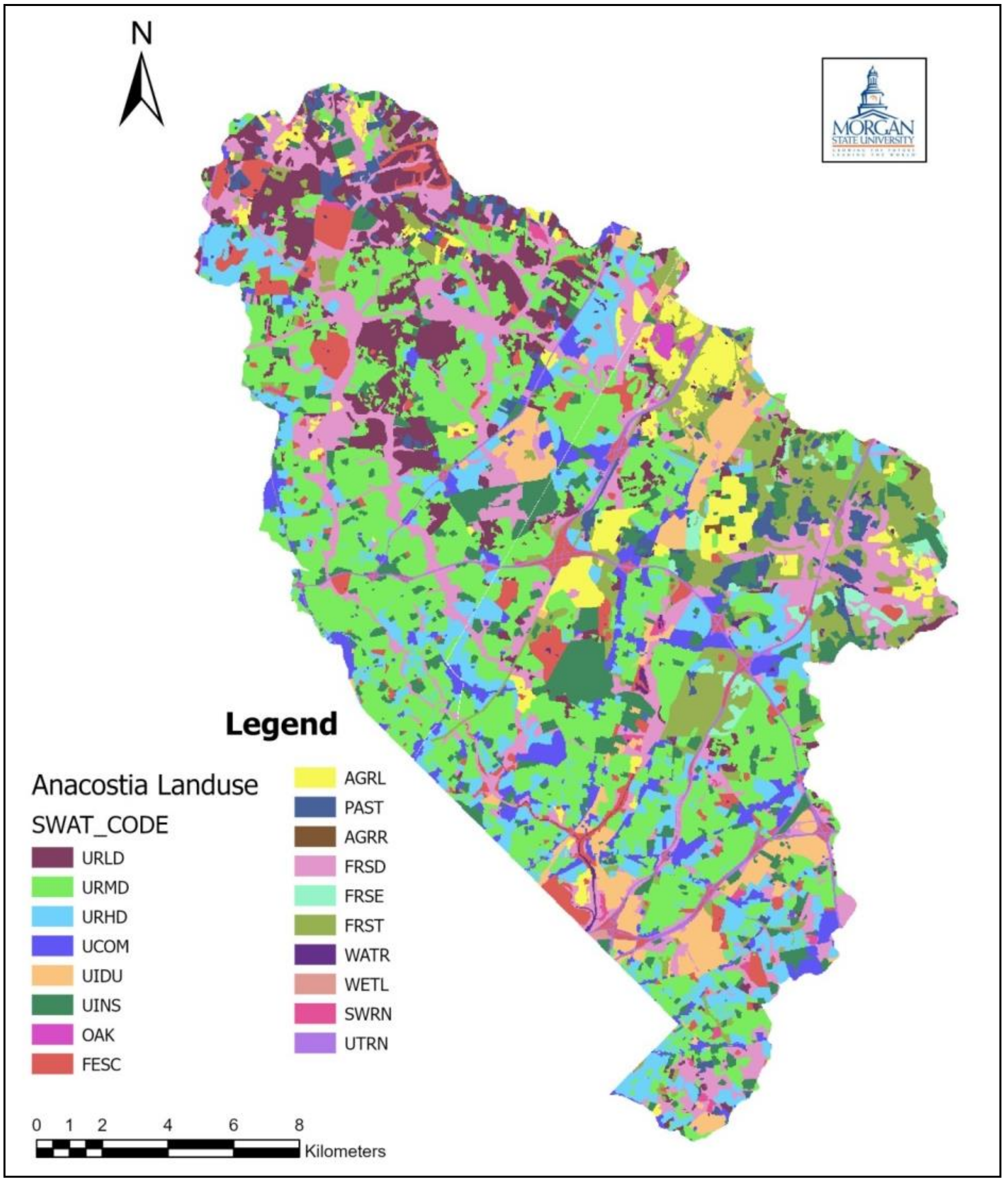

Figure 5.3: Landuse map of Anacostia.

5.3.2.2 Slope Stability and Landslide Risk Data

The key parameters essential for investigating slope instability include cohesion and the effective internal angle of friction, which are obtained from the soil map provided by SSURGO. Additionally, the slope angle, necessary for the analysis, can be derived from DEM maps using ArcPro (Figure 5.4).

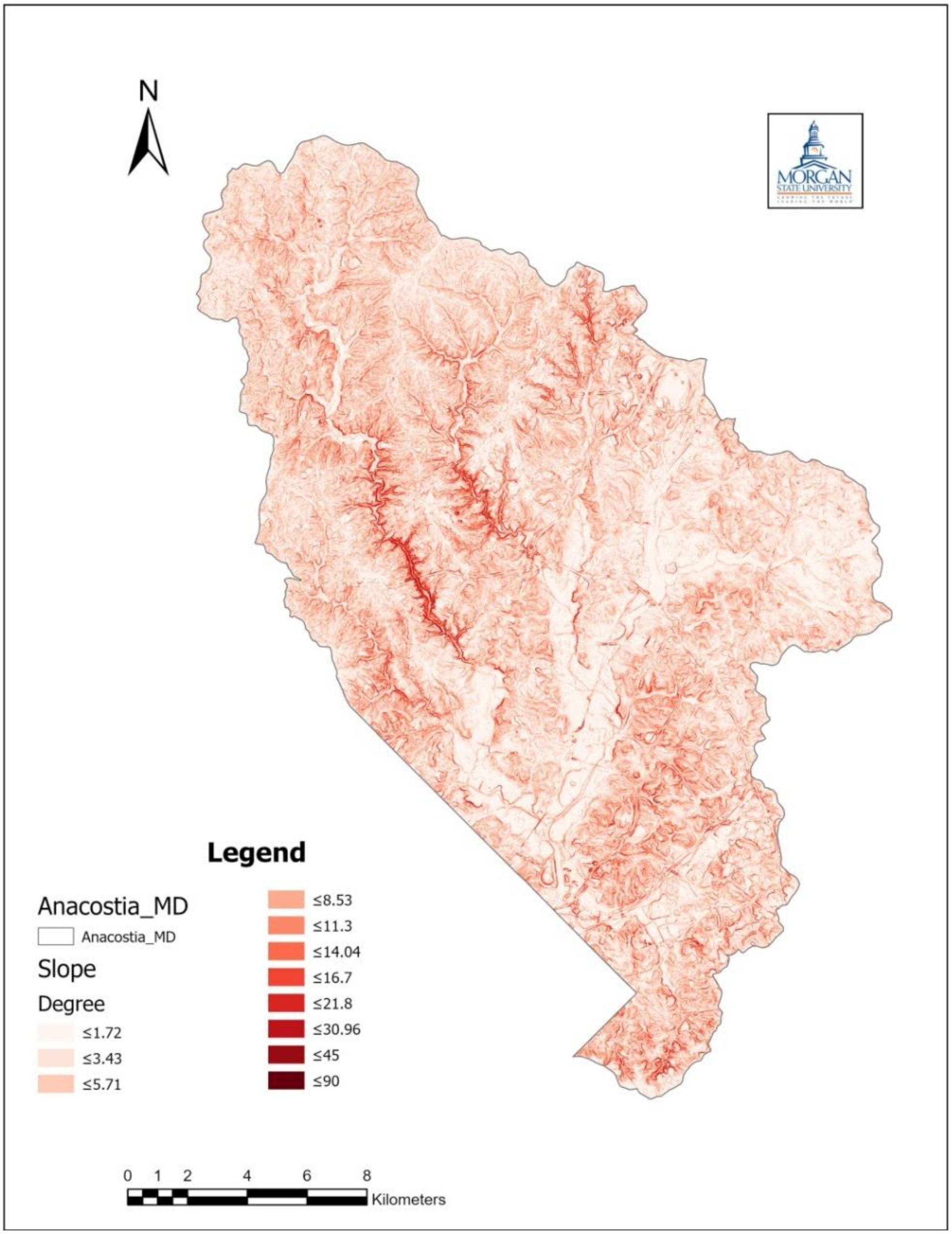

Figure 5.4: The slope map of Anacostia.

Another critical parameter is SG, representing the bulk specific gravity of the soil, calculated as the ratio of the unit weight of soil to the unit weight of water. SG estimation can also be based on soil type and the soil map. The soil type was missed for some parts of the soil map and we found the soil type of these parts by considering the percentage of clay, silt and sand and using USGS soil type calculator. To ensure comprehensive analysis, we compiled soil property data from various sources, including references such as [71], to create Table 2, which details soil properties for different soil types.

Table 5.2: Typical values of soil parameters for different soils according to USCS

Soil type	SG	C (KN/m^2)	Phi (°)	Field capacity	Porosity	Sgsat
Channery loam	2.66	0	30	0.28	0.48	2.86
Channery silt loam	2.66	0	27	0.29	0.51	2.88
Clay loam	2.69	10	18	0.32	0.46	2.83
Fine sandy loam	2.64	0	33	0.15	0.46	2.95
well-graded gravel, fine to coarse gravel	2	0	40	0.08	0.36	2.28
Gravelly loam	2	0	32	0.08	0.37	2.29
Gravelly sandy loam	2	0	36	0.07	0.35	2.28
Gravelly silt loam	2	0	30	0.09	0.38	2.29
Loam	2.66	0	28	0.27	0.47	2.86
Loamy sand	2.65	0	31	0.09	0.44	3
Moderately decomposed plant material	2.2	20	17	0.32	0.47	2.35
Sand	2.65	0	37	0.17	0.43	2.91
Sandy loam	2.65	0	32	0.14	0.45	2.96
Silt loam	2.67	0	25	0.28	0.5	2.89
Silty clay loam	2.69	10	18	0.33	0.48	2.84
Slightly decomposed plant material	2.2	20	17	0.32	0.47	2.35
Silt loam highway	2.67	0	30	0.28	0.5	2.89

5.3.3 Modeling with SWAT

SWAT is a tool designed to forecast how land management choices impact water quality, sediment, and agricultural chemical levels in diverse and complex watersheds over long periods. [72, 73]. This widely adopted model reflects long time of continuous development [74]. SWAT operates on the different physical principles of water and sediment flow, crop development, and nutrient cycling that can be used for long-term studies.

Its flexibility is underscored by its ability to address various water resource problems, a testament to the model's comprehensive nature, robust support, and the open-access status of its source code [75]. In comparison to other leading hydrologic and water quality models, SWAT has solidified its position as a preferred tool in the field [73]. In SWAT studies, the water balance is crucial. The model simulates two main phases: the land phase controls inputs to the main channel, and the water phase manages the movement through the watershed's channel network [76]. This equation is used in SWAT to simulate hydrological cycle:

$$SW_t = SW_0 + \sum_{i=1}^{t}(R_{day} - Q_{surf} - E_a - W_{seep} - Q_{gw}) \tag{5.1}$$

Where SW_t is the final soil water content (mm), SW_0 is the initial soil water content (mm), t is the time (day), R_{day} is the precipitation (mm), Q_{surf} is the surface runoff (mm), E_a is the evapotranspiration (mm), W_{seep} is the amount of water entering the vadose zone from the soil profile (mm), Q_{gw} and is the amount of return flow (mm). Estimating some components of this equation is explained in the following.

5.3.3.1 Surface Runoff

There are two methods to estimate surface runoff in SWAT: the SCS curve number method [77] and the Green-Ampt infiltration method [78]. The choice between the two methods hinges on the data time-steps. In this study, we chose the SCS method instead of the Green-Ampt method because the Green-Ampt method needs more time due to its requirement for sub-daily precipitation data [76, 53]. In the other hand, the SCS curve number (CN) method is a popular and versatile approach for computing runoff volume from rainfall and known for its simplicity and applicability [79]. It considers key watershed characteristics and has been successfully applied in diverse environments, from small agricultural watersheds to rural, forest, and urban settings [80]. The SCS-CN equation is [77]:

$$Q_{surf} = \frac{(R-0.2S)^2}{(R+0.8S)} \tag{5.2}$$

$$S = 25.4\left(\frac{1000}{CN} - 10\right) \tag{5.3}$$

where Q_{surf} is the amount of runoff, R is the amount of rainfall; and s is a retention parameter that depends on soils, land use, management, slope, and soil water content and is related to the CN by the equation (3).

5.3.3.2 Evapotranspiration

In this study we used Penman-Monteith method to estimate potential evapotranspiration. This method has been widely employed to analyze experimental results [81]. It tackles surface energy balance and the movement of heat and water vapor all at once and takes some shortcuts in the math to make a clear equation (Eq. 5.4). This method requires solar radiation, air temperature, relative humidity, and wind speed [82].

$$\lambda E = \frac{\Delta.(R_n-G)+\rho * c_p * [e_z^0-e_z]/r_a}{\Delta+\gamma *(1+\frac{r_c}{r_a})} \tag{5.4}$$

Where λE is the evaporative latent heat flux (MJ m^{-2} d^{-1}), Δ is the slope of the saturation vapor pressure-temperature curve (kPa/C°), R_n is the net radiation (MJ m^{-2} d^{-1}), G is the heat flux density to the ground (MJ m^{-2} d^{-1}), ρ is the air density (kg/m^3), c_p is the specific heat at constant pressure (MJ/kgC°), e_z^0 is the saturation vapor pressure of air at height z (kPa), e_z is the water vapor pressure of air at height z (kPa), γ is the psychrometric constant (kPa/C°), r_c is the plant canopy resistance (s/m), r_a and is the diffusion resistance of the air layer (s/m).

5.3.3.3 Calibration and Model Performance Evaluation of SWAT

Calibration is traditionally manual, requiring adjustments to model input parameters for simulated values to align with measured data; however, for complex hydrologic models, the time-consuming nature of manual calibration has prompted a preference for automated calibration methods [83]. Calibrating SWAT involves numerous parameters, adding complexity; to streamline the process, we selectively focus on key parameters identified in prior research [53, 83, 84] for a more targeted sensitivity analysis. In this research, we utilized SWATplus Toolbox to auto-calibration model and the daily stream flow data from a gauge station on the Anacostia River called North West branch of Anacostia, located at Latitude 38°57'09.2" and Longitude 76°57'54.5" (NAD83) for the period between 2015 and 2022 as our observation data to calibrate the SWAT model.

There are several methods for model evaluation that Moriasi et al. [85] recommended. Some of them that work well in different situations, are commonly used and accepted in published work, and have proven strengths in evaluating models. In this research we used three most recommended statistical model evaluation methods, Nash-Sutcliffe efficiency (NSE), RMSE-Observations Standard Deviation Ratio (RSR) and Pbias Percent Bias (PBIAS).

The Nash-Sutcliffe efficiency (NSE) is a key statistic that tells us how much the difference between predicted and observed data compares to the variance in the measured data [85].

$$NS = 1 - \frac{\sum(Q_{obs}-Q_S)^2}{\sum(Q_{obs}-\bar{Q}_{obs})^2} \qquad (5.5)$$

where $\bar{Q}_{obs}$ is the mean of observed discharges, and Q_s is simulated discharge and Q_{obs} is observed discharge.

The RMSE-Observations Standard Deviation Ratio (RSR), is a model evaluation metric introduced by Singh et al. [86]. It standardizes RMSE by considering the variability in the observed data. A lower RSR generally indicates better model performance, highlighting a smaller model error relative to the variability in the measured data.

$$RSR = \frac{RMSE}{\bar{\sigma}} = \frac{\sqrt{\sum(Q_{obs}-Q_S)^2}}{\sqrt{\sum(Q_{obs}-\bar{Q}_{obs})^2}} \qquad (5.6)$$

Pbias Percent Bias (PBIAS), is a metric that assesses the average tendency of simulated data to be larger or smaller than the observed data. This concept was introduced by Gupta et al. [87] in 1999. An optimal PBIAS value is 0.0, which indicates an accurate model simulation. Positive PBIAS values suggest that the model underestimates, while negative values indicate overestimation. The PBIAS is calculated using Equation (5.7).

$$P_{Bias} = \frac{(Q_{obs} - Q_s)*100}{Q_{obs}} \qquad (5.7)$$

5.3.4 Slope Stability Physical Model

Applying the theory of infinite slope stability allows the identification of circumstances in which a soil layer with a thickness denoted as Z may experience sliding over a plane parallel to the surface, characterized by a slope angle of θ concerning the horizon. The criteria for sliding conditions are ascertainable through the application of Coulomb's law of friction. If seepage is presumed to be parallel to the plane of failure, the factor of safety (FS) concerning slope failure along a given plane can be computed utilizing the equation (5.8).

$$FS = \frac{C+\left[\frac{(\gamma_{sat}-\gamma_{w})h}{cos^2\theta}+\gamma\left(Z-\frac{h}{cos^2\theta}\right)\right]cos^2\theta.tan\varphi}{\left[\frac{(\gamma_{sat})h}{cos^2\theta}+\gamma\left(Z-\frac{h}{cos^2\theta}\right)\right] sin\theta.cos\theta} \tag{5.8}$$

Where C is the apparent cohesion, γ_{sat} is the specific weight of saturated soil, γ_w is the specific weight of water, $\frac{h}{cos^2\theta}$ is the depth of seepage and h is the water pressure associated with the seepage depth, γ is the unit weight of soil under normal conditions, θ is the slope angle, and φ is the effective internal angle of friction.

A factor of safety below 1 indicates slope failure. Specifically, if the numerator of Equation (5.8) is less than its denominator, the soil layer with a thickness of Z will experience slipping over the plane of failure. By expressing Equation (5.8) as an inequality that signifies a condition where the factor of safety is less than 1, it can be reorganized to establish the minimum depth of seepage in the soil layer essential to trigger slope failure. Consequently, one can ascertain the minimum seepage depth (Hcr) required for inducing slope failure:

$$H_{cr} = \frac{\frac{C}{\gamma_w}-SG.Z.cos^2\theta(tan\theta-tan\varphi)}{cos^2\theta[(SG_{sat}-SG)(tan\theta-tan\varphi)+tan\varphi]} \tag{5.9}$$

Where H_{cr} is the critical seepage depth for the soil layer; SG is the bulk specific gravity of the soil, which is the ratio of the unit weight of soil to the unit weight of water; and SG_{sat} is the specific gravity of saturated soil.

Finally, with an initial moisture content at field capacity, ϑ_{FC}, and porosity (η), the minimum amount of infiltrating water (F) that will cause failure becomes:

$$F = H_{cr}cos^2\theta(\eta - \vartheta_{FC}) \tag{5.10}$$

To determine Z, one effective method is to use the Topographic Wetness Index (TWI), which reflects moisture levels influenced by topography and is derived from topographic attributes [88]. TWI is calculated using Digital Elevation Models (DEM), as described in Equation (5.7) [86].

$$TWI = ln\frac{\alpha}{\tan\beta} \tag{5.11}$$

where α represents the flow accumulation and β is the slope angle in radians. Using a DEM and ArcGIS tools, we can generate a flow direction map, and subsequently, a TWI map (Fig. 5). Numerous studies have confirmed a linear relationship between soil thickness and TWI [89, 90, 91]. This study leverages this relationship to create soil thickness maps for the Anacostia watershed. Soil thickness data was collected from 9 locations using the Geosetta database. The observed soil thicknesses and TWI were used to generate a linear equation:

$$TWI = a + b(Z) \tag{5.12}$$

Based on Figure 6, the equation is $Z = \frac{TWI - 1.804}{0.3258}$. Using this equation, we generated a soil thickness map for the area.

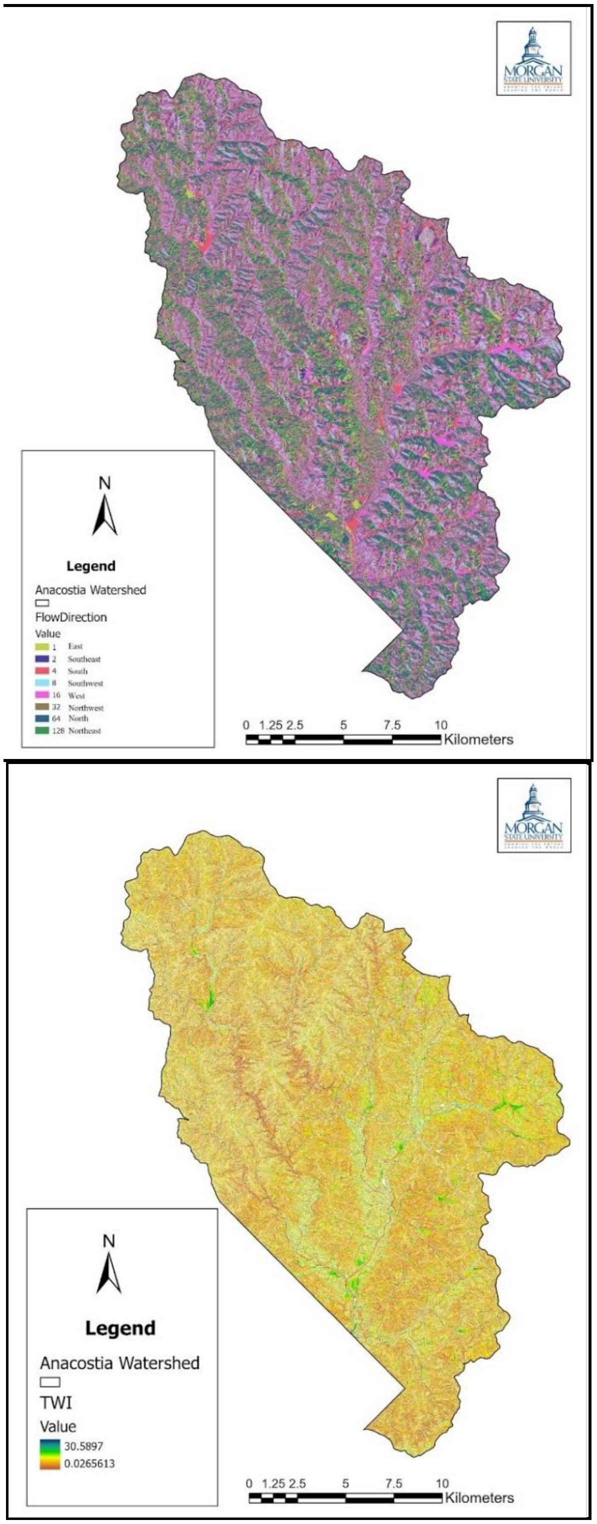

Figure 5.5: The maps of flow direction and TWI of Anacostia calculated by ArcGIS.

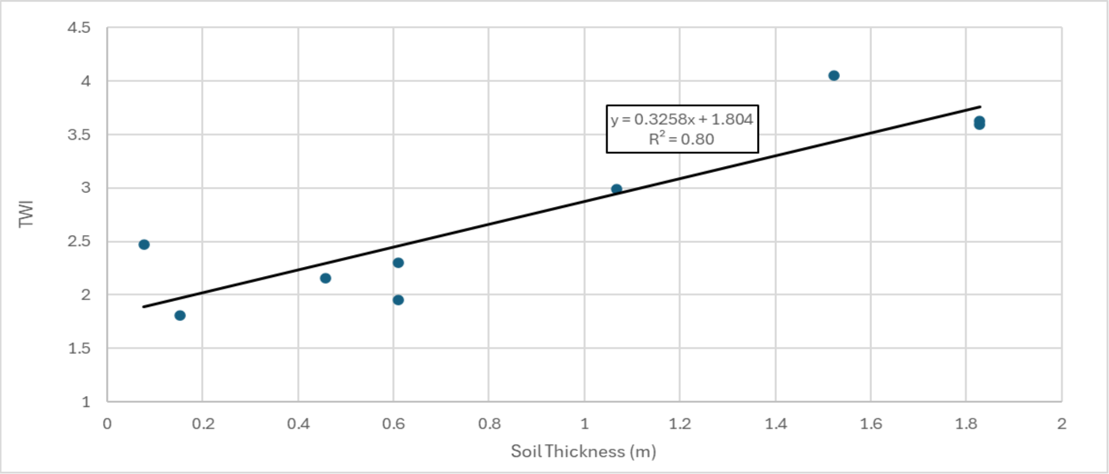

Figure 5.6: The linear relationship between TWI and observed slope thicknesses (Z).

5.4 Results

5.4.1 Hydrological Model

5.4.1.1 Sensitivity Analysis

Certain parameters like GW_DELAY and REVAPMN, recommended in prior studies [53], had minimal impact on simulated streamflow and were excluded from calibration. Sensitivity analysis identified SURLAG and CN2 as the most influential, with Epco being the least sensitive, as shown in Table 5.3.

Table 5.3: The results of sensitivity analysis of SWAT model

Parameter name	Description	Order sensitivity
SURLAG	Surface runoff lag coefficient	1.95
AWC	Available water capacity of the soil layer	0.02
CN2	Curve number for moisture condition II	-0.002
Alpha	Baseflow alpha factor	-0.0065
Esco	Soil evaporation compensation factor	-0.008
Epco	Plant uptake compensation factor	-0.0005
REVAPMN	Threshold water in shallow aquifer	0

5.4.1.2 Model Calibration

Based on sensitivity analysis we chose the most important parameters to calibrate model. Table 5.4 lists the parameters selected for model calibration for the period from 2015 to 2020.

Table 5.4: The value of calibrated SWAT parameters

Parameter name	Description	Initial range	Final value after calibration
CN2	Curve number for moisture condition II	(-0.2) - 0.2	0.02
AWC	Available water capacity of the soil layer	0.01 – 1	0.85
Esco	Soil evaporation compensation factor	0.1 – 1	0.137
Alpha	Baseflow alpha factor	0.01 – 1	0.191
SURLAG	Surface runoff lag coefficient	0.05 – 24	6.146

Figures 5.7 and 5.8 illustrate the simulated versus observed streamflow for our gauge station located on channel 8 on the main outlet of the SWAT model over various years between 2015 and 2020 for calibration period and year 2021-2022 for validation period. The years 2015 and 2016 were utilized as a warm-up period for the SWAT model. The results demonstrate a close alignment between simulated and observed flow rates.

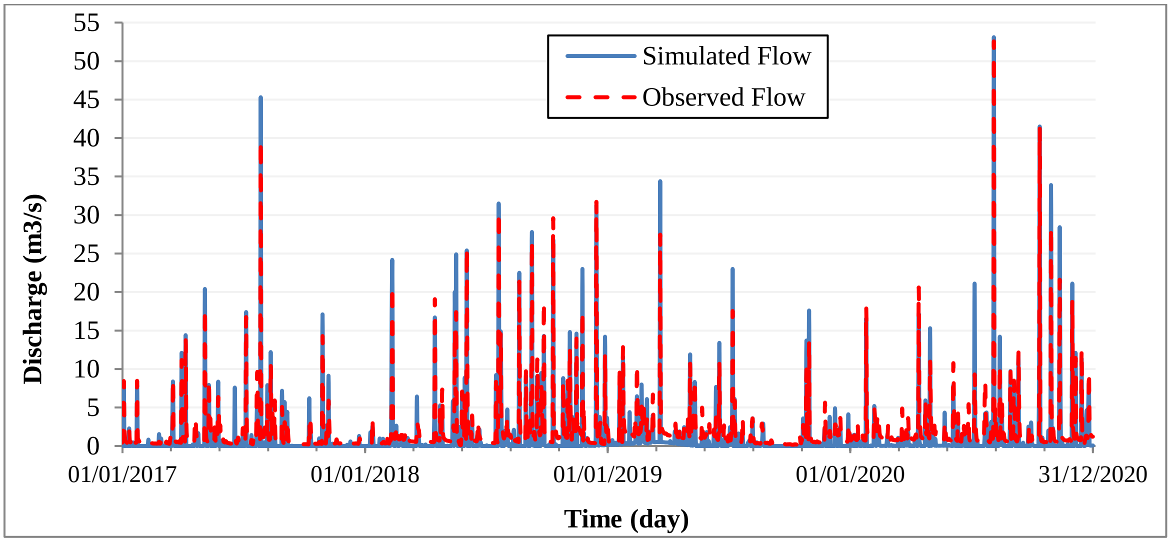

Figure 5.7: Simulated and observed stream flow at gauging station North West branch of Anacostia after calibration.

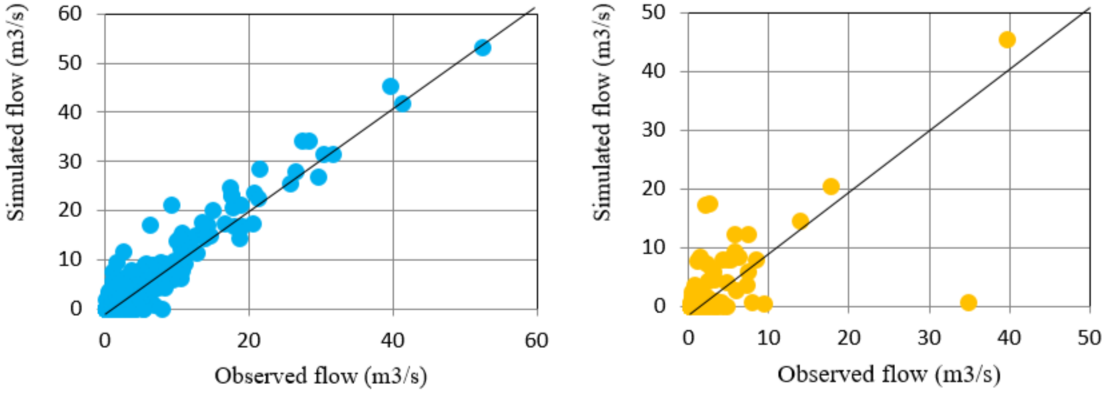

Figure 5.8: Simulated flow versus observed flow at gauging station North West branch of Anacostia for calibration (left graph) and validation (right graph).

For model evaluation, we calculated a NSE of 0.85 and P_{bias} of 12%, indicating very good and good performance according to Table 5.5 [92]. Additionally, our calibrated model has an RMSE of 1.43 m^3/s and a standard deviation of observed flow rate data of 3.44 m^3/s, resulting in an RSR of 0.41, which indicates very good model performance [83].

Table 5.5: General performance ratings for NSE and RSR for a daily time step

P_{bias}	NSE	RSR	Model Performance
0-10	0.75 - 1	0 – 0.5	Very good
10-15	0.65 – 0.75	0.5 – 0.6	Good
15-20	0.5 – 0.65	0.6 – 0.7	Fair
>20	≤ 0.5	≥ 0.7	Inadequate

For the validation period (2021 and 2022), the NSE and RSR were estimated at 0.68 and 0.52, respectively, signifying good model performance. Figure 9 visually compares observed precipitation data with the simulated streamflow rates. The alignment of peak flow rates with increasing precipitation levels highlights the model's capacity to accurately capture the dynamics of streamflow in response to varying precipitation.

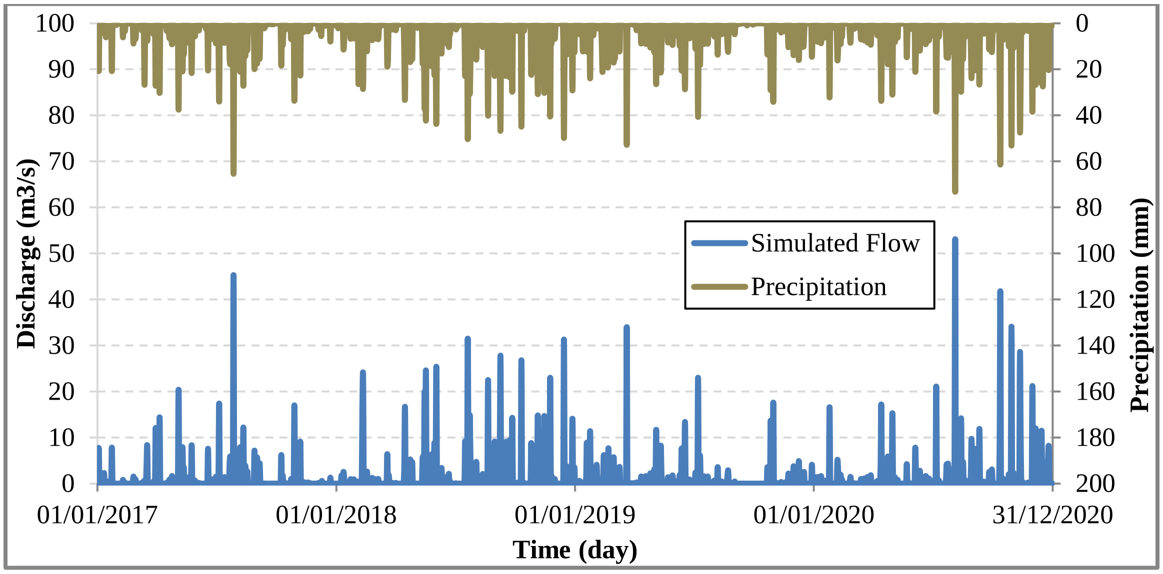

Figure 5.9: Simulated flow rate and observed precipitation at station of North West branch of Anacostia River.

5.4.1.3 Simulated Results

Figure 5.10 illustrates the model's proficiency in quantifying both surface runoff and infiltration resulting from rainfall. This capability allows the model to accurately calculate and distinguish the volumes of surface runoff and infiltration, ensuring a precise assessment of hydrological processes. The model's commendable performance in these simulations confirms the reliability of the derived results, making it a robust tool for hydrological analysis and prediction.

Figure 5.11 presents a map of the average soil moisture content due to rainfall in the Anacostia watershed for the year 2018. This map demonstrates the ability to spatially simulate infiltration for each rainfall event. By understanding the infiltration levels across different areas of the watershed, this information can be utilized to create a landslide risk map, helping to assess the potential for landslides in each specific part of the study area.

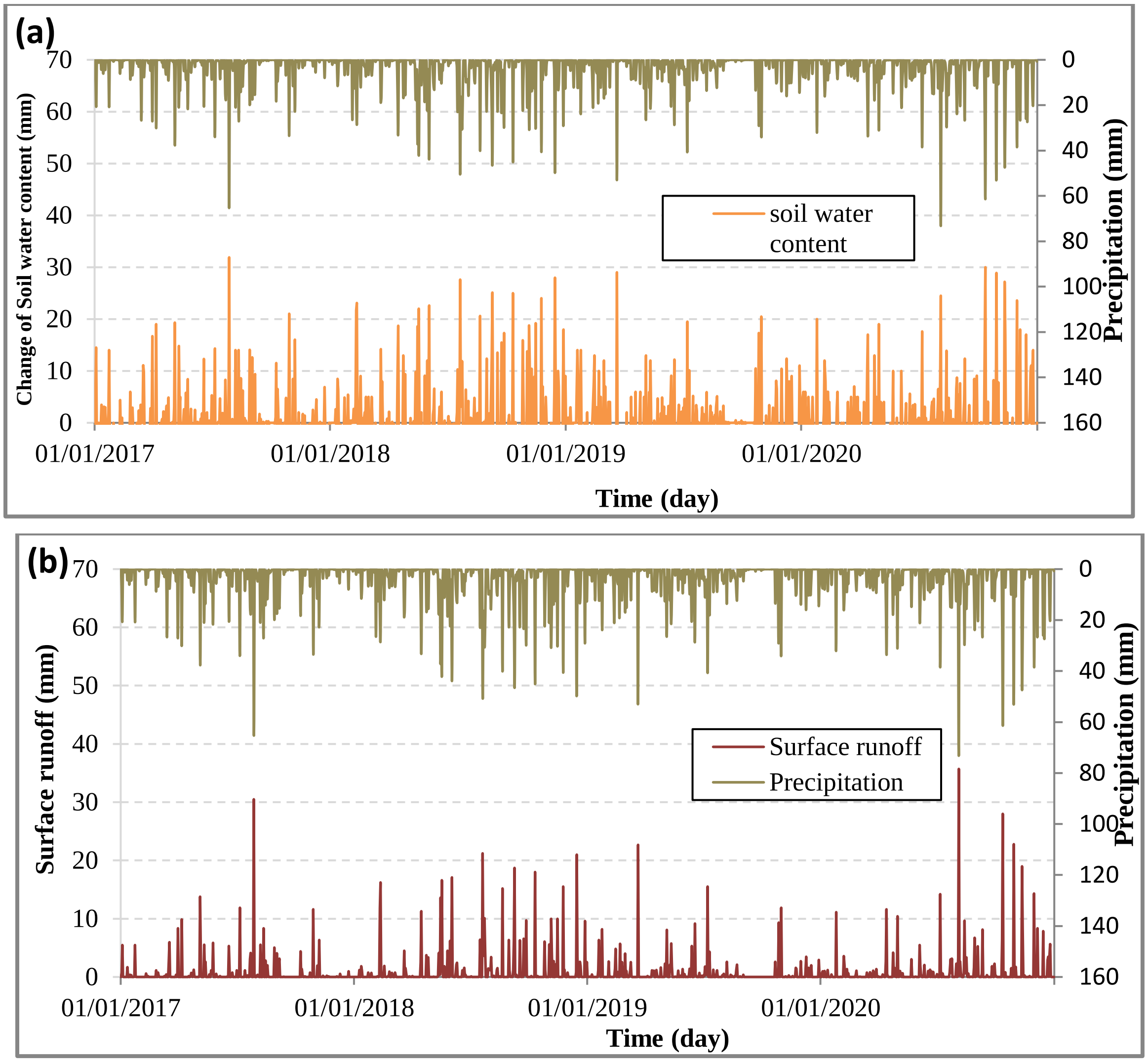

Figure 5.10. The amount of infiltration (a) and surface flow rate (b) at station of North West branch of Anacostia River.

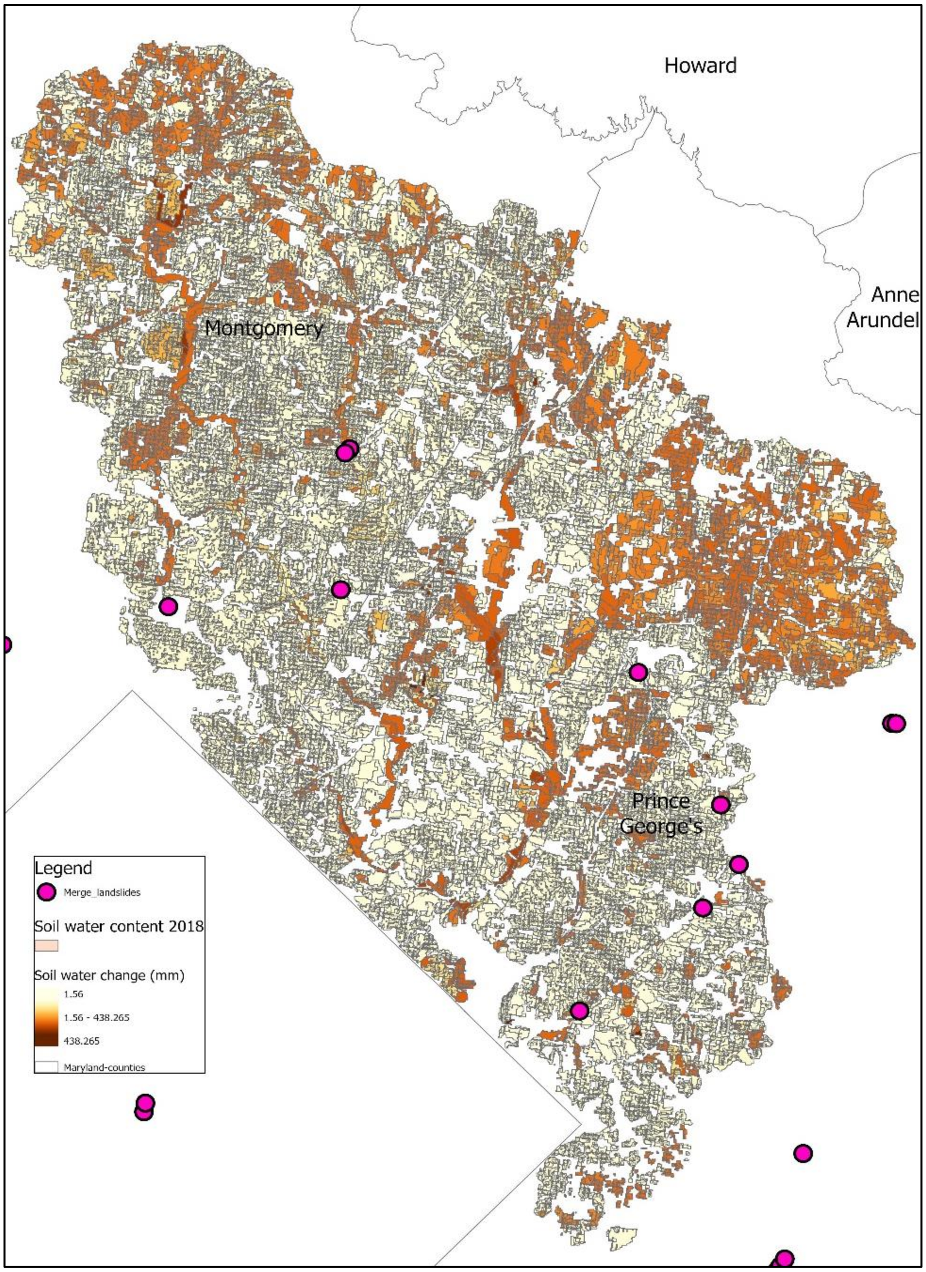

Figure 5.11: The map of the amount of average soil water content in Anacostia watershed in 2018 simulated by SWAT model.

5.4.2 Landslide Risk Model

5.4.2.1 Sensitivity Analysis

Following initial modeling and testing, sensitivity analysis was conducted, resulting in Table 5.6. Each parameter was increased by 20%, and the corresponding change in critical seepage depth for the soil layer was calculated. Table 5.2 highlights the significance of SG, or bulk specific gravity of the soil, as the most influential parameter in the model. A 20% increase in SG corresponds to a 25% increase in the critical seepage depth.

Table 5.6: Sensitivity analysis results

Variable	Change in mean of Hcr (%)
Slope angle (θ)	-4.4%
Internal angle of friction (Φ)	3.0%
Cohesion (c)	1.4%
Bulk specific gravity (SG)	25.3%

5.4.2.2 Simulated Results

Utilizing the collected data and values, we generated raster maps using ArcGIS, incorporating the "raster calculator" tool and equations (5.9) and (5.10). This process for the first scenario resulted in the creation of a map depicting the minimum amount of infiltrating water (F) in centimeter necessary to induce failure for slope thickness of 1 meter, as illustrated in Figure 5.12.

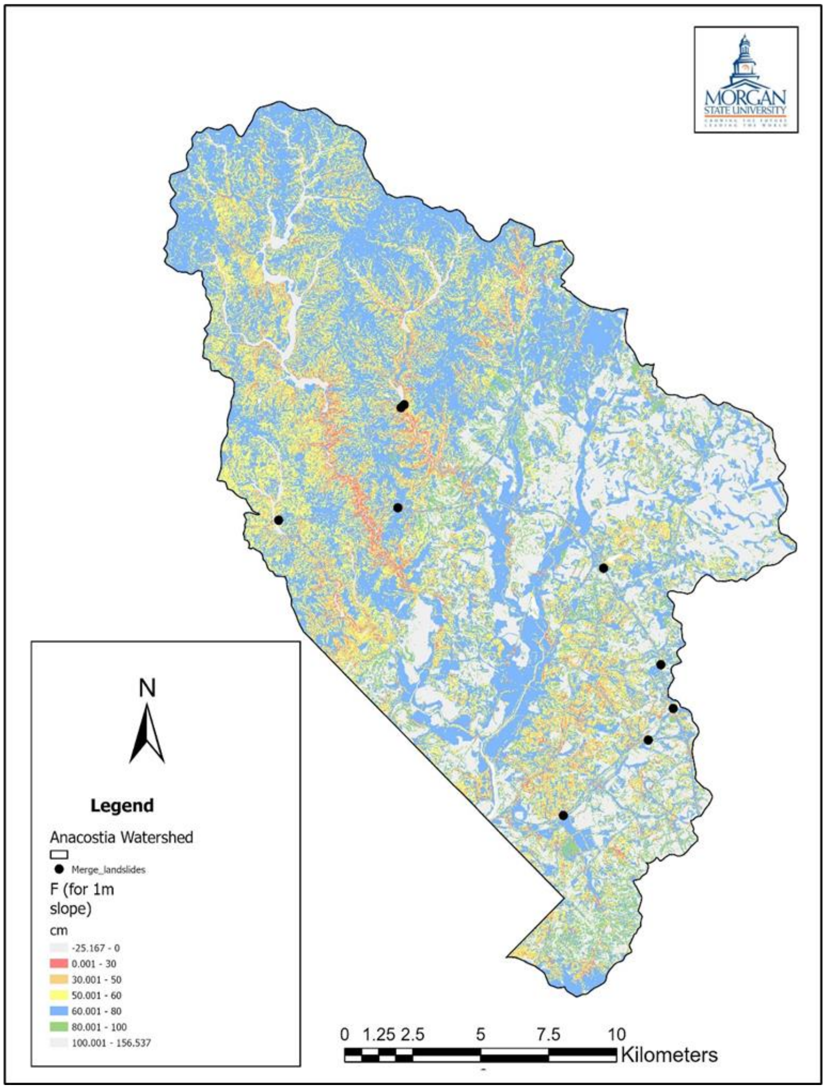

Figure 5.12: The map of minimum amount of infiltrating water (F) that will cause failure becomes with assuming slope thickness of 1 meter.

According to Figure 5.12, the red areas on the map indicate regions with a lower threshold for infiltration, indicating a higher risk of landslide occurrence. Conversely, the black dots represent historical landslide locations, with many occurring in the red and orange regions, signifying elevated landslide risk. This suggests that the initial landslide modeling, incorporating physical processes, is effective.

The LiDAR data, acquired from USGS has been overlaid with the output map depicting landslide risk that displayed in Figure 5.13. However, it's important to note that the LiDAR data is available only for the southern part of the study area, specifically Prince's George County. Despite this limitation, observations reveal that certain areas adjacent to historical landslide sites persist within high-risk zones as indicated by the landslide model.

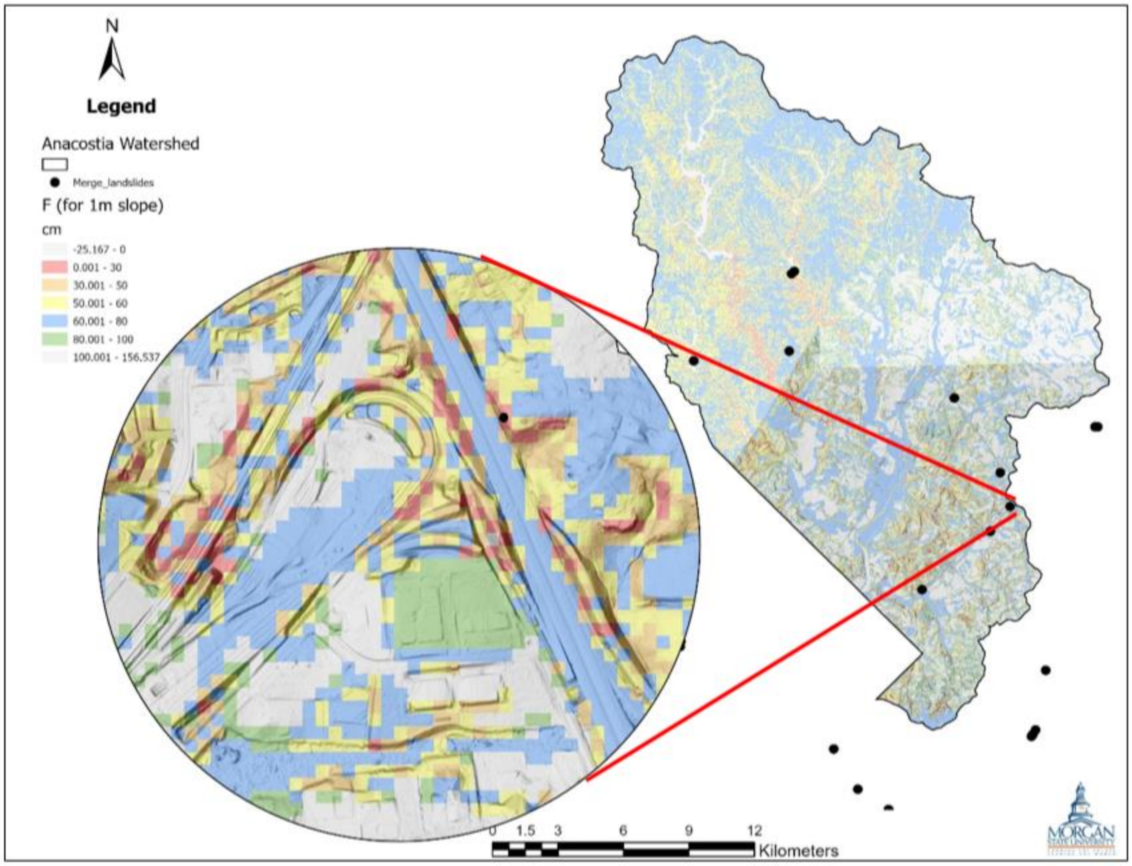

Figure 5.13: The map of landslide risk with assuming slope thickness of 1 meter overlaying with LiDAR data.

We prepared a map for site visits based on historical landslide locations and the results of a GIS-based slope instability model to collect samples and measure slope dimensions. Figure 5.14 displays detailed zoom-in views of each site. Notably, some of these sites remain within the red areas, indicating a high risk of slope failure.

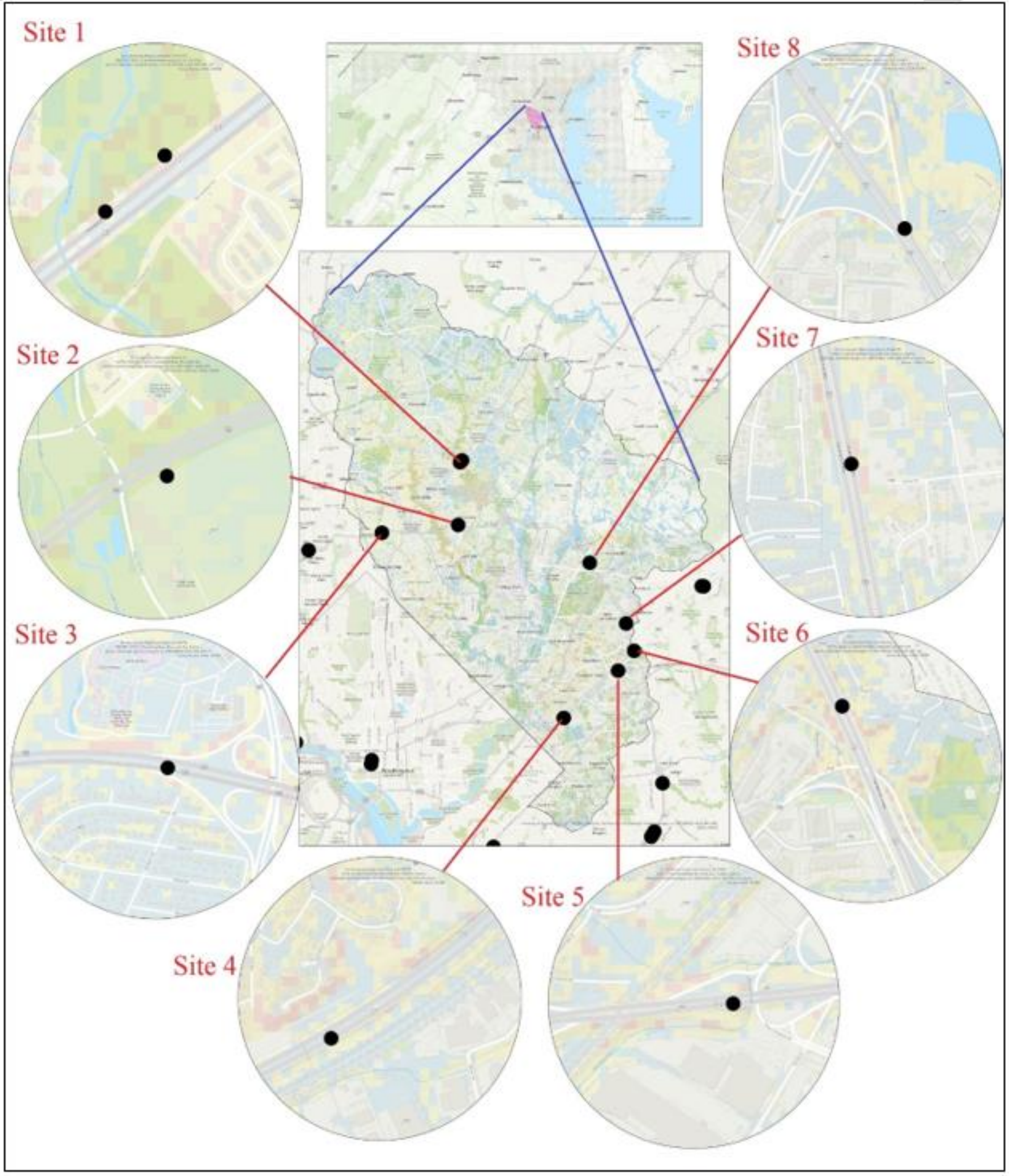

Figure 5.14: The map of site visiting location determine based on historical landslides and the results of GIS-based slope stability model.

In the second scenario, we utilized the slope thickness map derived from the TWI method instead of employing a constant soil thickness value to calculate the F_{min} map. Figure 5.15 illustrates the landslide risk map generated using this slope thickness map. This approach allows for a more accurate and detailed assessment of landslide risk by incorporating variable soil thicknesses across the study area. In this map, we observe that the red areas, indicating higher landslide risk, are relatively fewer and are primarily located near roads.

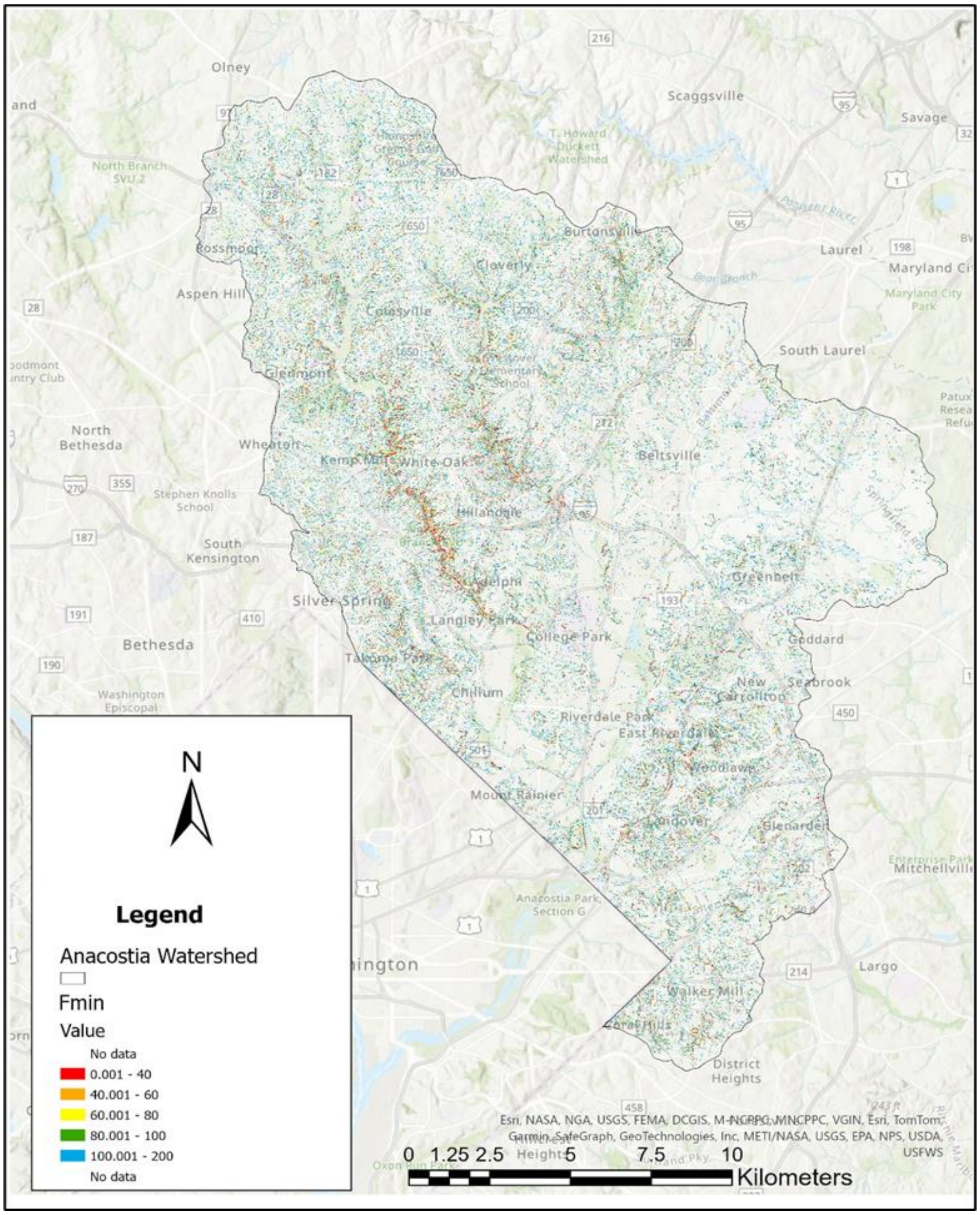

Esri, NASA, NGA, USGS, FEMA, DCGIS, M-NCPPC, VGIN, Esri, TomTom, Garmin, SafeGraph, GeoTechnologies, Inc, METI/NASA, USGS, EPA, NPS, USDA, USFWS

Figure 5.15: The map of minimum amount of infiltrating water (F) that will cause failure with considering slope thickness map derived from the TWI method.

In this map, we calculated only the amount of infiltration required to trigger slope failure. To create a comprehensive landslide risk map, we need to integrate these results with the outputs from the hydrological model. Additionally, we should account for cumulative infiltration from multiple rainfall events, rather than considering a single event.

5.5 Conclusion and Future Works

In conclusion, this study underscores the critical need for accurately assessing rainfall-induced landslides. The complex interplay between infiltration and runoff, especially in regions experiencing intense precipitation events exacerbated by climate change, necessitates precise modeling for effective risk assessment and mitigation. Traditional methods often oversimplify infiltration estimation, leading to inaccuracies in landslide risk prediction. To address this, we employed the SWAT model to simulate the entire hydrological cycle, focusing on the Anacostia River watershed in Maryland. By integrating SWAT outputs with a GIS-based slope stability model, we achieved a more comprehensive evaluation of landslide risks associated with rainfall events.

Our findings highlight the significance of detailed hydrological modeling in understanding the dynamics of slope stability. The SWAT model's ability to simulate both surface and subsurface flow, combined with precise land use, soil, and topographical data, allowed for a robust analysis of infiltration and runoff. The subsequent mapping of the Factor of Safety (FS) provided a nuanced understanding of landslide susceptibility across the watershed. The calibration and validation of the SWAT model, using streamflow data from the USGS gauge station, demonstrated high model performance, reinforcing the reliability of our approach. The integration of detailed soil parameters and slope stability analysis further enhanced the model's predictive capability.

In general, this study advances the methodology for assessing landslide risks by incorporating comprehensive hydrological simulations. The results emphasize the importance of accurate infiltration modeling in predicting rainfall-induced slope failures. Future research should continue to refine these models and explore their application in other regions to enhance early warning systems and inform land use planning, ultimately contributing to safer and more resilient communities.

In future work, we plan to further develop our hydrological and landslide models. First, we will calibrate the hydrological model using data from three flow rate gage stations. Using the calibrated SWAT model, we will determine the cumulative infiltration for different durations, including 3-day, 7-day, 15-day, and monthly intervals. Additionally, we will calculate the depth of groundwater (h) to incorporate into the Factor of Safety (Fs) equation. For the landslide model, we will utilize the simulated groundwater depth from the SWAT model to calculate the Factor of Safety (Fs) map, thereby enhancing the accuracy of landslide risk assessments.

Chapter 6

6. Physical Model Development – Literature Review

Samuel Fadipe, Sunil Lamsal, Yi Liu, Zhuping Sheng, Oludare Owolabi

6.1 Introduction

6.1.1 Background

Landslides have disrupted highways and roads across Maryland, presenting considerable risks to infrastructure and natural resources, impacting transportation safety and posing risks to property and lives. To address these challenges, a comprehensive understanding of slope failure mechanisms is critical for developing effective mitigation measures to prevent and minimize landslide damage.

Our research employs an innovative approach that integrates geomechanical model simulations with field investigations. We use the advanced modeling tools, TRIGRS (Transient Rainfall Infiltration and Grid-Based Regional Slope-Stability Model) and PLAXIS (officially called PLAXIS Geotechnical Analysis Software), to enhance our understanding of landslide dynamics.

In landslide-prone areas, field investigations involve extensive land slope measurements, identification of slope types and landsliding signs as well as causes of slope, soil sampling, accessibility for monitoring and further investigations, and slope engineering status, among others. Geotechnical laboratory testing, geological mapping, soil sampling, and geological profiling are conducted in the office. These methods provide essential practical and empirical data on environmental and climate triggers and the geographic distribution of historical events. This data is used to create detailed geomechanical models with TRIGRS and PLAXIS, which simulate landslide mechanisms across various geological and environmental contexts. Our study identifies critical factors influencing landslide susceptibility, such as geological structure and the physical and mechanical properties of soil. By validating these models against observed events and performing sensitivity analyses, we advance hazard assessment frameworks in landslide-prone regions, improve forecasting capabilities, and guide targeted mitigation strategies.
Future research should focus on incorporating real-time environmental data and further enhancing the complexity of these models to improve hazard prediction and management.

6.1.2 Purpose of Study

The purpose of this study is to identify and characterize landslide-prone areas in Maryland through field investigations. It aims to analyze the data collected from these geotechnical investigations and use geomechanical models, specifically TRIGRS and PLAXIS, to simulate landslide behavior under various conditions.

Based on the results of field observations and model simulations, the study seeks to develop and recommend effective mitigation measures.

6.2 Objectives

The primary objectives of this study are:

1. To conduct field investigations to identify landslide-prone areas in Maryland.
2. To collect and analyze geotechnical data from these sites.
3. To perform geotechnical laboratory testing of collected samples and obtain laboratory results.
4. To simulate landslide behavior using TRIGRS and PLAXIS models under various conditions with field and laboratory data.
5. To propose effective mitigation measures based on the simulation results and field data.

6.3 Literature Review

6.3.1 Overview

Relevant literature was reviewed to fully understand the features of the geomechanical models and their applications:

The TRIGRS model developed by Baum et al. [93], has been widely used for predicting rainfall-induced landslides. TRIGRS integrates transient rainfall infiltration with slope stability analysis, using a grid-based approach to simulate how rainfall affects soil moisture and slope stability over time. Valuable insights into the spatiotemporal distribution of landslide risk were provided by this model. The report demonstrates that applying TRIGRS to reliable geotechnical slope models significantly enhances landslide susceptibility analysis. By integrating detailed soil properties with transient rainfall simulations, this approach provides a more accurate and comprehensive assessment of landslide risk. The integration of TRIGRS with geotechnical models represents a valuable advancement in landslide prediction, offering improved accuracy and insights into the temporal dynamics of slope stability.

Iverson [94] investigated the mechanisms by which rainfall infiltration triggers landslides, focusing on the physical processes that lead to slope instability. The study emphasized the role of pore water pressure in reducing soil shear strength and highlighted the importance of understanding the hydrological and mechanical interactions within slope materials. Iverson used mathematical modeling to demonstrate how different rainfall patterns and soil properties affected the timing and location of landslide initiation. The research provided critical insights into predicting landslide occurrences by linking rainfall infiltration with slope failure mechanisms, offering valuable guidance for improving landslide hazard assessment and mitigation strategies.

Jibson [95] conducted a comprehensive analysis of landslide hazards in La Conchita, California. This region has faced and is expected to continue to face a diverse array of landslide hazards. The study investigated a reoccurring landslide in 2005 and compared it with a previous occurrence in the same location in 1995. It presented the geotechnical and hydrological factors contributing to slope instability in the region. It included an examination of historical landslide events, geological conditions, and the role of rainfall in triggering landslides. The report underscores the importance of thorough hazard assessments and effective mitigation strategies to address and minimize landslide risks in susceptible areas.

Godt et al. [96] applied the TRIGRS model to assess landslide susceptibility in the San Francisco Bay Area. The study aimed to evaluate the effectiveness of TRIGRS in predicting rainfall-induced landslides by incorporating local geotechnical and hydrological data. The authors calibrated the model using historical landslide data and rainfall records, demonstrating its ability to simulate pore pressure changes and slope stability under different rainfall scenarios. The results indicated that TRIGRS could reliably identify areas at high risk of landslides, providing valuable information for hazard mitigation and land-use planning in the region.

Several hybrids of TRIGRS with other models have been developed over the years for more accurate predictions of landslides susceptibility. Ciurleo et al. [97] demonstrated that applying TRIGRS to reliable geotechnical slope models significantly enhances landslide susceptibility analysis. The study showed that this integrated approach improves the accuracy of predictions, provides detailed risk mapping, and offers valuable temporal insights into slope stability. These results underline the effectiveness of combining advanced modeling techniques with high-quality geotechnical data to achieve more accurate and actionable landslide risk assessments.

Zhang et al. [98] demonstrate that soil mechanical and hydraulic parameters have a significant impact on the definition of rainfall intensity and duration thresholds using the TRIGRS model. Their results showed that variations in soil cohesion, friction angle, hydraulic conductivity, and soil-water retention can substantially alter the thresholds for landslide triggers. Accurate soil parameterization is essential for reliable landslide risk assessment and effective risk management. The study highlighted the need for detailed soil data to enhance the predictive capabilities of landslide models and improve overall risk management strategies.

A valuable evaluation of TRIGRS's predictive skill for hurricane-triggered landslides was conducted by Liao et al. [99] in a case study in Mason County, North Carolina. The study highlights the model's strengths and limitations in forecasting landslides associated with intense hurricane rainfall. TRIGRS, coded in Fortran, accounts for hydrology, topography, and soil physics to assess slope stability. In the Blue Ridge Mountains of Macon County, North Carolina, an area that experienced widespread landslides during the 2004 hurricane season, the evaluation was conducted particularly due to Hurricanes Ivan and Frances. The study indicated that MaTRIGRS exhibited acceptable spatiotemporal predictive skill for landslide occurrences within a 120-meter radius and for the duration of the hurricane event. It showed potential as a landslide warning system in areas with accurate rainfall forecasts and detailed field data. However, the validation could be enhanced with additional information on landslide failure times, extent, and runout length.

The simulation and prediction of rainfall-induced shallow landslides and subsequent debris flows was highly improved by a hybrid of TRIGRS and DEBRIS-2D models [100]. The integrated approach offered enhanced accuracy in modeling both the initiation of landslides and the dynamics of debris flows. The study highlighted the importance of using comprehensive modeling frameworks to better understand and manage the risks associated with landslides and debris flows, particularly in areas prone to heavy rainfall and complex terrain. The combined TRIGRS and DEBRIS-2D model provided valuable insights into the behavior and impact of these natural hazards, supporting more effective risk management and mitigation efforts.

Yang et al. [101] demonstrated that coupling the physics-based TRIGRS model with the Random Forest algorithm significantly improved landslide susceptibility assessment. The hybrid approach offered enhanced predictive accuracy and a more comprehensive understanding of the factors influencing landslide risk. By integrating detailed physical modeling with advanced machine learning techniques, the study provided a powerful tool for more effective landslide risk management and mitigation efforts.

Abbas [102] examined the use of numerical methods, particularly PLAXIS software, for analyzing slope stability. The study utilized finite element analysis with PLAXIS to simulate various slope conditions, investigating the impact of soil properties, slope geometry, and external loads on stability. Abbas demonstrated the effectiveness of PLAXIS in predicting potential failure mechanisms and compared these numerical methods with traditional analytical approaches. The findings revealed that PLAXIS offered more precise and versatile solutions for complex slope stability problems, highlighting its significance in geotechnical engineering.

Sungkar et al. [103] performed an in-depth analysis of slope stability using both the Bishop and finite element methods. Their study deployed the PLAXIS software for the finite element analysis, revealing that although the Bishop method provides a simpler approach to slope stability assessment, the finite element method delivers a more precise and detailed evaluation, particularly in complex geological conditions. The research underscores the necessity of selecting the most suitable method and software according to the specific requirements of the slope stability analysis.

6.3.2 Highway Slope Types in Maryland

Highway slopes in Maryland, like in many other regions, can be classified into several types based on their geometry, stability, and the methods used for their construction and maintenance. These slope types are crucial for ensuring the safety and longevity of highways, especially in areas prone to geological hazards like landslides. The primary types of highway slopes in Maryland include:

1. Cut Slopes

Cut slopes are created by excavating into natural terrain to provide a stable roadway platform, common in hilly and mountainous regions. The stability of cut slopes depends on the slope angle, geological assessment, and drainage control. The angle must be carefully determined to minimize landslide risks, a thorough geological survey is necessary to evaluate rock quality and potential fractures, and effective drainage systems must be installed to prevent water accumulation and reduce pore water pressure. Cut slopes in Maryland, particularly in the Appalachian Mountains and Piedmont Plateau, face challenges due to diverse geological formations, as highlighted by Brezinski et al. [104]

2. Fill Slopes

Fill slopes are constructed by placing and compacting soil or rock material to raise the ground level for the roadbed, typically used in low-lying or uneven terrain. The quality of the fill material is crucial, as it should be well-compacted and free of organic matter to prevent future settlement or instability. The slope should be designed with an appropriate angle and may require stabilization techniques such as retaining walls or geotextiles. Additionally, erosion control measures like vegetation, riprap, or erosion control blankets are essential to protect the slope surface. In Maryland, fill slopes are common in coastal plain areas and river valleys, where geotextiles and vegetation have proven effective in enhancing stability and erosion resistance.

3. Natural Slopes

Natural slopes are existing landforms that are incorporated into highway design with minimal alteration. These slopes require careful assessment and monitoring to ensure they remain stable and do not pose a risk to the roadway. Geotechnical surveys are necessary to understand soil and rock properties and identify potential instability. Implementing monitoring systems, such as inclinometers or piezometers, is crucial to detect signs of movement or instability. Maintaining vegetation cover helps enhance slope stability by reducing surface erosion and providing root reinforcement.

4. Engineered Slopes

Engineered slopes are specifically designed and constructed to address stability challenges, often involving advanced construction techniques and materials. Utilizing modern engineering solutions like soil nailing, shotcrete, or rock bolting is essential to improve slope stability. Regular inspections and maintenance are crucial to address emerging stability issues and ensure the slope's continued performance. Additionally, implementing adaptive measures such as slope drains, retaining structures, or flexible facing systems is necessary to manage changes in slope conditions. O'Mally et al. [105] reported the application of rammed aggregate pier reinforcements to stabilize the embankment slope on the west face of the southbound Baltimore - Washington Parkway along Route 197, which enhanced slope stability and safety.

Highway slopes in Maryland are diverse and require careful consideration of geological, hydrological, and engineering factors to ensure their stability and safety. Understanding the different types of slopes and the best practices for their design and maintenance is essential for the effective management of highway infrastructure in the state. By incorporating appropriate engineering solutions and maintaining rigorous monitoring programs, Maryland can continue to improve the resilience and reliability of its transportation network.

6.3.3 TRIGRS

TRIGRS is a physical and numerical model that simulates the effects of transient rainfall infiltration on slope stability. The model is a FORTRAN program designed to compute transient pore-pressure changes and the resultant changes in the factor of safety due to rainfall infiltration. It calculates changes in pore water pressure due to rainfall and evaluates slope stability based on these changes. It utilizes the Finite Difference Method (FDM) and operates as a grid-based model, where it divides the study area into a grid of cells and calculates the factors affecting slope stability for each cell based on rainfall intensity, soil properties, and other input parameters. TRIGRS integrates both hydrological and geotechnical processes to predict how rainfall-induced changes in soil moisture affect the stability of slopes. This model is essential for predicting the timing and distribution of shallow, rainfall-induced landslides.

The model is governed by hydrological (Richards) and slope stability equations. Richards' Equation is a major partial differential equation used to describe the movement of water through unsaturated soils. Appendix B1 and B2 shows guide to Performing a TRIGRS Model Run with Topographic DEM from Baltimore, Maryland and a typical TRIGRS initialization file, respectively.

6.3.4 PLAXIS

PLAXIS, developed by Bentley Systems and officially called "PLAXIS Geotechnical Analysis Software," is an advanced tool for geotechnical engineering and structural analysis. It employs the Finite Element Method (FEM) to divide the study area into finite elements, enabling detailed modeling of complex soil and structure interactions. PLAXIS offers a range of soil models and integrates structural elements to analyze deformations, stresses, and stability under various loading conditions. The software features advanced capabilities, including nonlinear material behavior, dynamic load simulations, and construction sequence modeling. It allows for simulation of static and dynamic loading conditions to provide insights into slope deformation and failure mechanisms. PLAXIS is widely utilized in geotechnical engineering for designing and analyzing highway slopes.

6.4 Study Area

The study area encompasses several landslide-prone regions in Maryland, including the Appalachian Plateau, Blue Ridge Mountains, and Piedmont Plateau which are characterized by steep slopes, diverse geological formations, and varying soil types, contributing to their susceptibility to landslides.

6.5 Methodology

6.5.1 Field Investigations

Field investigations play a key role in assessing the physical and geological conditions of slopes. Samples collected during these investigations are analyzed to determine their physical and mechanical properties, which are then used as inputs. An extensive field survey was essential for our geotechnical investigation, providing direct insights into the conditions at various highway landslide locations. This practical approach allowed us to observe the environmental and geological factors contributing to instability at these sites. Our team conducted site visits at thirteen distinct landslide locations along different highways, each presenting unique features and challenges.

Among these sites, some had been stabilized, serving as key examples of successful mitigation efforts. These stabilized sites offered a baseline for evaluating the success of previous treatments and for assessing long-term stability. Additionally, they allowed us to identify any residual or emerging risks. Notably, Site 9 exhibited ongoing drainage issues despite recent interventions, with road embankment degradation already apparent, resulting in visible embankment degradation and highlighting the need for urgent remedial action.

However, not all sites were accessible due to various constraints such as site conditions, location, and safety concerns. Sites 4, 5, 6, and 7 were inaccessible due to safety hazards requiring traffic management, while Sites 3 and 8 were obstructed by dense vegetation, preventing the transport of sampling and surveying equipment. Despite these challenges, we successfully investigated Site 2, where we identified signs of recent landslides, including exposed tree roots and soil deposits. This active site underscored the urgency for prompt action and provided critical insights into dynamic landslide processes, emphasizing the need for immediate and effective geotechnical solutions.

The field survey was also crucial for sample collection and evaluation. By gathering soil and rock samples from various locations, we will be able to perform laboratory tests to determine geotechnical properties and variables influencing landslide susceptibility. Laboratory analysis of these samples will provide a deeper understanding of material composition and generate the soil parameters such as shear strength, cohesion, moisture content, and other factors affecting slope stability. This comprehensive data is vital for developing accurate models and simulations for future landslide risk assessments. Measurements of physical features like slope height, slope angle, slope width and slope length will enhance the creation of realistic models, facilitating the implementation of appropriate mitigation techniques.

In summary, the field survey was pivotal to our geotechnical research, with the aim of delivering essential empirical data and firsthand observations that theoretical studies alone cannot provide. By examining both stabilized and active landslide sites, we have enhanced our understanding of landslide dynamics and refined our mitigation strategies, ultimately contributing to the development of safer and more resilient infrastructure.

6.5.1.1 Site Selection
Sites were selected based on historical landslide records, slope steepness, soil type, and land use. Priority was given to areas with critical infrastructure, such as roads, residential zones, and utilities. More sites are anticipated to be visited.

6.5.1.2 Geological Mapping
Detailed geological mapping was conducted to identify rock types, soil layers, faults, and joints. GPS and total station surveying techniques will be useful to accurately map slope geometry and landslide features. These include elevations, slope angles, slope lengths and slope widths. Other features include the determination of slope strikes and dip angles.

6.5.1.3 Soil and Rock Sampling
Soil and rock samples were collected from various depths using hand and auger methods, boreholes and test pits. In-situ tests, such as Standard Penetration Tests (SPT) and Cone Penetration Tests (CPT), pocket penetrometer, will help to measure the soil material properties in equipment accessible areas.

6.5.2 Laboratory Testing
Laboratory tests for soil and rock in slope stability analysis will include grain size distribution, Atterberg limits (liquid limit and plastic limit), specific gravity, Proctor compaction test, shear strength tests (direct shear, triaxial compression, and unconfined compression), permeability test, consolidation test, density and unit weight tests, moisture content determination, and soil suction test. After the site visits and samples collection are completed, laboratory tests will be carried out at the Geotechnical Laboratory located in the Center for the Built Environment & Infrastructure Studies Building at Morgan State University in Baltimore. These tests will provide critical information on the physical and mechanical properties of soil and rock, essential for evaluating slope stability.

6.5.2.1 Data Analyses
Soil and rock samples will be analyzed in the Geotechnical Engineering Laboratory, Morgan State University, Baltimore, to determine properties such as cohesion, internal friction angle, density, and hydraulic conductivity. Field data will be correlated with historical landslide events and precipitation records.

6.5.3 Geomechanical Modeling

6.5.3.1 TRIGRS Modeling

TRIGRS (Transient Rainfall Infiltration and Grid-Based Regional Slope-Stability Model) is a numerical model used to simulate landslide susceptibility. The TRIGRS model will be used to simulate transient rainfall infiltration and its impact on slope stability. Input parameters will include soil hydraulic properties, rainfall intensity and duration, and initial moisture content. Maps of pore pressure distribution and factor of safety (FS) will be generated over time.

The following equations are used in performing the TRIGRS analyses.

1. Infiltration Models for Wet Initial Conditions

$$\begin{aligned}\psi(Z,t) &= (Z-d)\beta \\ &+2\sum_{n=1}^{N}\frac{I_{nZ}}{K_S}\left\{H(t-t_n)[D_1(t-t_n)]^{\frac{1}{2}}\operatorname{ierfc}\left[\frac{Z}{2[D_1(t-t_n)]^{\frac{1}{2}}}\right]\right\} \\ &-2\sum_{n=1}^{N}\frac{I_{nZ}}{K_S}\left\{H(t-t_{n+1})[D_1(t-t_{n+1})]^{\frac{1}{2}}\operatorname{ierfc}\left[\frac{Z}{2[D_1(t-t_{n+1})]^{\frac{1}{2}}}\right]\right\}\end{aligned} \tag{6.1A}$$

where ierfc (Ψ) is the complementary error function.

$$\operatorname{ierfc}(\eta) = \frac{1}{\sqrt{\pi}}\exp\left(-\eta^2\right) - \eta\operatorname{erfc}(\eta), \tag{6.1B}$$

Ψ is the ground-water pressure head.

t is time.

$Z = z\cos\delta$, where Z is the vertical coordinate direction (positive downward) and depth below the ground surface, z is the slope-normal coordinate direction (also positive downward), and δ is the slope angle

d is the steady-state depth of the water table measured in the vertical direction

$\beta = \cos^2\delta - I_{ZLT}/K_S$;

K_s is the saturated hydraulic conductivity in the Z direction.

I_{ZLT} is the steady (initial) surface flux.

I_{nZ} is the surface flux of a given intensity for the *nth* time interval.

$D_1 = D_O/\cos^2\delta$, where D_o is the saturated hydraulic diffusivity ($D_o = K_s/S_0$, where K_s is the saturated hydraulic conductivity and S_s is the specific storage);

N is the total number of time intervals; and

$H(t-t_n)$ is the Heaviside step function and t_n is the time at the n^{th} time interval in the rainfall infiltration sequence.

2. Slope stability equation:

$$F_S\big|(Z,t) = \frac{\tan\phi'}{\tan\delta} + \frac{c' - \psi(Z,t)\gamma_W\tan\phi'}{\gamma_S Z\sin\delta\cos\delta} \tag{6.2}$$

Where c' is soil cohesion for effective stress, φ' is the soil friction angle for effective stress, γ_w is unit weight of groundwater, and γ_s is soil unit weight.

3. Governing Equations for Unsaturated Initial Conditions

Richards Equations

$$\frac{\partial\theta}{\partial t}=\frac{\partial}{\partial Z}\left[K(\psi)\left(\frac{1}{\cos^2\delta}\frac{\partial\psi}{\partial Z}-1\right)\right] \tag{6.3}$$

$$K(\psi)=K_S\exp(\alpha\psi *)$$

$$\theta=\theta_r+(\theta_s-\theta_r)\exp(\alpha\psi *)$$

where θ is the soil moisture content, K(Ψ) is the hydraulic conductivity as a function of moisture content, h is the pressure head, and z is the vertical coordinate.

To perform a TRIGRS model, the following phases will be undertaken:

1. First, data collection will be conducted, involving the gathering of topographic data as a digital elevation model (DEM), soil properties (such as permeability, cohesion, and friction angle), rainfall data (including intensity and duration), and geological data (like rock type and fault lines).
2. Next, the model setup will proceed by defining the study area and grid size, assigning soil and geological properties to each grid cell, and setting up the rainfall scenario in terms of intensity, duration, and timing.
3. During the model run, the TRIGRS model will be simulating the infiltration and stability of the soil, while also calculating the factor of safety (FoS) for each grid cell.
4. In the post-processing phase, the FoS values will be analyzed to identify areas of high landslide susceptibility, and the results will be visualized using maps and 3D visualizations.

The TRIGRS modeling process is described in Figure 1. After the software has been downloaded from the USGS website and installed on the computer, a more detailed step-by-step guide to running the TRIGRS model is as shown in the flow chat in Appendix 10.1.

When performing a TRIGRS model, the following important considerations are necessary:

a) Ensuring that the input data is accurate and has sufficient resolution to capture the complexities of the study area will be crucial for data quality and resolution.
b) Model calibration and validation will be carried out using historical landslide data and independent data to ensure reliable results.

c) Sensitivity analysis will be performed to understand the impact of different parameters on the model output.
d) Finally, uncertainty analysis will be conducted to quantify the uncertainty in the model output and understand the reliability of the results.

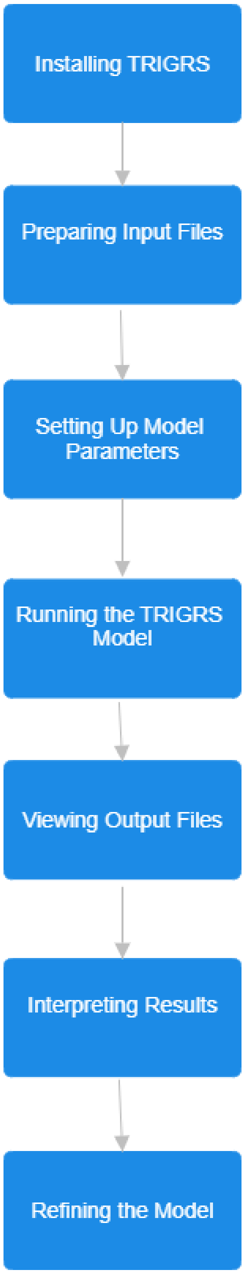

Figure 6.1: The TRIGRS modeling Process

6.5.3.2 PLAXIS Modeling

PLAXIS was utilized for detailed finite element analysis of selected slopes. Both 2D and 3D models were created, incorporating slope geometry, soil stratigraphy, and loading conditions. Simulations were conducted to analyze slope stability under static and dynamic conditions, and deformation patterns and failure mechanisms were evaluated.

PLAXIS is an advanced geotechnical modeling program extensively used in engineering to analyze slope stability and other soil-structure interaction issues. Utilizing finite element techniques (FEM), the software models the response of soil and rock under various scenarios, enabling engineers and researchers to evaluate slope stability and devise suitable solutions for risk reduction.

PLAXIS, slope stability problems are typically analyzed using finite element methods (FEM) rather than traditional limit equilibrium methods (LEM). The primary equations used by PLAXIS to solve slope stability problems include equilibrium equations, constitutive equations, and compatibility equations. A detailed examination of these equations is provided below:

1. Equilibrium Equations

The equilibrium of forces in a continuum mechanics context is described by the following partial differential equations:

$$\nabla \cdot \sigma + b = 0 \qquad (6.4)$$

where:

$\nabla \cdot \sigma$ is the divergence of the stress tensor

b is the body force vector (e.g., gravity)

2. Constitutive Equations

These equations define the relationship between stresses and strains, which depends on the material model used. For a linear elastic material, the constitutive relationship is given by Hooke's law:

$$\sigma = D : \epsilon \qquad (6.5)$$

where:

σ is the stress tensor

D is the constitutive matrix (depends on the material properties)

ϵ is the strain tensor

3. Compatibility Equations

These equations ensure that the strain field is compatible with the displacement field:

$$\epsilon = \frac{1}{2}(\nabla u + (\nabla u)^T) \qquad (6.6)$$

where:

ϵ is the strain tensor

u is the displacement vector

∇u is the gradient of the displacement vector

4. Boundary Conditions

Boundary conditions are essential for solving partial differential equations. They can be expressed as:

$$u = u_0 \text{ on } \partial\Omega_u$$

$$\sigma \cdot n = t_0 \text{ on } \partial\Omega_t$$

where:
$\partial\Omega_u$ is the boundary with prescribed displacements u_o
$\partial\Omega_t$ is the boundary with prescribed tractions
n is the normal vector to the boundary

5. Safety Factor Calculation

To evaluate slope stability, PLAXIS uses the concept of the factor of safety (FoS), which can be determined through a strength reduction method. In this approach, the shear strength parameters (cohesion c and internal friction angle ϕ) are reduced until failure occurs. The equations are:

$$c' = \frac{c}{\mathrm{FoS}}$$
$$\tan(\phi') = \frac{\tan(\phi)}{\mathrm{FoS}} \quad (6.7)$$

where:
c' and ϕ' are the reduced shear strength parameters
c and ϕ are the original shear strength parameters
FoS is the factor of safety

The factor of safety is the value at which the slope reaches a limit state where failure mechanisms are developed.

Virtual modeling enhanced comprehension of the slope's behavior and enabled the efficient development of preventative measures, underscoring the indispensable contribution of PLAXIS in geotechnical engineering. By incorporating real-world data such as soil properties, slope geometry, and groundwater conditions, we created a geotechnical model in PLAXIS. This digital simulation allowed us to manipulate various factors and observe their impact on slope stability. The software's ability to generate multiple slip surfaces, representing potential failure planes within the slope, enabled us to calculate the factor of safety which is a numerical indicator of a slope's resistance to landslides. A factor of safety below 1 indicated an unstable slope, prompting us to explore mitigation measures. In summary, PLAXIS addresses slope stability problems by utilizing a combination of equilibrium equations, constitutive equations, and compatibility equations within the framework of the finite element method. The safety factor for slope stability is typically calculated using a strength reduction technique, which involves systematically reducing the shear strength parameters until failure is observed.

6.6 Summary

This study will highlight the importance of proactive landslide management strategies by combining advanced modeling techniques with field observations and continuous monitoring. The use of TRIGRS and PLAXIS will provide valuable insights into landslide mechanisms and offer practical solutions for mitigating landslide risks in the State of Maryland. TRIGRS is a powerful tool for examining how transient rainfall infiltration affects slope stability, providing comprehensive insights into the timing and distribution of rainfall-induced landslides. While it does have limitations related to sensitivity to initial conditions and assumptions of homogeneity, its integration with GIS and capability to manage complex storm sequences make it an asset for geotechnical and hydrological research.

6.7 Future Work

Field Investigations:

This includes more visitations to the landslide locations, taking measurements and collecting soil and rock samples for laboratory work.

Laboratory Testing:

Samples collected will be tested in the laboratory to determine the engineering properties of the landslides' materials.

Modeling:

Perform TRIGRS and PLAXIS models to simulate various slope conditions, determine the factor of safety and predict landslides susceptibility.

Chapter 7

7. Assessment of Economic Impacts – Preliminary Analysis

Nazah Nova Nur, Benjamin Walrath, Zhuping Sheng, Oludare Owolabi, Yi Liu

7.1 Background

Landslides have had a significant economic impact on individuals, their residences and items of value, manufacturing plants, and vital connections including roads, trains, and communications networks in different states of the US. Due to the strain of growing populations, urban development is pushing into vulnerable slope areas, resulting in significant and seemingly increasing economic losses from slope failures. Large amounts of rock and soil are disrupted by human activity when structures, highways, water reservoirs and dams, drainage channels, and networks of communication are constructed. As a result, industrial activity has contributed significantly to the rise in damage caused by slope failures. Landslides are a crucial component of many big disasters, the extent of which is often missed by the news media. They cause far more economic and casualty losses than is typically acknowledged. For instance, because an earthquake caused the landslide, the 1970 Huascaran tragedy in Peru, which claimed the lives of almost 20,000 people, can sometimes be considered as an earthquake disaster in literature that evaluate disasters; this is regardless of the fact that, a massive, fast-moving debris landslide was the immediate source of the actual devastation, loss, and fatalities.

Natural disasters can devastate a region abruptly and horribly. They can slowly but inevitably drain its resources both psychologically and economically. Damages from natural disasters like tornadoes and earthquakes are unexpected and alarming as they can occur without any advance notice. Decisions on how much money should go into disaster mitigation rather than facility repairs and emergency assistance after an incident are made easier by policymakers at all levels of government when they are aware of the monetary implications and severity of natural disasters. Given the scarcity of resources for studying natural disasters, research priorities ought to take into account the advantages and disadvantages of various courses of action.
Winter & Broomhead [106] summarized the economic impacts of landslide events into three major categories, and these are direct economic impacts, direct consequential economic impacts, and indirect consequential economic impacts. The direct economic impacts are related to the direct costs associated with reconstruction, emergency response expenses, and the replacement or restoration of any lost or damaged infrastructure in its widest sense. The data related to the direct cost is easier to obtain compared to the data related to the indirect costs. The direct consequential economic impacts are further related to interruption of utilities

and infrastructure. As an example, the price of both fatal and nonfatal injuries, as well as the expense of closing a route. Finally, the indirect economic impact is the additional effects of direct investment decisions and the money movement between an institution and its stakeholders are known as indirect economic impacts. They can be financial or non-financial, and it's crucial to evaluate them in accordance with regional and local economies. As an example, if a landslide event affects any rural area where a major part of the economy is dependent on the transportation network the related damages can be related more to due to the disruption of the highway network rather than the landslide event itself. These expenses are an essential aspect of the total economic effect that these kinds of disasters have on society. These expenses further play an important role while allocating funds to conduct the activities related to landslide mitigation. Thus, the data related to the indirect costs are difficult to obtain as they are broadly distributed in terms of both region and society.

This chapter analyzes the economic impacts of landslides, particularly in the state of Maryland with a case example slope. Focusing on both direct and indirect costs, the methodology of this study discounts future costs to the present value and utilizes a cost-benefit analysis of landslide mitigation. This study also uses the indirect costs to estimate the cost-benefit ratio. The indirect costs include relocation of buildings and roadways, measures to prevent or mitigate additional landslide damage, decrease in agricultural or industrial production, decrease in market value of affected properties, tax loss due to decrease in appraised value, and measures to protect health and safety of the public. Costs to the public and private sectors of the economy due to landslide damage are much larger than anticipated. In order to conduct cost-benefit analysis, data is collected from the United States Geological Survey, Maryland Department of Agriculture, Maryland Department of Commerce, and Maryland Department of Transportation. We expect to find the social benefits which include reduced property damage and infrastructure losses, lower emergency response and recovery costs, insurance and financial benefits are greater than the total cost. Thus, making the project more beneficial to the community with a cost-benefit ratio of more than one which correlates to a positive net present value.

7.2 Related Literature

Previous studies related to the different types of costs of landslide damage are mainly based on various case studies. Winter et al. [107] highlighted the economic impacts of landslides and floods in Scotland in August 2004. The case study focuses on the series of debris flow with monthly average rainfall affecting transportation networks and rural communities. Due to climate change flood events can also increase frequently and can cause same threat towards the economy [108-111]. The previous studies of Schuster [112], Highland [113], Schuster & Highland [114] are particularly instructive and useful in choosing the methodology for these case studies. Both Klose et al. [115] and Highland [116] deal with direct economic impacts and direct consequential economic impacts. According to Highland [120] economic activities can vary in areas due to the different access routes on both sides of landslide incidents. Porter et al. [117] estimated economic impacts of the prairie landslides in Western Canada with total impacts exceeds \$281 to \$450 million annually. According to the authors the findings are significant as they can aid in standardization and provincial estimates of the risk of landslides. It can further help the decision makers to comprehend the danger and risk of landslide events affecting both government and industry. Thus, they can allocate the budgets accordingly to conduct the activities related to the landslide mitigation. According to the natural resources of Canada the total estimation of direct and indirect costs in Canada due to landslides vary between $200 to $400 million.

Schuster and Highland [118] highlighted the socioeconomic and environmental impacts of landslides in the Western Hemisphere. Based on U.S. Geological Survey the study focuses on the economic losses of landslides in Western Hemisphere due to increased construction in areas vulnerable to landslides. The ongoing high rate of deforestation brought on by timber harvesting, smoldering and industrialization is linked to population growth and raises the risk of landslides on the world's slopes. The landslides that resulted from the 1964 Alaska earthquake, the 1980 rainfall-induced landslides in southern California, the 1982 landslides in the San Francisco Bay area, the 1983–1984 El Nino-triggered landslides in the State of Utah, and the 1998 El Nine-related landslides in California have all caused the most devastating economic damage in the United States in recent decades. According to Krohn & Slosson [119] the annual cost of landslide in US is about 400 million in 1971 without including the indirect costs related to the public property, agricultural and industrial production, transportation and other facilities related to communication. Jahns [120] analyzed the expenses of damages from several natural disasters over a 50-year span, from 1925 to 1975. Unadjusted for inflation, the total losses from earthquakes, hurricanes, tornadoes, and floods during that time approached $20 billion. In contrast, during the same time, there was at least $75 billion worth of movement of the ground of two different types: subsidence and landslides.

7.3 Methodology

While talking about the economic impacts of Landslides we have considered both direct and indirect costs for a single event. To evaluate the indirect costs, we have implemented Cost-Benefit analysis. An organized process for assessing the financial, social, and environmental consequences of an initiative, regulations, or decisions is called cost-benefit analysis, or CBA. To ascertain if and by how much the benefits outweigh the costs, it entails comparing the overall predicted costs of a course of action or decision to the total expected benefits. The process further helps in developing well-informed judgments that optimize overall benefits to the community. First, we assign monetary values to each identified cost and benefit. Then we calculate the benefit-cost ratio and finally calculate the net present value by subtracting the total present value of cost from the total present value of benefit. All the results are estimated and are in the preliminary stage. The equations of the described methodology are as following:

$$\text{BCR} = \text{PV (Benefits)}/\text{PV (Costs)} \tag{7.1}$$

$$\text{Net Present Value} = \text{PV of benefits} - \text{PV of Costs}. \tag{7.2}$$

7.4 Data Sources

To evaluate the direct costs, the data are collected from a survey which recorded the cost of repairs to state highways caused by landslides for the five-year period between 1986 and 1990 [121]. The results are further adjusted for inflation. Previous studies have been taken into consideration to show the landslide correction costs in US highway systems, transportation infrastructure in the United States and different types of risk reduction infrastructure. To evaluate the indirect costs, the data is collected from the United States Geological Survey (https://www.usgs.gov/programs/landslide-hazards), Maryland Department of Agriculture (https://mda.maryland.gov/), Maryland Department of Commerce (https://commerce.maryland.gov/), and Maryland Department of Transportation. Since the project specializes on a single event to conduct Cost-Benefit analysis we have listed all the costs and benefits associated with the project. We have further quantified all these costs and benefits in monetary terms accordingly.

7. 5 Results of Case Examples

7.5.1 Direct Cost

Table 7.1 takes data from a survey which recorded the cost of repairs to state highways caused by landslides for the five-year period between 1986 and 1990, in two categories: contracts awarded and maintenance [121]. Importantly, that study only evaluated state roads; Interstate highways were not included. "[That represents] only 20.7% of the 3,876,500 miles of roadway under public … jurisdiction in the U.S. [121]." Adjusting either figure for the total number of highway miles at the time is a simple rate problem, however.

$$\therefore \frac{\$\, Cost\ (Contr. or\ Manit.)}{Dep. Var. (Study\ mi.)} = \frac{\$\, Adj. Cost}{Ind. Var. (Total\ mi.)} \tag{7.3}$$

To account for growth in the public highway sector from 1990 to 2023, the difference quotient of total highway miles is first obtained using data from another study [122]. It is important to note that—while the article was published in 2020—the data point used for this step is the sum of Rural and Urban highway miles in 2008, the most recent year listed.

$$\therefore \frac{Highway\ miles\ (2008) - Highway\ miles\ (1990)}{18} = Growth\ (mi.)/year \tag{7.4}$$

Costs are next adjusted for growth—by equating ratios—as before.

$$\therefore \frac{\$\ Init. Cost}{Dep. Var. (1990\ mi.)} = \frac{\$\, Adj. Cost}{Ind. Var. (2023\ mi.)} \tag{7.5}$$

Finally, results are adjusted—year-by-year—for inflation. The calculations were performed in Excel™, using the published inflation rate for each year of the interval (123). Extrapolated to their present [2023] value, the study metrics equate to roughly $1.3 billion.

Table 7.1: Assessment of direct costs

		Jurisdiction				
Title	**Published**	**State**	**Public**	**Category**	**Cost**	**Totals**
Landslide Correction Costs on U.S. State Highway Systems	**1992** (1990 data)	**803,000** mi. (**20.7%** of total)	**3,876,500** mi. (total)	**Contracts**	**$68.5** million	**$159.9** million
$\frac{\$\text{Cost (Contr. or Maint.)}}{\text{Dep. Var. (Study miles)}} = \frac{\$\text{Adj. Cost}}{\text{Ind. Var. (Total miles)}}$				**Maintenance**	**$37.4** million	
Transportation Infrastructure in the United States	**2020** (2008 data)	**Rural**	**Urban**	4,042,778 −3,876,500 166,278		
		2,977,222 mi.	**1,065,556** mi.			
		Total: **4,042,778** mi.		Difference: **166,278** mi.		
$\frac{\text{Highway miles (2008)} - \text{Highway miles (1990)}}{18\ \text{yrs.}} = \text{Growth (mi.)/year}$						+ ~**9,237**$^{2}/_{3}$ mi./yr.
					Growth (1990 – 2023)	**304,858** mi.
					(Estimated) **Highways as of 2023**	**~4,181,358** mi.
U.S. Inflation Rate by Year: 1929 to 2024	**2024** (2023 data)	$\frac{\$\ \text{Init. Cost}}{\text{Dep. Var. (1990 mi.)}} = \frac{\$\ \text{Adj. Cost}}{\text{Ind. Var. (2023 mi.)}}$				
			Initial	**Contracts**	~**$771.8** million	
				Maintenance	~**$421.4** million	
		$A = Pe^{rt}$	**Inflated**	**Contracts**	~**$830.6** million	
				Maintenance	~**$453.5** million	
						~$1.3 billion

The Walkinshaw's article lamented a lack of adequate preliminary evaluation by geotechnical engineers during construction and realignment of the interstate highway system [124]. With even scarcer resources, state highway departments face costly interventions in the aftermath of catastrophic failures because maintenance personnel failed to address small problems early—or correctly identify their root cause. "Roads broken by slow landslide movement often have layers of road patching several feet thick," by one account [124].

Following an abnormally prolific rainfall event that affected San Diego County, California, in 1978, engineering geologists Slosson and Krohn surveyed debris flow damage to homes in the Los Angeles area as part of a building code review [125].

Extrapolated nationally, their data put private property damage at roughly $400 million annually [125]. Assuming their methodology was sound, the inflation-adjusted value of private losses would be nearly $2.1 billion today. Taken together, these figures give a conservative approximation of the direct economic cost of landslides in the U.S.: $3.4 billion. Even if the annual cost of repairing landslide damage to the national highway system could be precisely quantified, that information would be of little value in a cost-benefit analysis. A more useful input would be the unit cost of various mitigation strategies. Adjusting for inflation, Table 7.2 shows this for three types of abatement infrastructure, in descending cost order [115]. Table 7.3 likewise gives the unit cost for several methods from another study—this one focused on large landslides [126]

Table 7.2: Costs for different mitigation approaches

Method	**Area/Length**	**Cost**	**Year**	**Inl. Adj.** †	**Unit Cost**
Soil-nailing (12 m. depth)	4,300 m.^{2}	$2.16 M.	2001	$3.67 M.	$853 / m.^{2}
Soil-Nailing (6 m. depth)	8,300 m.^{2}	$2.48 M.	2006	$3.68 M.	$443 / m.^{2}
Infill Buttress (6 m. depth)	20 m.	$180 k.	2003	$293 k.	$14,632 / m.
Infill Buttress (6 m. depth)	75 m.	$640 k.	2007	$911 k.	$12,146 / m.
Infill Buttress (6 m. depth)	550 m.	$4.06 M.	2007	$5.78 M.	$10,507 / m.
Catch-Fence, L.E. (<100 kJ.)	470 m.	$260 k.	2005	$395 k.	$841 / m.

† Inflation adjusted, year-by-year, using the formula: $A=Pe^{rt}$ [123]

Table 7.3: Summaries of construction costs for three measures

Mitigation Method	**Construction Costs (2002)**	**Engineering Costs (2002)**	**Total Cost (2002)**	**Inflation Adjusted Cost (2023)** †
Horizontal Drains	30 Drains @ $15 to $20/ft. = $225k. to $300k.	$100k.	$325k. to $400k.	~$539k. to ~$663k.
	60 Drains @ $15 to $20/ft. = $450k. to $600k.	$200k.	$650k. to $800k.	~$1.1M. to ~$1.3M.
Key Trench	20 ft. wide Key @ $5 to $15/yd. = $1.5M.	$200k.	$1.7M.	~2.8M.
	40 ft. wide Key @ $5 to $15/yd. = $2M.	$600k.	$2.6M.	~4.3M.
Shear Piles (w/ Tie-Backs)	120 2 ft. dia. Piles on 5 ft. centers @ $215/ft. = $2M.	$500k.	$2.5M.	~$4.1M.
	75 4 ft. dia. Piles on 8 ft. centers @ $490/ft. = $2.8M.	$900k.	$3.7M.	~6.1M.

† Inflation adjusted, year-by-year, using the formula: $A=Pe^{rt}$ [123]

Table 7.4 summarizes three case studies explored in detail in the Hammond article [126].

Table 7.4: Costs estimate for three different measures

Site	**Scale**	**Mitigation Method**	**Cost**	**Infl. Adj. Cost**	**Result**
Ditch Camp Slide (Sandy, OR.)	1,200 ft. W. x 900 ft. L. x ~40 ft. D.	29,000 ft. of Horizontal Drains Installed	$400k. (1997)	$745k. (2023)	Satisfactory Stability
Scenic Loop Highway Slide (Pacific City, OR.)	850 ft. W. x 500 ft. L. x ~45 ft. D.	9,000 ft. Horizontal Drains Installed 45,000 yds^3 Shear-Key Placed 750 ft. of Trench Drains Excavated 1,000 ft. of Highway Rerouted	$1.5M. (1999)	$2.7M. (2023)	Good Stability
Goat Lick Slide (Glacier National Park, MT.)	220 ft. W. x 420 ft. L. x ~40 ft. D.	1,670 Linear ft. of 4 ft. Dia. Shear-Piles, with 53 Tie-Backs Installed Cantilever Bridge [Re]built	$1.5M. (1993)	$3.1M. (2023)	Good Stability

† Inflation adjusted, year-by-year, using the formula: $A=Pe^{rt}$ [123]

Remediation methods—and therefore costs—for [large] landslides vary depending upon site considerations as determined from a geotechnical engineering assessment [126]. In ascending order of cost—one, or ideally, a combination of approaches—increasing drainage, earthworks, and the placement of structural elements may be used to improve slope stability [126]. There are viable alternatives, though, such as planting native species to help retain the soil, relocating roadways, or excavating drainage basins to absorb debris flows [115]. These are considered best practices wherever improvements to existing highways or construction of new one's permit. Determining their unit cost, however, is only possible on a case-by-case basis.

A review of the literature identified a knowledge gap in definitive data on the direct [and indirect] economic impacts of landslides. Existing work that attempts to quantify the costs is frequently self-referencing. Studies cited here were curve-fitting to a single estimate published 44 years earlier [127]. Approximations must, therefore, be viewed with appropriate skepticism, as our methodology relies on the same, outdated data [128]. Another problem is ambiguity in attributing cause to event, as the deadly debris flow in Montecito, California, demonstrates. The relationship between slope stability and excessive precipitation is well understood. However, the disaster occurred months after the Thomas wildfire had burned through the impacted area [129]. So, was the root cause a wildfire or excessive rainfall? …Lack of proper forest management, or arcing from a wind-whipped power line?

Furthermore, highway administrators' classification of expenses in one state may differ from how similar spending is recorded in another, making it difficult to identify even the proximate cost of landslides. Where private property is involved, losses may be covered by insurance policies, making them partially or wholly invisible in public budgets. It is fair to say the traveling public vastly underappreciates the impact of landslides, including the expense of infrastructure, and the cost to maintain it. There is a prescient need for comprehensive, up-to-date research into their true cost to our transportation network.

7.5.2 Indirect Costs

Table 7.5 starts with the main cost of the project which is the landslide mitigation measures and their costs. As we estimated our cost for a single event in Maryland the estimated costs for landslide mitigation includes total cost for the retaining structure, total cost of reinforcement, and finally the overall cost to prevent and mitigate landslide damage. The scales, numbers of elements, and the costs are adjusted accordingly. Thus, our total cost for the retaining structure is 55,000, total cost of drainage control $720,400, and the total cost of reinforcement is 3.5 M. After adding 20% of the engineering design our final cost is 3.94 M as an example.

Table 7.6 includes the decrease in agricultural and industrial production in Maryland due to a single landslide. According to the table we assume that there is no estimated loss for crop damage as no farmland has been affected due to the landslide. Next, we estimated the impact of the landslide on the industrial production. We assume overall one site has been affected by the single slope and the repair cost is 2 million for that industry site. Again, the production halt and delays for that site is 1 million. Thus, the combined total impact is 3 million. Since these are the estimation of decrease in agricultural and industrial production due to landslide events and after taking the mitigation measures to prevent further damage, we are assuming to avoid these costs. Thus, the community can benefit from regaining the loss in agriculture and industrial production.

Table 7.5: Landslide Mitigation Measures and their Costs

Landslide Mitigation Measures and Their Costs		**Scales**	**Numbers of elements**	**Costs**	**Notes**
Regrading slopes	$27,500	1 acre= 43560 sq ft	2	$55,000	
Retaining Walls	$200,000	per ft, 9 ft L, 4.5 ft D, 2.75 ft W	0	$0	
Vegetative Stabilization	$60,000	per ft, 22.5 ft W	0	$0	
Soil nail (6 m deep)	$443	per sq. m	0	$0	
Soil nail (12 m Deep)	$853	per sq. m	0	$0	
Total Retaining Structure	$288,796			$55,000	
Surface Drainage System	$50	per ft	40	$2,000	
Subsurface Drainage System	$60	per ft	50	$3,000	For a single event, 1 slope
Total cost of Drainage Control	$110			$5,000	
Rockfall Barriers	$200	per linear foot	2	$400	
Fences	$900	per m	800	$720,000	
Total Cost of Rockfall Protection	$1,100			$720,400	
Road Reinforcement	$2,500,000	per mm, T40 (40mm)	1	$2,500,000	
Total Cost of Reinforcement	$2,500,000				
Total Estimated Cost to Prevent and Mitigate Additional Landslide Damage	$2,788,710			$3,280,400	
Cost of Eng Design (20%)				**$656,080.0**	
Overall				**$3,936,480**	

Table 7.6 Decrease in Agricultural and Industrial Production

Categories	**Parameters**	**Notes**
Average crop value	$1,500	
Farmland affected by landslide	0	
Estimated Loss for Crop Damage	$0	
Cost of soil remediation and infrastructure repair	$500	per acre
Additional Cost	$0	
Total Agricultural Impact	$0	
Industrial Sites	1	Assume
Average Repair cost	$2,000,000	per site
Total Cost	**$2,000,000**	
Production Hults and delays	$1,000,000	Per site
Additional Costs	**$1,000,000**	
Total Industrial Impact	$3,000,000	
Combined total Impact	**$3,000,000**	

Next is Table 7.7 which is the decreased market value of the affected properties due to a single landslide event in Maryland. According to Maryland Department of Assessments and Taxations the average property value in Maryland is 350,000 and by assuming the number of properties over one slope which is 10, we get the estimated total property value for that landslide event is 3.5 million. According to previous studies the reduction of property values due to landslides varies between 10%-20% and thus, the estimated decrease in the property values due to landslides is $525,000. After taking the landslide mitigation measures to avoid further damage, we can also avoid this cost and thus the value of the properties will be regained which can be considered as a major contribution towards the economy.

Table 7.7: Decreased Market Value of the Affected Properties

Categories	**Parameters**	**Notes** (For a single event, 1 slope)
Average property value in Maryland	$350,000	
Number of properties over one slope	10	Assumed
Total property value in landslide prone areas	$3,500,000	
Reduction of property values due to landslide	10%-20%	Academic studies
Estimated Reduction in Value	**$525,000**	

Table 7.8 is the tax loss due to the decrease in appraised value for the landslide event in the State of Maryland. Our Table 7.8 aligns with Table 7.7 as we have multiplied the decrease in property value with average property tax rate in Maryland. According to Maryland Department of Commerce the average property tax rate in Maryland is 1.1% and according to Table 7.7 the decrease in property value is $525,000. Thus, the total tax loss for the single event is $5,775. After undertaking the landslide mitigation measures, we expect to avoid the damages at least 70% and thus the total tax loss can be regained which also add value to the community.

Table 7.8: Tax Loss Due to Decrease in Appraised Value

Categories	**Parameters**
Average property tax rate in Maryland	1%
Decrease in Property value	$525,000
Total Tax loss	**$5,775**

Our next table is Additional Benefits, which includes the other benefits we will get due to the implementation of the mitigation measures of landslide damages. Our Table 7.9 consists of savings in emergency response and recovery costs, enhanced public safety and health, preservation of environmental and natural resources, and improved community resilience and livelihood. According to the table below the overall additional benefit we get is $885,000.

Table 7.9: Additional Benefits

Categories		**Notes-For a Single Event**
Average annual emergency response costs	$150,000	
Expected reduction in emergency response costs	0.6	
Emergency Response Savings	$90,000	
Average annual recovery costs	$400,000	
Expected reduction in recovery costs	0.6	
Recovery Costs Savings	$240,000	
Enhanced Public Safety and Health		
Value of reduced injuries and fatalities	$125,000	
Healthcare cost savings	$50,000	
Overall public safety and health benefits	$175,000	
Preservation of Environmental and Natural Resources		
Value of preserved ecosystem and biodiversity	$80,000	
Improved Community Resilience and Livelihoods		
Economic stability benefits	$200,000	
Quality of life improvements	$100,000	
Community Resilience and Livelihood Benefits	$300,000	
Overall Additional Benefits	**$885,000**	

Our next and final table is the cost-benefit analysis. Thus, our Table 7.10 aligns with the previous results. According to Table 7.5 total estimated cost to prevent and mitigate additional landslide damage is the only projected cost in our cost-benefit analysis which is about 3.94 million for an assumed case. Our estimated total benefits after implementing the mitigation measures includes regained market value of the affected properties, regained agricultural and industrial productions, regained tax loss, and additional benefits. Thus, our estimated total benefits after implementing mitigation measures to avoid landslide damages 4.42 million.

Table 7.10: Cost-Benefit Analysis

Categories	**Parameters**

Total estimated cost to prevent and mitigate additional landslide damage	$3,936,480
Estimated Total Benefits after mitigation measures	
Regained market Value of the Affected Properties	$525,000
Regained Agricultural and Industrial Production	$3,000,000
Regained Loss of Tax	$5,775
Additional Benefits	$885,000
Overall benefit	**$4,415,775**
Cost-Benefit Ratio	**1.12**
Net present Value (PV of benefit- PV of Costs)	**$479,295**

Thus, by dividing Overall Benefits by estimated total costs we got the Benefit-Cost Ratio of 1.12 with a net present value of $479,295. Since BCR is more than one and NPV is positive the project is considered as viable. Please note that in some cases some of the benefits may not be counted in monetary values. Therefore, BCR may not fully reflect the benefits of preventive measures for geohazards reduction.

7.6 Conclusions

This chapter analyzes the economic impacts of landslides in Maryland with an assumed case slope area. To evaluate the direct costs the data are collected from a survey which recorded the cost of repairs to state highways caused by landslides for the five-year period between 1986 and 1990. The results are further adjusted for inflation. Previous studies have been taken into consideration to show the landslide correction costs in US highway systems, transportation infrastructure in the United States and different types of risk reduction infrastructure. To evaluate indirect costs first, we assign monetary values to each identified cost and benefit. Then we calculate the benefit-cost ratio and finally calculate the net present value by subtracting the total present value of cost from the total present value of benefit. All the results are estimated and are in the preliminary stage. We found the benefit cost ratio more than one which correlates to positive net present value and thus making the project more beneficial to the community. One of the major limitations of our research is the results of the indirect costs are the initial evaluation of the collected data. Thus, we need additional data collection to conduct further analysis on the economic impacts of landslides. We can further run a regression model to see if the effects are significant on the mitigation process of landslide.

Chapter 8

8. Summaries

8.1 Conclusions

This report summarizes work completed for the phase 1 of the project. They include:

- Preliminary site investigation and sample collection at selected sites based on historical landslides inventory.
- Characterization of landslides using LiDAR and InSAR data for the selected counties, proving their applicability in identifying and detecting potential landslides.
- Demonstration of integration of watershed hydrological model with slope stability model, focusing on impacts of precipitation on the slope stability using Anacostia watershed.
- Preliminary review of physical models, TRIGRS and PLEXIS.
- Preliminary assessment of economic impacts of landslides and benefits of preventive measures based on direct costs and indirect costs.

They are parts of the multi-phase project, aiming development of landslides risk assessment and early warning smart system. The Phase 1 work provides a strong foundation for next phase.

8.2 Future Work

The phase 2 will expand site investigation with additional survey and soil sampling. Laboratory tests will be carried out. LiDAR and InSAR images processing and interpretation will be further enhanced by integrating with other photo imaging approaches and site image acquisition. Physical models will be developed based on site investigation and laboratory test results. Multiple scenarios will be simulated to gain a better understanding controlling and triggering factors, which will be feed into the machine learning model to assess risk assessment of slope failure. Sensors and other monitoring technologies will be evaluated in cooperation with CMU and other partners within UTC Safety 21 program and beyond.

Appendix for Chapter 3

A3.2.1 Basic Soil Properties Testing

A3.2.1.1 Particle Size Analysis

The Particle Size Analysis test gives us a good idea about the constituents of soil. It tells us how much clay, silt, sand and gravel are present in our soil sample. This information is crucial to understanding drainage, permeability, and strength of soil for evaluating soil slope stability.

The conventional and most often used technique for determining particle size is still sieve analysis. The sample is agitated for five to ten minutes through a stack of sieves with progressively larger aperture sizes, dispersing the particles according to size (Figure A3.1). The method tends to measure particle width, as particles pass through the smallest possible aperture based on their orientation. The process continues until the mass on each sieve remains constant. Each sieve is then weighed to calculate the volume of each fraction by weight, resulting in a mass-related distribution. The obtained result is then used to determine the type of soil sample according to the different soil classification systems.

Figure A3.1: Stacked Sieves used for particle test.

A3.2.1.2 Atterberg Limits

Atterberg limits are a primary measure of critical water contents on fine-grained soils. This is an inexpensive and well-documented way of determining the engineering properties of soil. We used the Casagrande method to determine the liquid limit of soil (Figure A3.2).

Figure A3.2 Liquid limit testing device: Casagrande method (source: https://tinyurl.com/yuercn5k**)**

The Casagrande technique is a method used to establish the liquid limit of fine-gained soil, which is the point of moisture content where clay soils change from a plastic to a liquid state. The process includes blending soil sample with water to form a paste, transferring the paste into a cup, and carving a groove in the middle of the paste. The cup is dropped multiple times in a typical manner until the groove seals shut, and the liquid limit is determined by the number of drops needed to close the groove at a specific distance.

To find the Plastic Limit, a small ball of wet soil is shaped and rolled by hand into a 1/8 in thread multiple times. This test can also be conducted using a plastic limit roller device. The Plastic Limit is the moisture level at which the thread breaks before it can be fully rolled out. The shrinkage limit is a specific property of soil, particularly fine-grained soils like clay. It is defined as the maximum water content at which a reduction in water content does not cause a decrease in the volume of the soil. In other words, at the shrinkage limit, the soil is fully saturated, and any further loss of moisture will not result in further shrinkage (Figure A3.3).

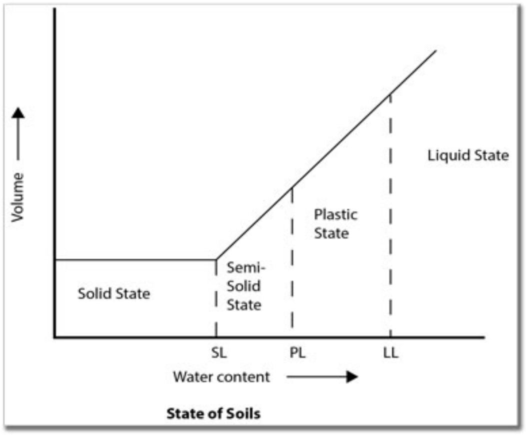

Figure A3.3: Atterberg Limit Consistency States of Soils (source: https://tinyurl.com/2777bc49).

A3.2.2 Mechanical Properties Testing

A3.2.2.1 Direct shear

Direct shear test is a simple and cost-effective way to measure the shear strength of soil, which is important for geotechnical engineers to design foundations, slopes, retaining walls, and pavements. The test is done by placing a soil sample in a shear box and applying a normal stress (vertical load) to it (Figure 3.4). Then, a horizontal force is applied to the top half of the shear box until the soil fails. The shear strength is determined.

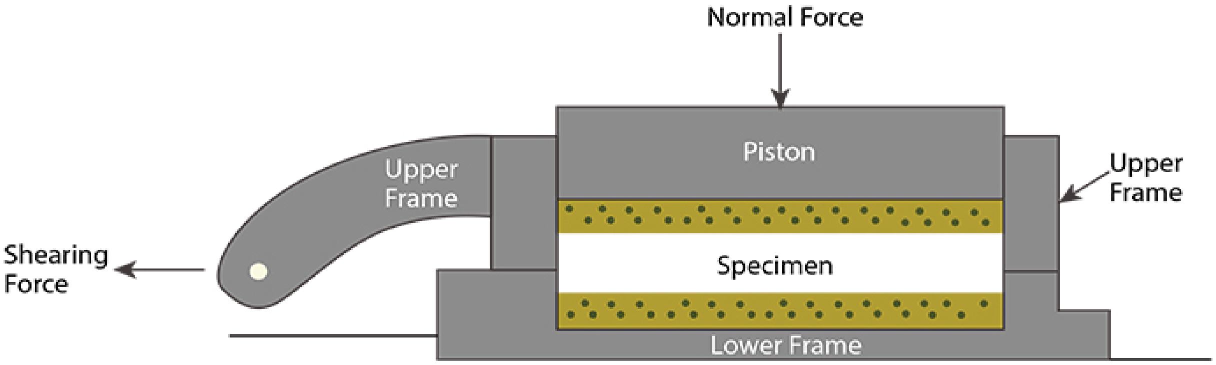

Figure A3.4: Representative image showing direct shear test of specimen (source: Gilson Company Inc.).

Proper sample preparation is crucial for accurate direct shear tests. Specimens should be prepared in a humid environment to maintain moisture, starting with a sample large enough for at least three identical specimens. Undisturbed samples should be carefully cut from a more significant initial sample on a non-absorbent surface using a sharp-edged cutter matching the shear box dimensions. Compressing or disturbing the prepared sample should be avoided. Errors often occur during trimming or transferring the sample. After cutting, the specimen should be placed in the shear box by pressing it out of the cutter smoothly, using waxed paper to prevent sticking. The shear box is ready for testing once the top filter and porous stone are added (Figure A3.5 and A3.6).

Figure A3.5: Sample cutter and extruders (source: Gilson Company Inc.).

Figure A3.6: Shear Box and porous stone (source: Gilson Company Inc.).

A3.2.2.2 Triaxial Shear Test

Triaxial testing is a form of shear testing conducted on solid materials while they are subjected to confining pressures from all directions. Confining pressures are created in a fluid chamber to mimic the pressures exerted by nearby soil materials (Figure A3.7). It can then provide a more accurate representation of how materials behave in their current in-situ location. This testing principle is relevant for soil, rocks, powders, and construction materials.

Specialized sample preparation equipment is used to shape and trim soil samples to size. The samples may be undisturbed and extruded from thin-walled tube (Shelby tube) samplers, or they can be remolded or compacted in the laboratory. Using a test cell kit and other tools and accessories, a latex membrane to regulate fluid movement, porous stones at either end, a cover, and a pedestal for installation in the test cell are fitted.

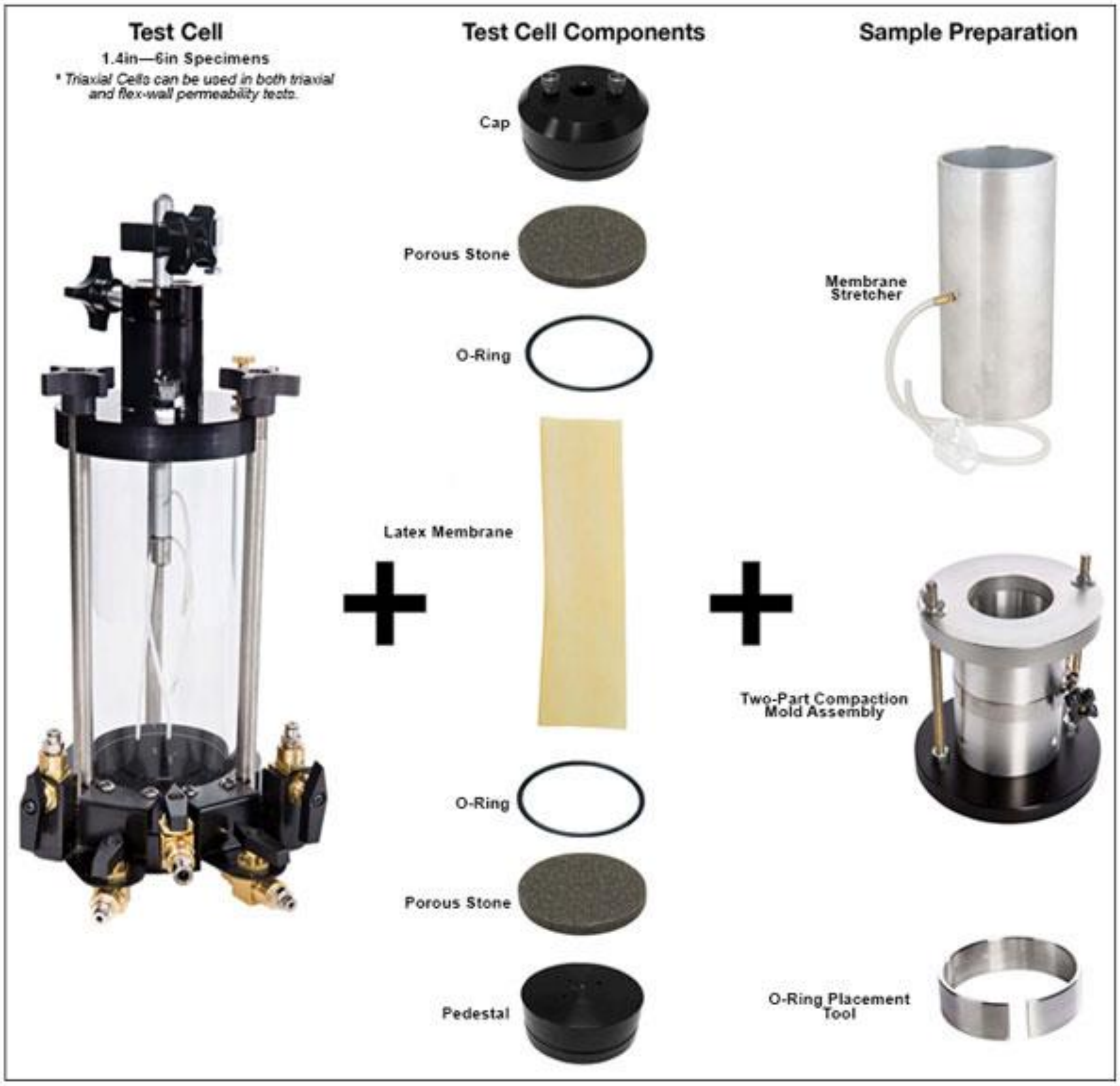

Figure A3.7: Equipment needed for Triaxial test (source: Gilson Company Inc.).

The assembled test cell with the prepared specimen and water is mounted in the load frame, and air and water lines are connected to the triaxial control panel. Measurement instruments are installed and zeroed. Triaxial tests consist of three phases: saturation, consolidation, and shear, each with unique steps per test method. Saturation fills all soil voids with water using deaired water and back pressure, enhancing saturation by compressing air into the solution. During consolidation, confining pressures are applied; in the UU (Unconsolidated Undrained Test) test, drainage is not allowed, and saturation prevents consolidation, whereas in CU (Consolidated Undrained Test) and CD (Consolidated Drained Test) tests, drainage and volume change occur until equilibrium. Shear involves axially loading the specimen; UU tests have a quick loading rate to induce failure within 15 minutes, while CU and CD tests require calculated, slower strain rates, extending test times to days or weeks (source: https://www.globalgilson.com/blog/triaxial-shear-test-of-soil).

A3.2.3 Hydraulic Properties Testing

A3.2.3.1 Permeability Test

This test measures the water flow rate through soil, which is crucial for designing drainage systems and assessing groundwater movement. Common methods include constant head and falling head permeability tests. Soil permeability tests are conducted either under conditions of constant head or conditions of falling head. The Constant Head Test is a setup where the top of the water column maintains the same height above the sample during the entire test. The test is appropriate for soils with high permeability such as sands, gravels, and certain clay soils. The Falling Head Test involves the sample's head decreasing as water infiltrates, causing a gradual decrease in pressure during the test. Head falling techniques are typically restricted to soils with fine particles.

The ASTM D5084 standard outlines various techniques for assessing the hydraulic conductivity of soils using Flexible-Wall Permeability Cells (see Figure A3.8). This standard provides different options for conducting constant and falling head tests, such as tests for flow rate consistency and tests for constant volume under controlled pressures. The test sample can be created using either intact borehole samples (Shelby tubes) or by compacting soils in a mold to a specific density. The specimen is enclosed in a latex membrane and inserted into a pressurized test cell filled with fluid. Valves and burettes on a logic panel control confining pressures on the sample and permanent (usually water) in three dimensions. Sample deformation and volume change are continuously monitored during the procedure.

Figure A3.8: Flexible-Wall Permeability Cells for soil permeability test.

Appendix A

A: InSAR and LiDAR maps

A1. Cumulative Displacement Plots

Allegany County

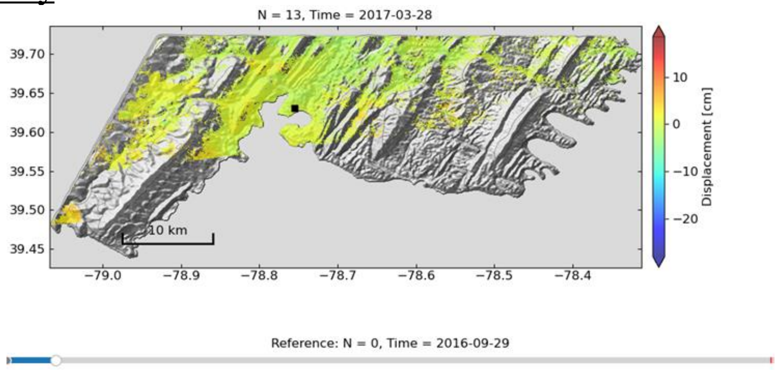

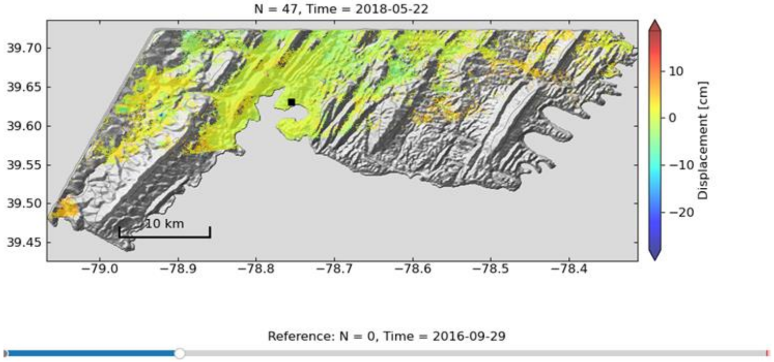

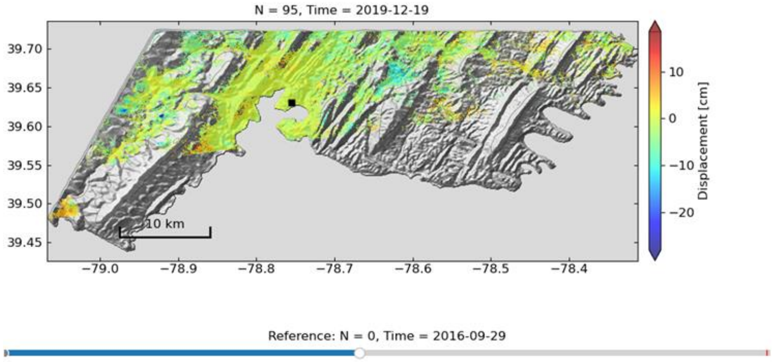

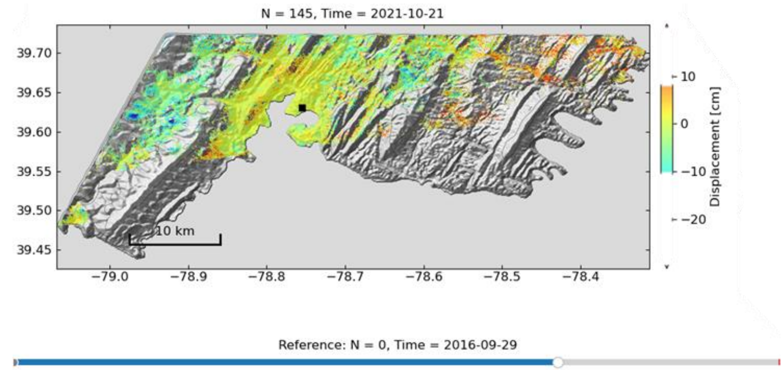

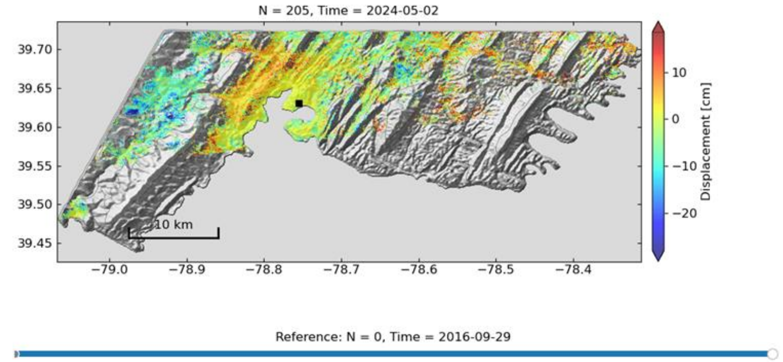

Talbot County

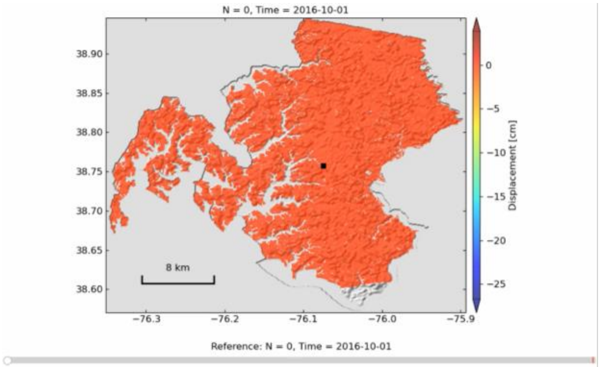

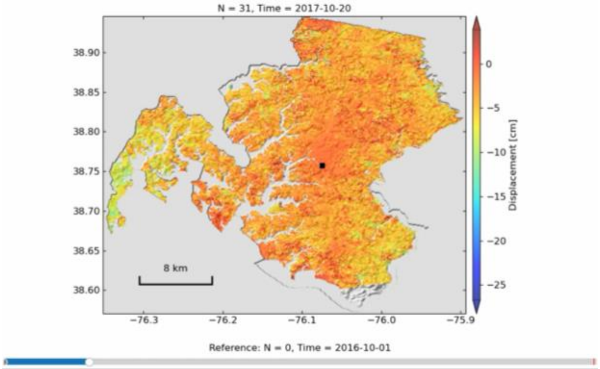

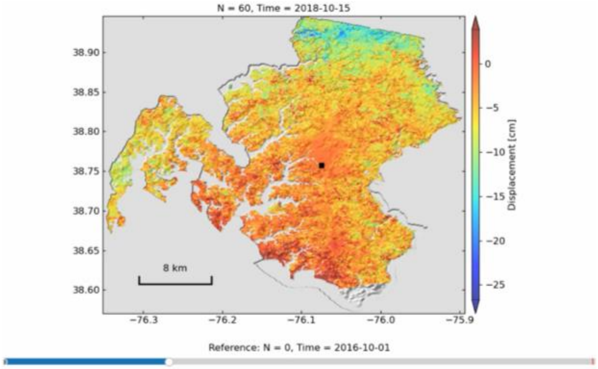
N = 60, Time = 2018-10-15
38.90
38.85
38.80
38.75
38.70
38.65
38.60
8 km
−76.3
−76.2
−76.1
−76.0
−75.9
0
−5
−10
−15
−20
−25
Displacement [cm]
Reference: N = 0, Time = 2016-10-01

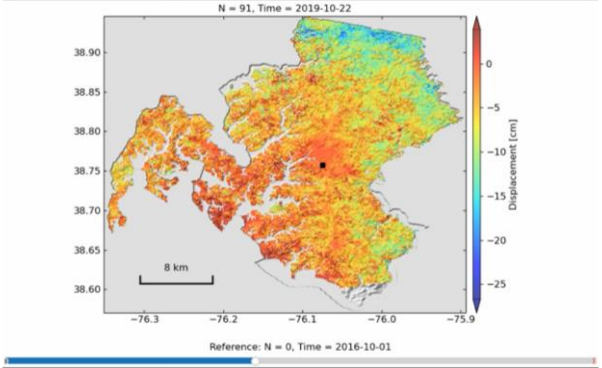
N = 91, Time = 2019-10-22
38.90
38.85
38.80
38.75
38.70
38.65
38.60
8 km
−76.3
−76.2
−76.1
−76.0
−75.9
0
−5
−10
−15
−20
−25
Displacement [cm]
Reference: N = 0, Time = 2016-10-01

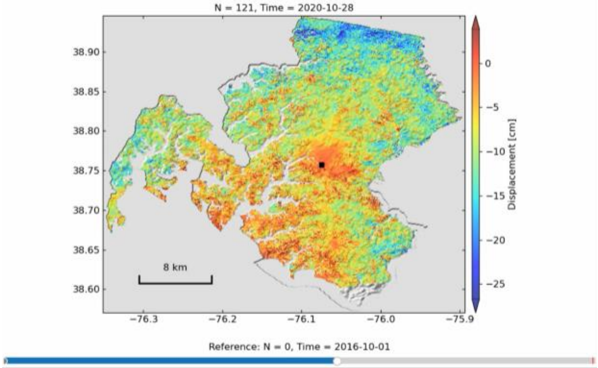
N = 121, Time = 2020-10-28
38.90
38.85
38.80
38.75
38.70
38.65
38.60
8 km
−76.3
−76.2
−76.1
−76.0
−75.9
0
−5
−10
−15
−20
−25
Displacement [cm]
Reference: N = 0, Time = 2016-10-01

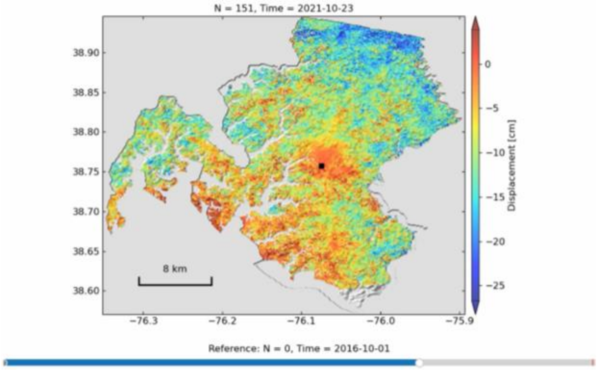
N = 151, Time = 2021-10-23
38.90
38.85
38.80
38.75
38.70
38.65
38.60
8 km
−76.3
−76.2
−76.1
−76.0
−75.9
0
−5
−10
−15
−20
−25
Displacement [cm]
Reference: N = 0, Time = 2016-10-01

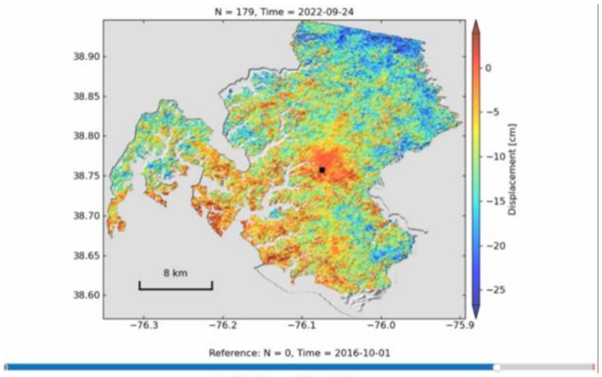

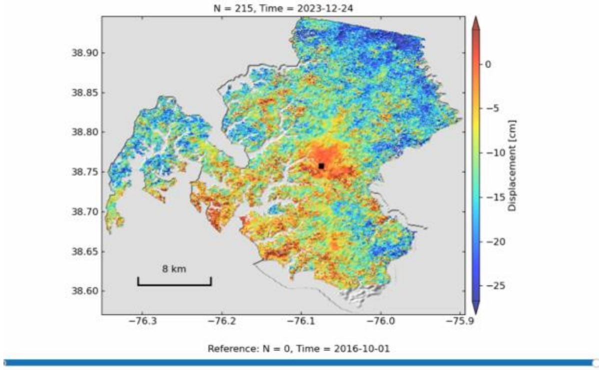

Montgomery County

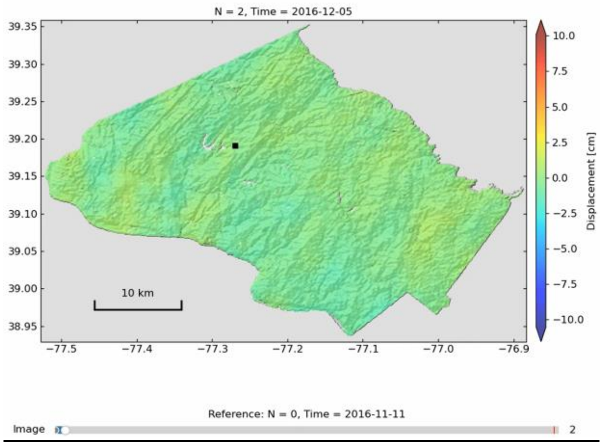

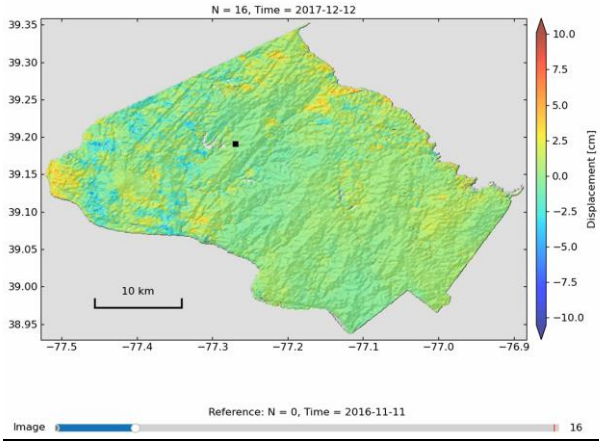

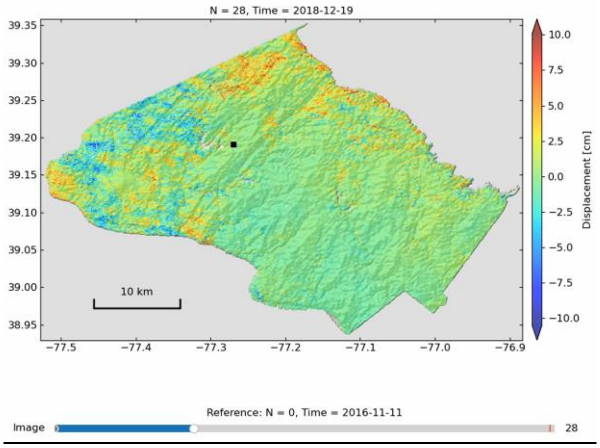
N = 28, Time = 2018-12-19
39.35
39.30
39.25
39.20
39.15
39.10
39.05
39.00
38.95
−77.5
−77.4
−77.3
−77.2
−77.1
−77.0
−76.9
10 km
10.0
7.5
5.0
2.5
0.0
−2.5
−5.0
−7.5
−10.0
Displacement [cm]
Reference: N = 0, Time = 2016-11-11
Image
28

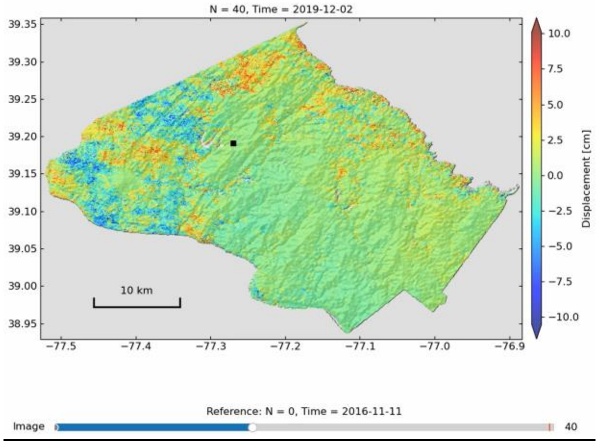
N = 40, Time = 2019-12-02
39.35
39.30
39.25
39.20
39.15
39.10
39.05
39.00
38.95
−77.5
−77.4
−77.3
−77.2
−77.1
−77.0
−76.9
10 km
10.0
7.5
5.0
2.5
0.0
−2.5
−5.0
−7.5
−10.0
Displacement [cm]
Reference: N = 0, Time = 2016-11-11
Image
40

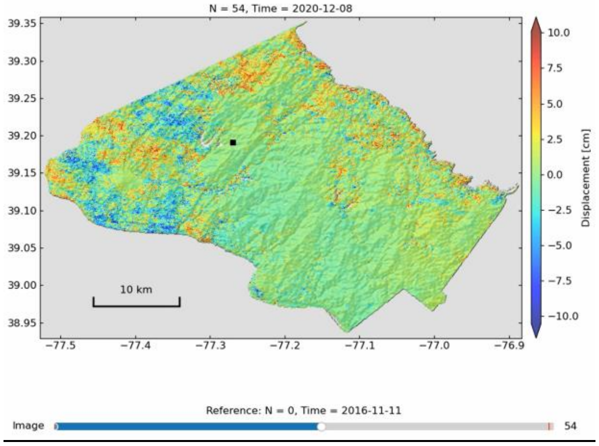
N = 54, Time = 2020-12-08
39.35
39.30
39.25
39.20
39.15
39.10
39.05
39.00
38.95
−77.5
−77.4
−77.3
−77.2
−77.1
−77.0
−76.9
10 km
10.0
7.5
5.0
2.5
0.0
−2.5
−5.0
−7.5
−10.0
Displacement [cm]
Reference: N = 0, Time = 2016-11-11
Image
54

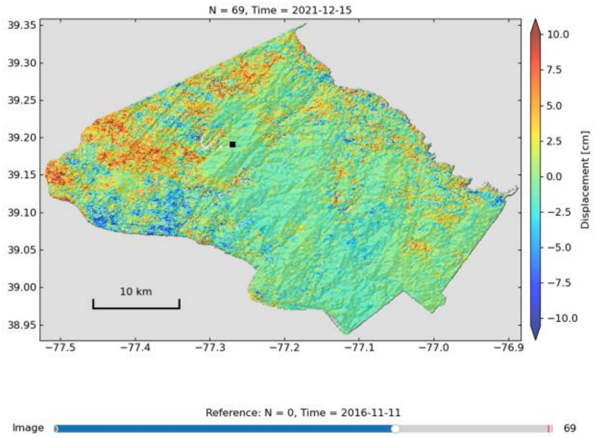
N = 69, Time = 2021-12-15
39.35
39.30
39.25
39.20
39.15
39.10
39.05
39.00
38.95
−77.5
−77.4
−77.3
−77.2
−77.1
−77.0
−76.9
10 km
10.0
7.5
5.0
2.5
0.0
−2.5
−5.0
−7.5
−10.0
Displacement [cm]
Reference: N = 0, Time = 2016-11-11
Image
69

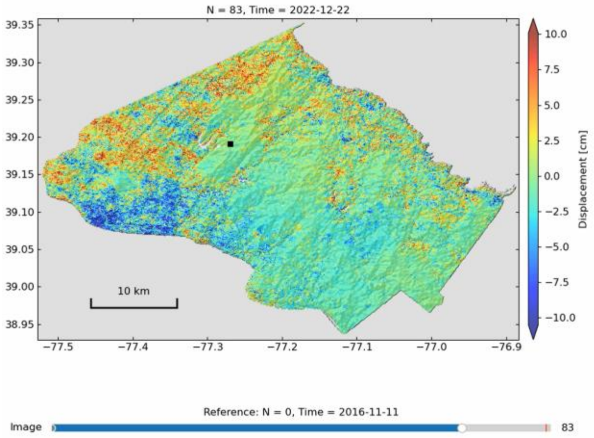
N = 83, Time = 2022-12-22
39.35
39.30
39.25
39.20
39.15
39.10
39.05
39.00
38.95
−77.5
−77.4
−77.3
−77.2
−77.1
−77.0
−76.9
10 km
10.0
7.5
5.0
2.5
0.0
−2.5
−5.0
−7.5
−10.0
Displacement [cm]
Reference: N = 0, Time = 2016-11-11
Image
83

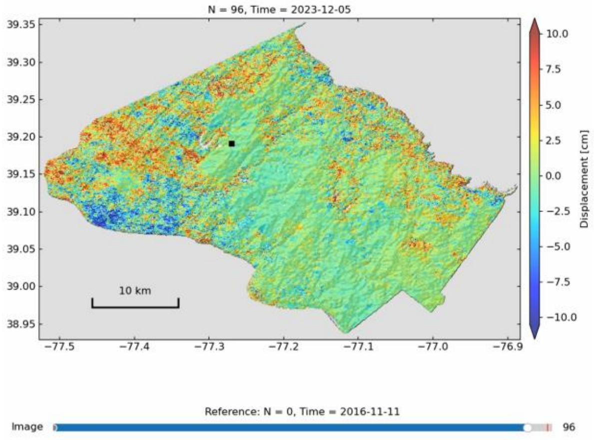
N = 96, Time = 2023-12-05
39.35
39.30
39.25
39.20
39.15
39.10
39.05
39.00
38.95
−77.5
−77.4
−77.3
−77.2
−77.1
−77.0
−76.9
10 km
10.0
7.5
5.0
2.5
0.0
−2.5
−5.0
−7.5
−10.0
Displacement [cm]
Reference: N = 0, Time = 2016-11-11
Image
96

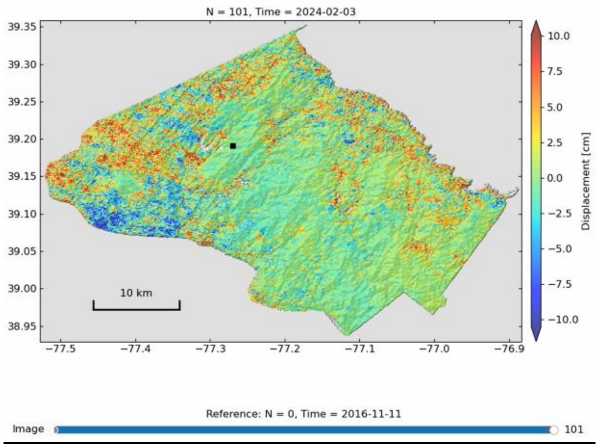

Baltimore County

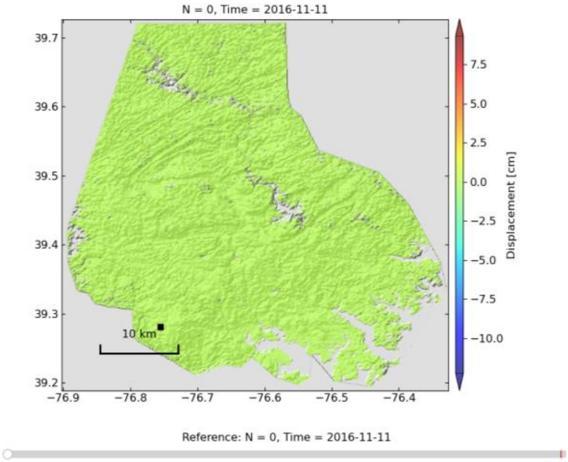

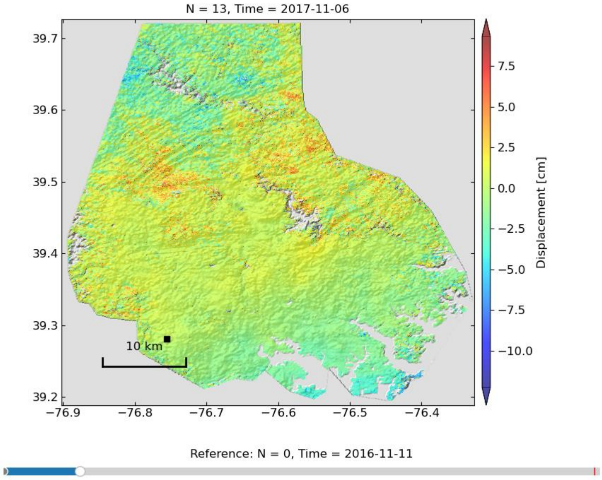

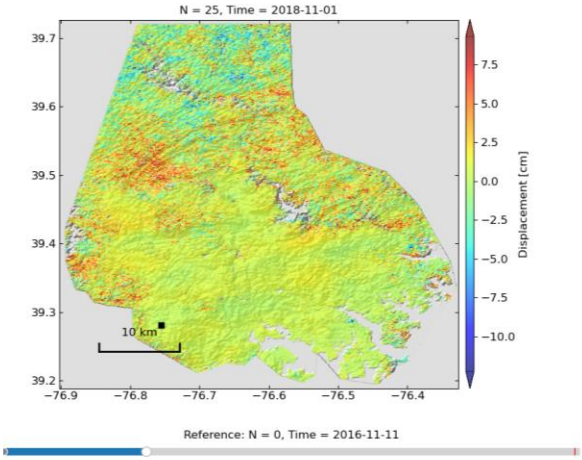
N = 25, Time = 2018-11-01
39.7
39.6
39.5
39.4
39.3
39.2
−76.9
−76.8
−76.7
−76.6
−76.5
−76.4
10 km
7.5
5.0
2.5
0.0
−2.5
−5.0
−7.5
−10.0
Displacement [cm]
Reference: N = 0, Time = 2016-11-11

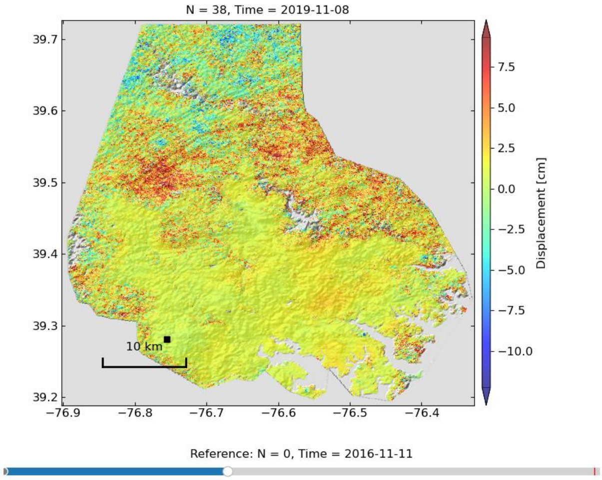
N = 38, Time = 2019-11-08
39.7
39.6
39.5
39.4
39.3
39.2
−76.9
−76.8
−76.7
−76.6
−76.5
−76.4
10 km
7.5
5.0
2.5
0.0
−2.5
−5.0
−7.5
−10.0
Displacement [cm]
Reference: N = 0, Time = 2016-11-11

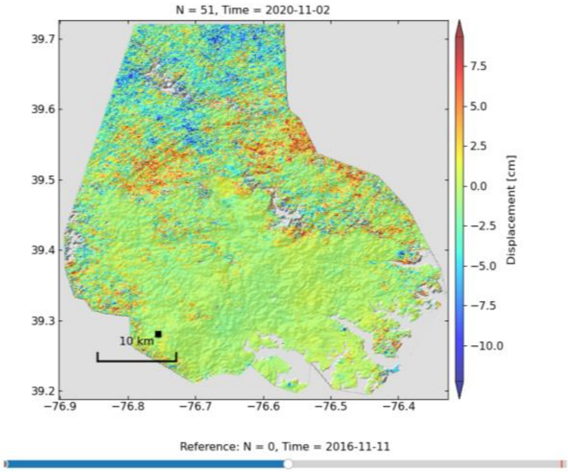
N = 51, Time = 2020-11-02
39.7
39.6
39.5
39.4
39.3
39.2
−76.9
−76.8
−76.7
−76.6
−76.5
−76.4
10 km
7.5
5.0
2.5
0.0
−2.5
−5.0
−7.5
−10.0
Displacement [cm]
Reference: N = 0, Time = 2016-11-11

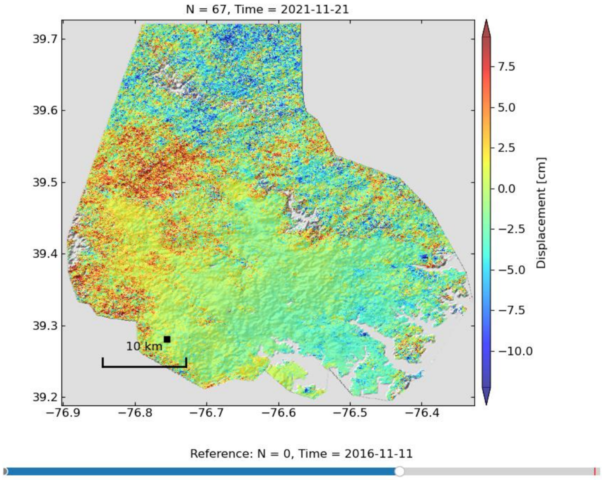
N = 67, Time = 2021-11-21
39.7
39.6
39.5
39.4
39.3
39.2
−76.9
−76.8
−76.7
−76.6
−76.5
−76.4
10 km
7.5
5.0
2.5
0.0
−2.5
−5.0
−7.5
−10.0
Displacement [cm]
Reference: N = 0, Time = 2016-11-11

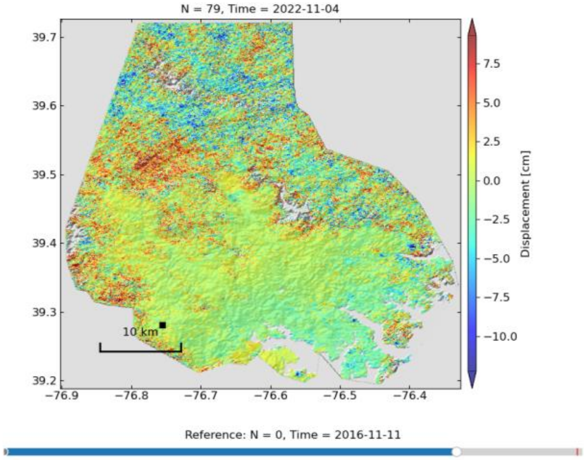
N = 79, Time = 2022-11-04
39.7
39.6
39.5
39.4
39.3
39.2
−76.9
−76.8
−76.7
−76.6
−76.5
−76.4
10 km
7.5
5.0
2.5
0.0
−2.5
−5.0
−7.5
−10.0
Displacement [cm]
Reference: N = 0, Time = 2016-11-11

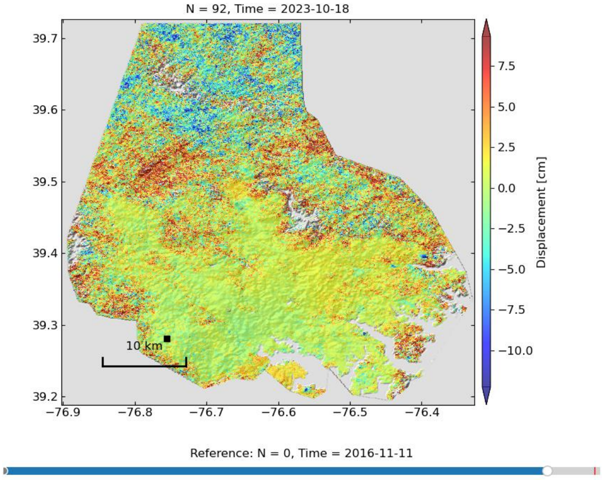
N = 92, Time = 2023-10-18
39.7
39.6
39.5
39.4
39.3
39.2
−76.9
−76.8
−76.7
−76.6
−76.5
−76.4
10 km
7.5
5.0
2.5
0.0
−2.5
−5.0
−7.5
−10.0
Displacement [cm]
Reference: N = 0, Time = 2016-11-11

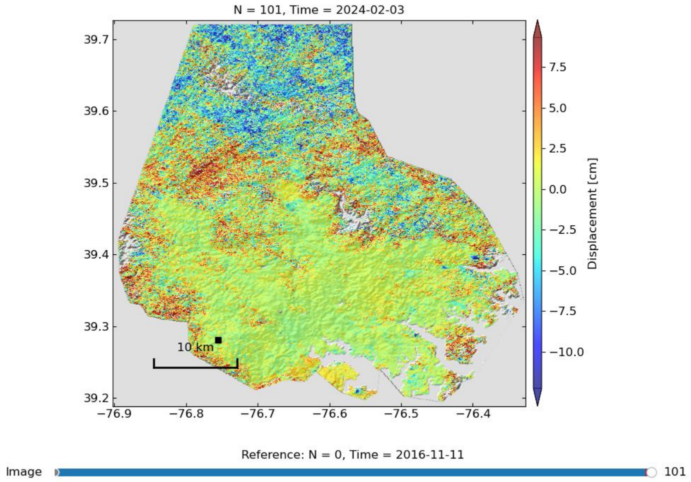
N = 101, Time = 2024-02-03
39.7
39.6
39.5
39.4
39.3
39.2
−76.9
−76.8
−76.7
−76.6
−76.5
−76.4
10 km
7.5
5.0
2.5
0.0
−2.5
−5.0
−7.5
−10.0
Displacement [cm]
Reference: N = 0, Time = 2016-11-11
Image
101

A2. LIDAR MAPS

Prince George County

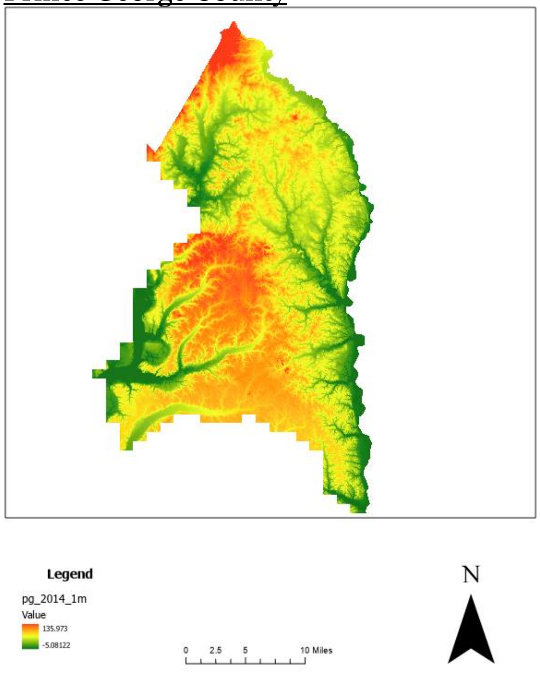

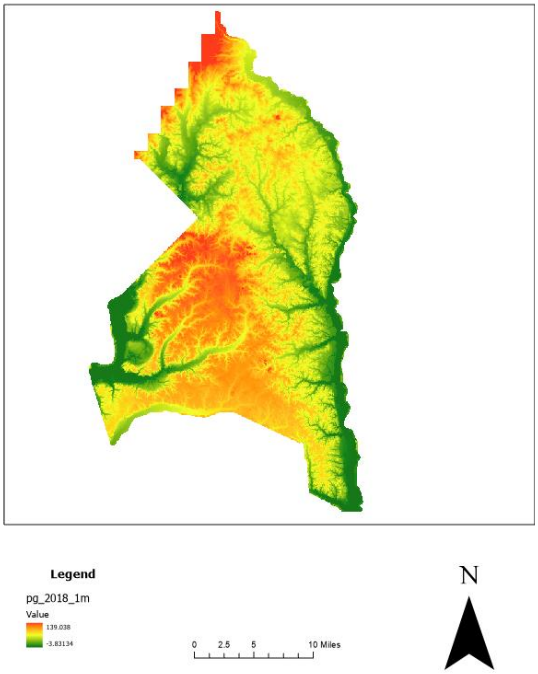

Worcester County

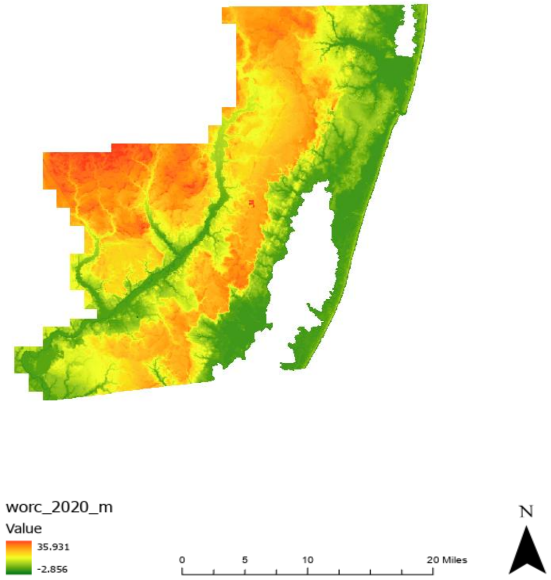

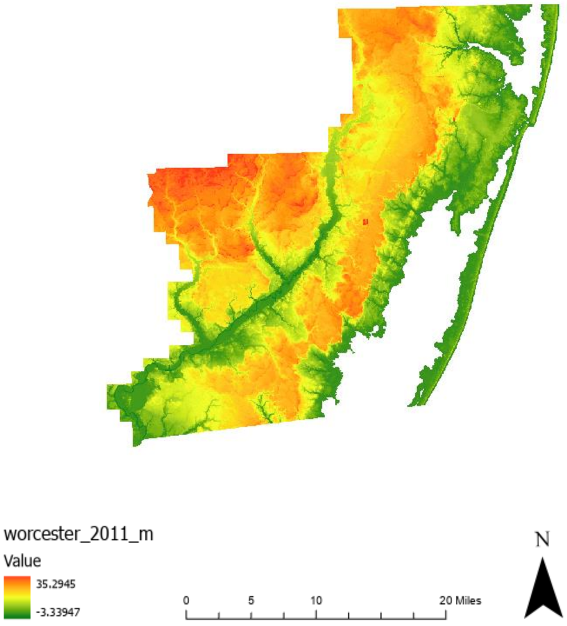

Wicomico County

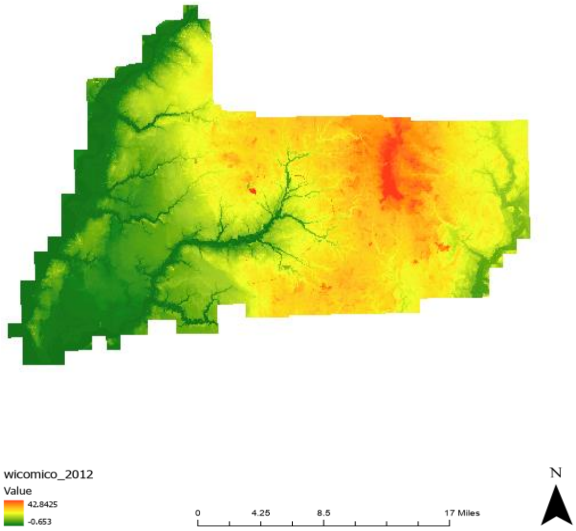

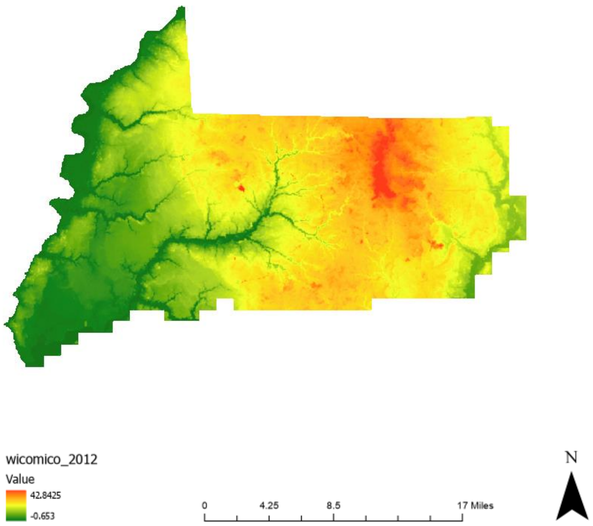

Somerset County

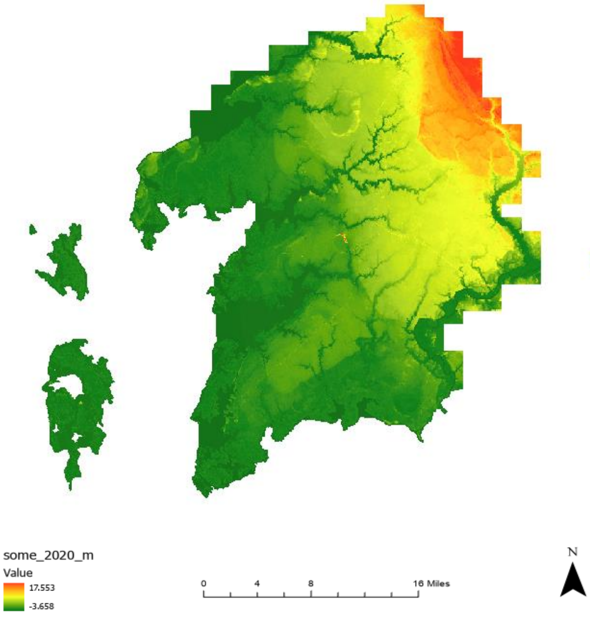

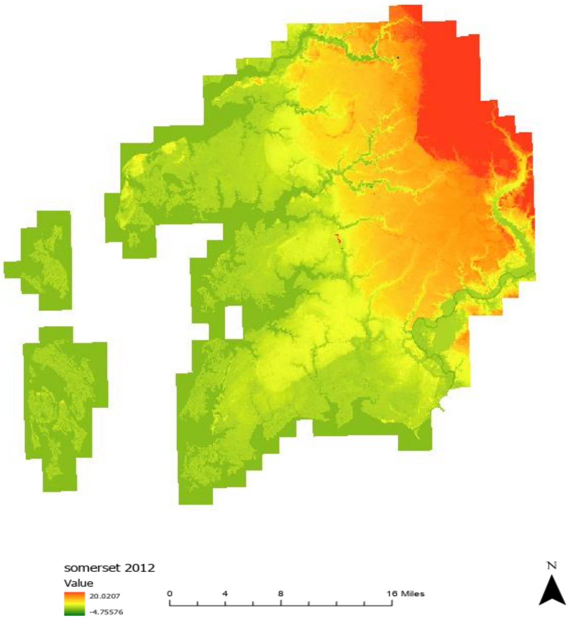

Talbot County

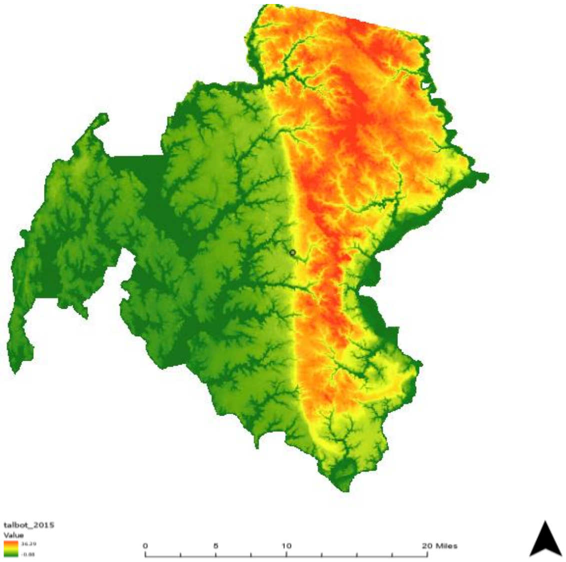

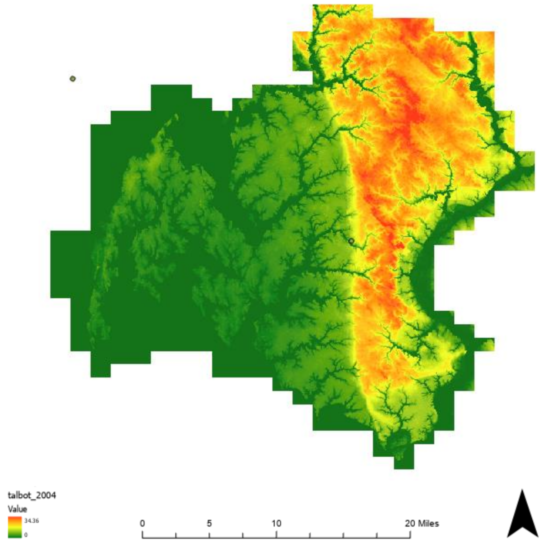

Harford County

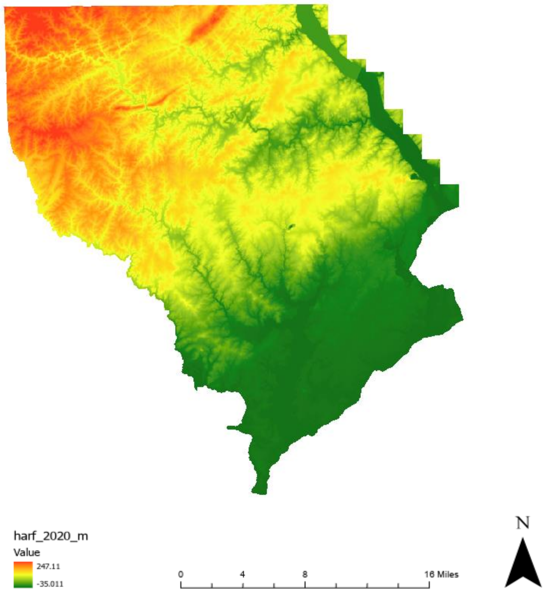

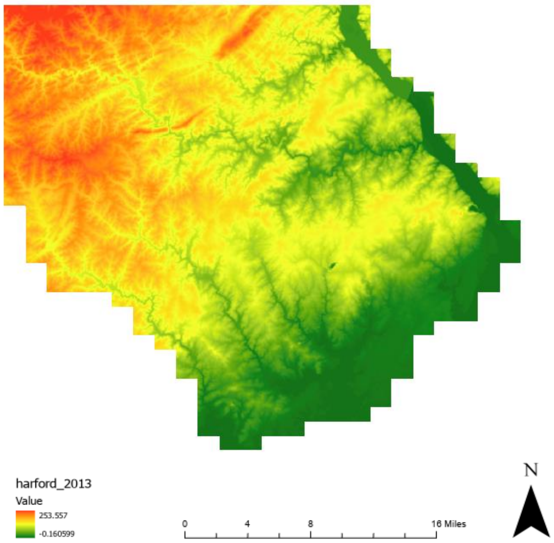

Howard County

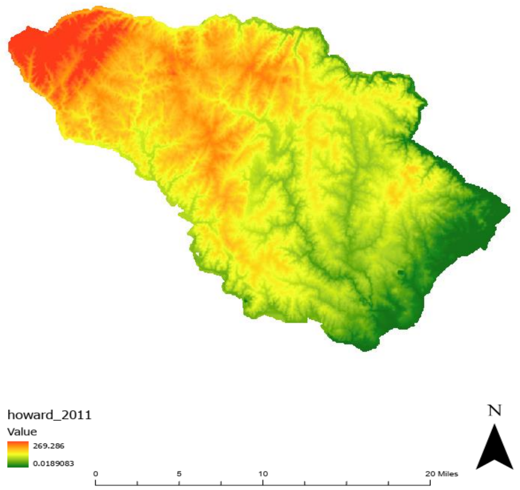
howard_2011
Value
269.286
0.0189083
0
5
10
20 Miles
N

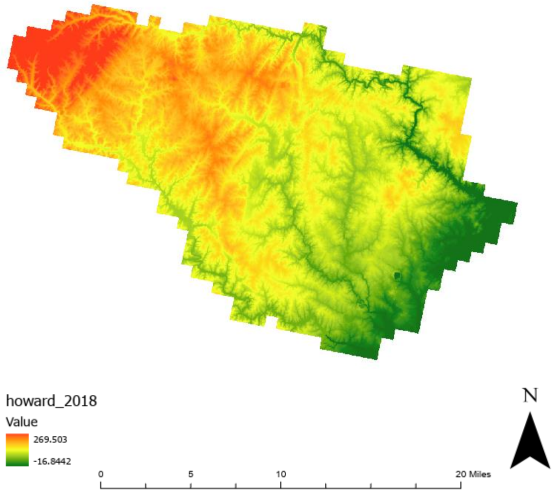
howard_2018
Value
269.503
-16.8442
0
5
10
20 Miles
N

<u>Kent County</u>

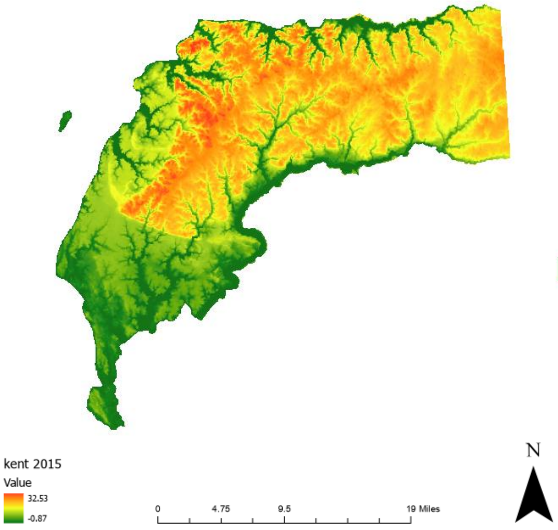
kent 2015
Value
32.53
-0.87
0
4.75
9.5
19 Miles
N

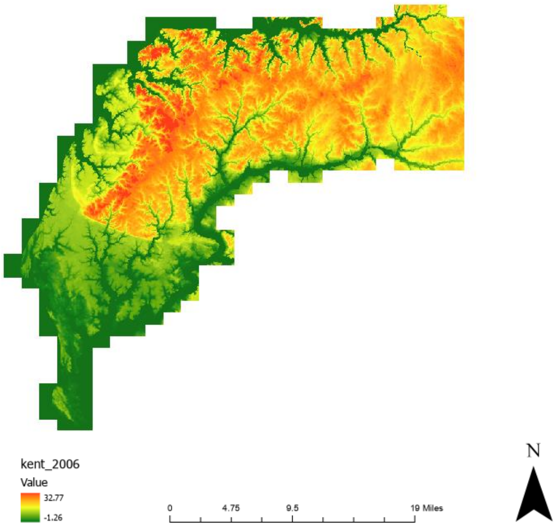
kent_2006
Value
32.77
-1.26
0
4.75
9.5
19 Miles
N

Garrett County

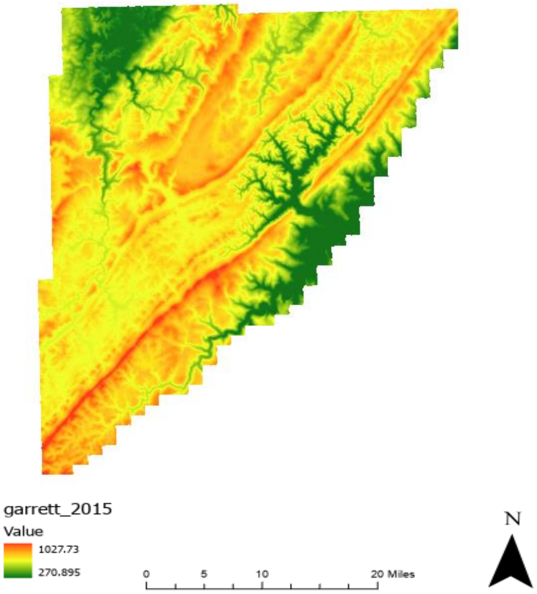

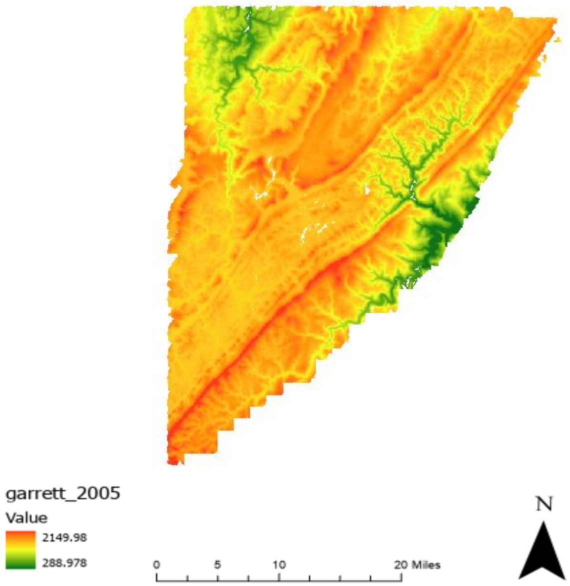

Caroline County

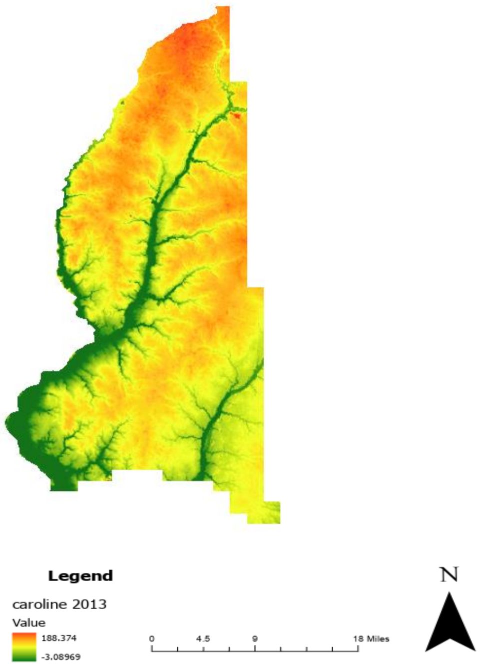

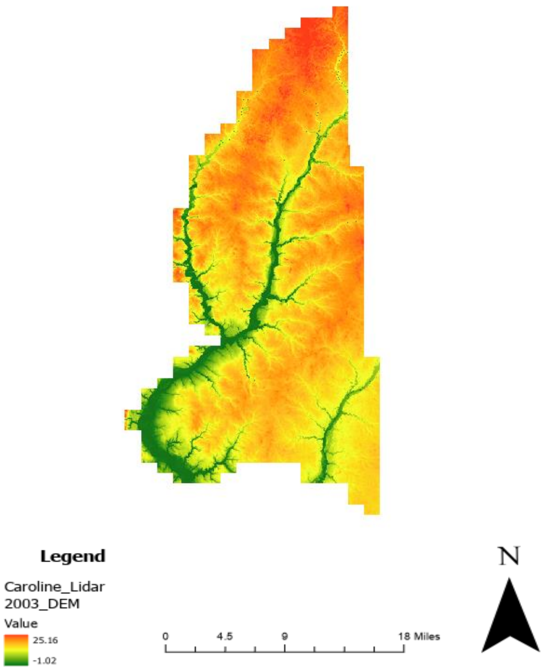

Dorchester County

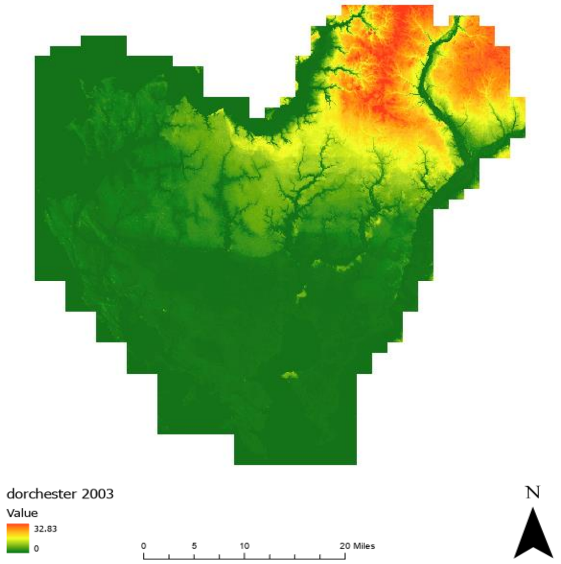

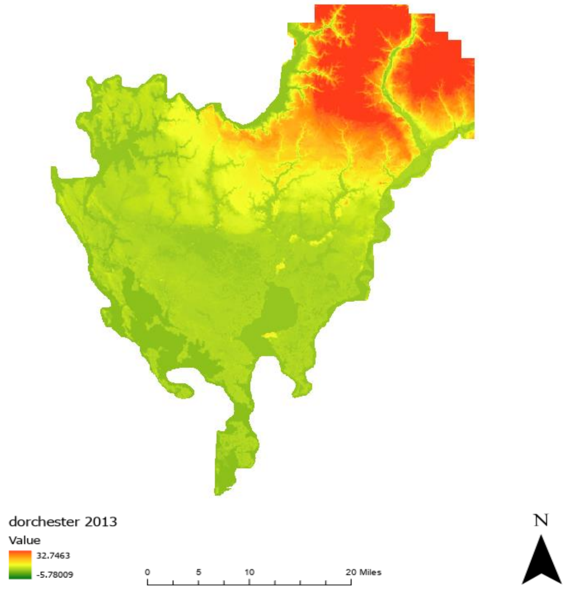

Charles County

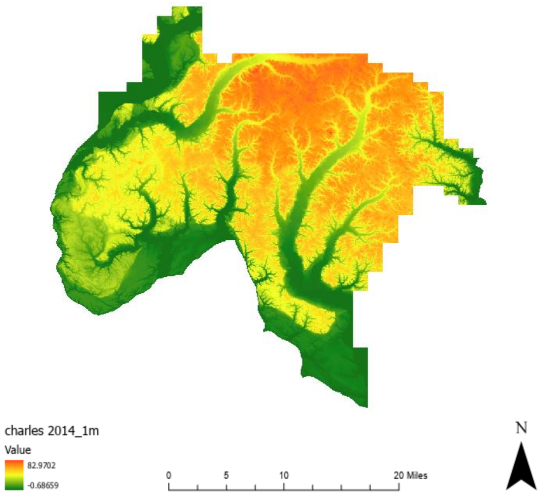

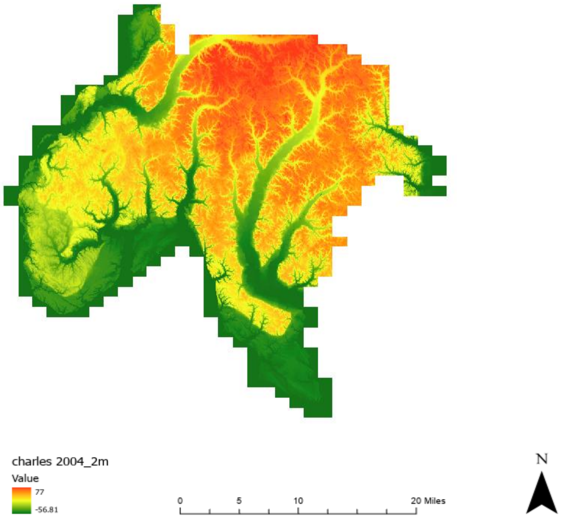

Calvert County

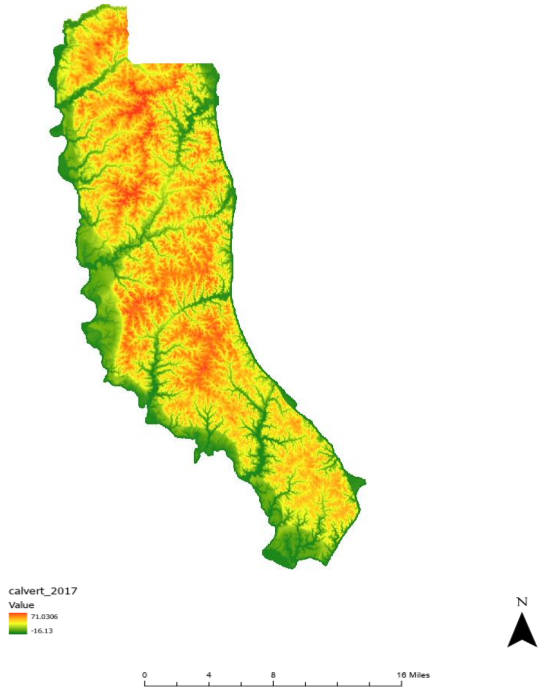

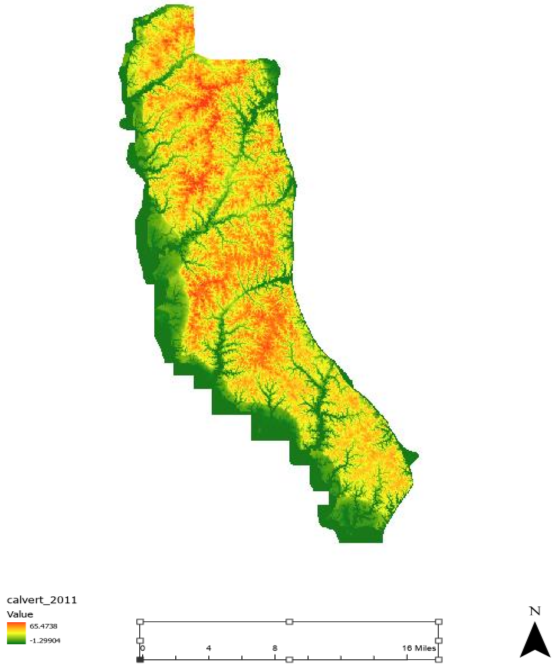

Cecil County

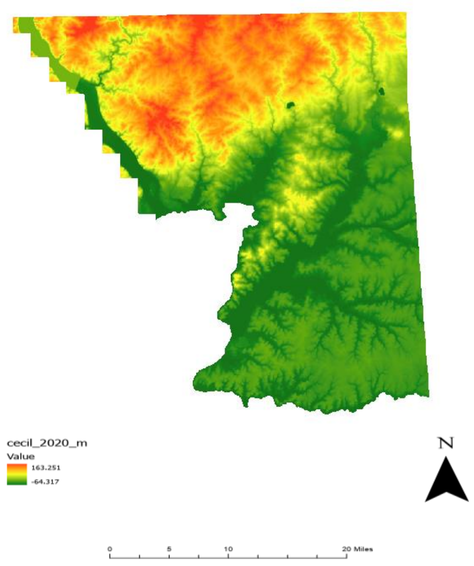

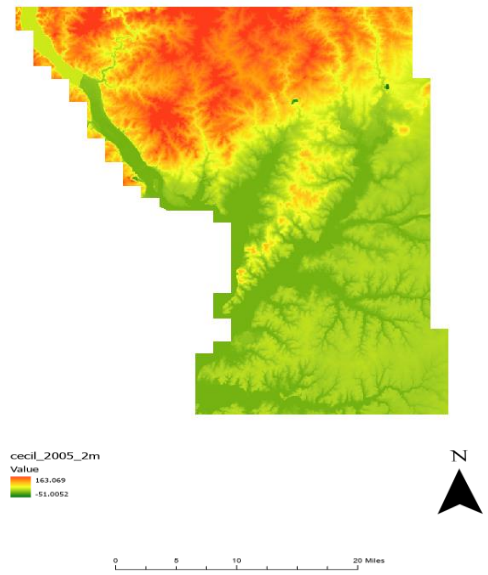

Carroll County

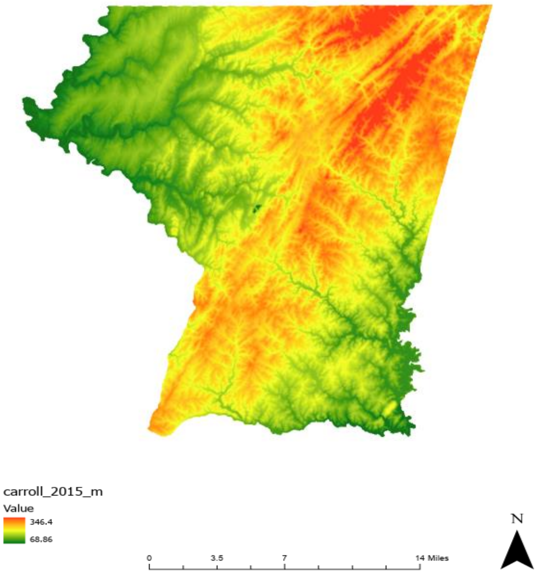

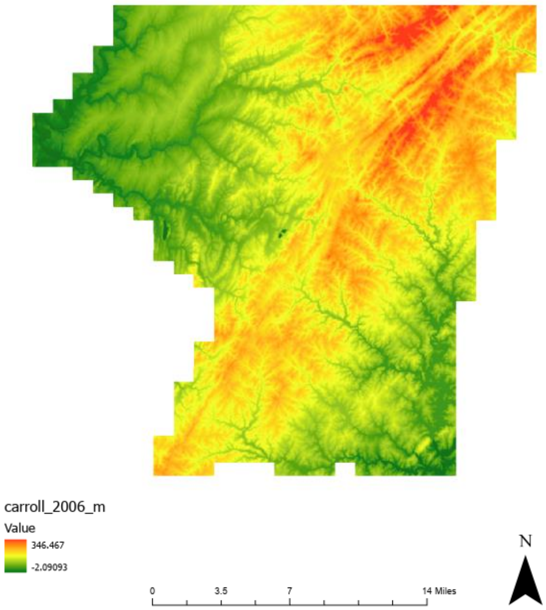

Appendix B

B: Physical Models

B.1 Guide to Performing a TRIGRS Model Run with Topographic DEM from Baltimore, Maryland

To perform a TRIGRS model run with a topographic DEM from Baltimore, Maryland, follow these steps to gather and prepare the data, set up the model, and run the analysis.

1. Obtain DEM Data

a) Download DEM Data:
b) Obtain DEM data for Baltimore, Maryland from sources like the USGS National Map or other online GIS data repositories. Example sources include: USGS Earth Explorer, NASA Earthdata, Maryland iMap
c) Select Area of Interest: Choose a specific area in Baltimore that is of interest for analysis. Download the DEM for that area.
d) Convert DEM Format:
e) Ensure the DEM file is in a compatible format for TRIGRS, such as GeoTIFF or ASCII Grid. Use GIS software like QGIS or ArcGIS to convert the DEM if it is in another format.

2. Prepare the DEM File

Clip and Reproject (if necessary):

a) Use GIS software to clip the DEM to your area of interest and reproject it to a coordinate system compatible with TRIGRS (e.g., UTM).
b) Format Conversion: Convert the DEM to the required format for TRIGRS if needed. TRIGRS often accepts ASCII Grid format, so you might need to convert your GeoTIFF to ASCII Grid.

3. Set Up TRIGRS Model

Example Setup:
Soil Properties (for demonstration):
Layer 1:
Cohesion (c): 15 kPa
Friction Angle (ϕ): 25°
Permeability (k): 5×10^{-6} m/s
Thickness: 2m
Layer 2:
Cohesion (c): 5 kPa
Friction Angle (ϕ): 30°
Permeability (k): 1×10^{-6} m/s
Thickness: 3m
Initial Moisture Content: 15% for both layers

Groundwater Data:
Initial Groundwater Table Depth: 5m below the surface
Groundwater Recharge Rate: 1×10^{-6} m/s (steady state)
Rainfall Data: 48-hour Event: 48mm of rain distributed 1mm per hour:

4. Run the TRIGRS Model

a) Load DEM:
b) Open TRIGRS and load the DEM file prepared. Ensure the DEM is correctly aligned with the model grid.
c) Input Soil Parameters:

i. Enter the soil properties for each layer in the TRIGRS setup.
ii. Set Groundwater Parameters:
iii.Input initial groundwater table depth and recharge rate.
iv. Input Rainfall Data:
v. Load the rainfall data into TRIGRS, specifying the temporal distribution.
vi. Configure Model Settings:

5. Define the model domain, boundary conditions, and simulation settings.

Run Simulation:
Start the simulation and monitor the process. Ensure it is complete without errors.

6. Analyze Results

Output Files:
Review output files for factors of safety, slip surface locations, and moisture distribution.
Visualization:
Use GIS software to visualize the results:
FS Map: Identify unstable zones (FS < 1.0).
Moisture Content Map: Show how moisture levels vary across the slope.
Groundwater Table Map: Display the groundwater table position.

<u>Example Execution with Hypothetical Data</u>

Assuming the DEM for Baltimore is ready and in ASCII Grid format, the following steps outline the execution process:
a) Open TRIGRS Software:
b) Load the DEM file into TRIGRS.
c) Configure Soil Layers:
d) Enter the properties for Layer 1 and Layer 2 as described.
e) Set Groundwater Parameters:
    Input groundwater table depth and recharge rate.
    Input Rainfall Data:
    Specify the 48-hour rainfall event.
f) Run Model:
g) Execute the simulation.
h) Review Outputs:
    Open results and visualize with GIS tools.

B2 TRIGRS Initialization File

```
# TRIGRS Initialization File
# Digital Elevation Model (DEM) file
elevation_file    elevation.asc
# Soil properties file
soil_properties_file soil_properties.txt
# Rainfall data file
rainfall_file     rainfall.txt
# Output directory
output_directory   ./output/
# Time step for the simulation (in hours)
time_step         1.0
# Total duration of the simulation (in hours)
simulation_duration 72.0
# Initial water table depth (in meters)
initial_wtd       2.0
# Initial pore-water pressure file (optional, can be set to NONE)
initial_pwp_file   NONE
# Saturated hydraulic conductivity (in meters per second)
hydraulic_conductivity 1e-6
# Soil density (in kg/m³)
soil_density      2000
# Soil cohesion (in Pascals)
soil_cohesion     10000
# Soil internal friction angle (in degrees)
soil_phi          30
# Maximum depth of the soil (in meters)
max_depth         10.0
# Maximum number of iterations for convergence
max_iterations     1000
# Convergence tolerance
convergence_tolerance 1e-6
# Flag to indicate if the model should account for evapotranspiration (YES/NO)
include_evapotranspiration NO
# Evapotranspiration rate (in mm/day, used if include_evapotranspiration is
YES)
evapotranspiration_rate 5.0
# Initial soil suction (in Pascals)
initial_soil_suction 1000
# Lateral boundary condition type (NOFLOW/FREE/DIRICHLET)
lateral_boundary_condition NOFLOW
# Flag to indicate if the model should use a dynamic water table (YES/NO)
use_dynamic_water_table YES
# Path to the Fortran executable file
executable_path    ./trigrs
```

Appendix C

C: Research Products for this Project

C.1 Conference Publications

1. Hosseinizadeh, A., Z. Sheng, S. Qian, Y. Liu, Separating infiltration and runoff from precipitation over Anacostia River watershed, Maryland, *Proc. Of World Environmental and Water Resources Conference*, ASCE, Milwaukee, WI, May 19-22, 2024.
2. Hosseinizadeh, A., Sheng, Z., Qian, S., Liu, Y. Slope instability forecasting system based on precipitation data. In 21st Annual Technical Forum on Geohazards, April 8-10, 2024 (oral presentation).
3. Hosseinizadeh, A, Qian,S., Gui,B. Liu, Y., Li, J. Sheng, Z., Owolabi, O., Olude, A., Fadipe, S., & Lamsal, S. Improve Highway Safety by reducing the Risks of Landslides, University Transportation Center –Safety 21 National Safety Summit, April 4, 2024, DC (poster presentation).
4. Hosseinizadeh, A., Fadipe, S., Qian, S. Gui, B., Liu, Y., Li, J., Sheng, Z. Incorporating precipitation data into geotechnical asset management – initial work, University Transportation Center –Safety 21 Deployment Partners Consortium Symposium, November 16, 2023, Pittsburgh, PA (poster presentation).

C.2 Datasets

Table C.2.1 Source data for the SWAT model

File Name	Detail	Format	Source and Link	Size
Ana_DEM_R	Topography map of Anacostia watershed cliped from DEM map of Maryland	.TIF	USGS website	532 KB
Ana_Soil	Soil type of Anacostia watershed cliped from Maryland soil map	.TIF	Maryland SSURGO	2.13 MB
MD-Landuse	The map of landuse and Land cover of Maryland	.Shp	Maryland Department of Planning (MDP)	140 MB
Northwest BR 2000-2023	Daily flow rate data of a gauge station (2000-2023)	.Txt	USGS website	276 KB
NASA Power larc cliamte data	Daily weather data (precipitation, temprature, solar radiation, humidity, wind speed)	.xlsx	NASA POWER website	846 KB
Merge_landslides	Including landslide inventories collected from SHA, USGS website, and NASA website	.Shp	merged data from SHA information, USGS, and NASA	1.26 MB

C.2.2 List of LiDAR data

Datasets for LiDAR

Sources: Maryland LiDAR data

https://imap.maryland.gov/pages/lidar-download

https://doitdataservices.maryland.gov/s/N9xGBYPKq4QSZNq

Table C2.2 List of LiDAR data

S/N	County	DEMs	Year
1	Prince George	0.9m	2014
		0.6m	2018
2	Montgomery	1.2m	2013
		0.6m	2018
3	Calvert	2m	2011
		0.3m	2017
4	Caroline	2m	2003
		1m	2013
5	Carroll	1m	2006
		0.7m	2015
6	Cecil	1m	2005
		1m	2020
7	Charles	2m	2004
		0.9m	2014
8	Dorchester	2m	2003
		0.9m	2013
9	Garrett	3m	2005
		1m	2015
10	Harford	1.5m	2013
		1m	2020
11	Howard	2m	2011
		0.6m	2018
12	Kent	2m	2006
		7m	2015
13	Montgomery	1.2m	2013
		0.6m	2018
14	Prince George	0.9m	2014
		0.32m	2020
15	Somerset	1m	2012
		1m	2020
16	Talbot	2m	2004
		0.7m	2015
17	Wicomico	1m	2012
		1m	2020

Table C2.3: Merged landslides

File Name	Detail	Format	Link
Merge_landslides	Including landslide inventories collected from SHA, USGS website, and NASA website	.Shp	merged data from SHA information, USGS, and NASA

C.2.3 List of InSAR data

Title of Dataset: InSAR Analysis Data

Date of data collection: Data was obtained and stored online at the Alaska Satellite Facility from 2024-06-28 to 2024-07-16.

Geographic location of data collection: Maryland, United States

To retrieve data, follow these steps:

1. Create a free Earthdata Login account at https://urs.earthdata.nasa.gov/home.
2. Go to Vertex (https://search.asf.alaska.edu) and log in using your Earthdata Login username and password.
3. Define the search type as "Geographic Search".
4. Define the dataset as "Sentinel-1".

<Repeat steps 2 to 4 for each county.>

5. Define the "Area of Interest" by either creating a polygon or a zip file delimiting Allegany, Talbot, Montgomery, and Baltimore Counties.
6. From the resulting search list, select a reference scene. <Refer to the list below for the date range and baseline tolerances applied for each county.>
7. Once selected, perform the Small Baseline Subset (SBAS) acquisition by clicking the "SBAS Tool" button. This will launch the search.
8. Refine the SBAS Results by clicking the "SBAS Criteria" button to set a date range and adjust baseline tolerances. <Refer to the list below for the date range and baselines applied for each county.>
9. Set the Overlap Threshold to 50%.
10. Once the search results are updated, <ensure the resulting list matches the list below for each county>. Add all pairs to the On-Demand Queue by clicking the On Demand icon at the top of the list and selecting "InSAR GAMMA" and "Add 3 SLC pairs".
11. Click the large "On Demand" icon and select "On Demand Queue" from the list of options.

12. Set InSAR Options by clicking "Set MintPy Options" and applying the "Water Mask".
13. Once you’re ready to submit the jobs for processing, click the "Submit Jobs" button.
14. Add a Project Name.
15. Once the project is completed, it will be recognized when importing into MintPy Software to perform the Time Series Analysis.

DATA & FILE OVERVIEW

Allegany County

>Reference Scene:
S1A_IW_SLC__1SDV_20180802T231527_20180802T231554_023074_028154_B7AF
>Date range: January 2016 to April 2024
>Baseline tolerances:24 days, 200 meters.
>List of Pairs: 375

Talbot County
>Reference Scene:
S1A_IW_SLC__1SDV_20231118T225909_20231118T225936_051278_062FC2_6604
>Date range: January 2016 to April 2024
>Baseline tolerances:24 days, 200 meters.
>List of Pairs: 426

Montgomery and Baltimore Counties
>Reference Scene:
S1A_IW_SLC__1SDV_20190217T230704_20190217T230731_025976_02E4D4_4AA2
>Date range: From 2016 to 2024, Season: 01 October to 28 February
>Baseline tolerances:30 days, 150 meters.
>List of Pairs: 158

C.3 Workshop

1. 2024 Summer Workshop: Improve Highway Safety by Reducing the Risks of Landslides with Smart Warning Systems, June 21, 2024

Bibliography

1. Schuster, R. L., Highland, L. M., & Survey, U. S. G. (2001). *Socioeconomic and environmental impacts of landslides in the western hemisphere*. U.S. Geological Survey Editorial. August, 2001.
2. Petley, D. (2012). Global patterns of loss of life from landslides. *Geology*, 40, 927–930. https://doi.org/10.1130/G33217.1
3. Froude, M. J., & Petley, D. N. Global fatal landslide occurrence from 2004 to 2016. *Natural Hazards and Earth System Sciences*, 2020 18, 2161–2181. https://doi.org/10.5194/nhess-18-2161-2018
4. Petley, D. N., Dunning, S., & Rosser, N. The analysis of global landslide risk through the creation of a database of worldwide landslide fatalities. In *Landslide risk management, 2005,* 367–374. Balkema. https://doi.org/10.1201/9781439833711-18
5. Kirschbaum, D. B., Stanley, T., & Zhou, Y. Spatial and temporal analysis of a global landslide catalog.*Geomorphology*, 2015, 249, 4–15. https://doi.org/10.1016/j.geomorph.2015.03.016
6. Sidle, R. C., & Ochiai, H. Natural factors influencing landslides. In *Landslides: Processes, prediction, and land use* (Water Resources, 2006, 41–119. American Geophysical Union.
7. Terzaghi, K. Mechanism of landslides. In S. Paige (Ed.), *Application of geology to engineering practice*. 1950, Geological Society of America.
8. Huang, J., Wu, X., Ling, S. et al. A bibliometric and content analysis of research trends on GIS-based landslide susceptibility from 2001 to 2020. *Environ Sci Pollut Res.*, 2022, 29, 86954–86993. https://doi.org/10.1007/s11356-022-23732-z.
9. Maryland Department of Transportation/State Highway Administration. MDOT SHA GEOTECHNICAL Asset Management Plan. 2022.
10. “Landslides.” World Health Organization, World Health Organization, www.who.int/health-topics/landslides#tab=tab_1. Accessed 17 July 2024.
11. National Oceanic and Atmospheric Administration (NOAA). What is lidar? [Online]. Available at: https://oceanservice.noaa.gov/facts/lidar.html 2023, (Accessed: 30 July 2024).
12. Helz, R.L. Monitoring ground deformation from space. Reston, VA, USA: US Department of the Interior, US Geological Survey, 2005.
13. Jaboyedoff, M., Oppikofer, T., Abellán, A., Derron, M.H., Loye, A., Metzger, R. and Pedrazzini, A., Use of LIDAR in landslide investigations: a review. Natural hazards, 2012, 61, 5-28.
14. Schulz, W.H. Landslide susceptibility revealed by LIDAR imagery and historical records, Seattle, Washington. Engineering Geology, 2007, 89(1-2), 67-87.

15. Abellán, A., Oppikofer, T., Jaboyedoff, M., Rosser, N.J., Lim, M. and Lato, M.J., Terrestrial laser scanning of rock slope instabilities. Earth surface processes and landforms, 2014, 39(1), 80-97.
16. Colesanti, C. and Wasowski, J., Investigating landslides with space-borne Synthetic Aperture Radar (SAR) interferometry. Engineering geology, 2006, 88(3-4), 173-199.
17. Cascini, L., Fornaro, G. and Peduto, D. Advanced low-and full-resolution DInSAR map generation for slow-moving landslide analysis at different scales. Engineering Geology, 2010, 112(1-4), 29-42.
18. Ferretti, A., Prati, C. and Rocca, F., Permanent scatterers in SAR interferometry. IEEE Transactions on geoscience and remote sensing, 2001, 39(1), 8-20.
19. Mohammed, O.I., Saeidi, V., Pradhan, B. and Yusuf, Y.A., Advanced differential interferometry synthetic aperture radar techniques for deformation monitoring: a review on sensors and recent research development. Geocarto International, 2014, 29(5), 536-553.
20. Berardino, P., Fornaro, G., Lanari, R. and Sansosti, E. A new algorithm for surface deformation monitoring based on small baseline differential SAR interferograms. IEEE Transactions on geoscience and remote sensing, 2002, 40(11), 2375-2383.
21. Li, S., Xu, W. and Li, Z., Review of the SBAS InSAR Time-series algorithms, applications, and challenges. Geodesy and Geodynamics, 2022, 13(2), 114-126.
22. Zhong, W., Chu, T., Tissot, P., Wu, Z., Chen, J. and Zhang, H. Integrated coastal subsidence analysis using InSAR, LiDAR, and land cover data. Remote Sensing of Environment, 2022, 282, 113297.
23. Zhang, Y., Meng, X., Jordan, C., Novellino, A., Dijkstra, T. and Chen, G., 2018. Investigating slow-moving landslides in the Zhouqu region of China using InSAR time series. Landslides, 2018, 15, 1299-1315.
24. Cigna, F., Esquivel Ramírez, R. and Tapete, D., 2021. Accuracy of Sentinel-1 PSI and SBAS InSAR displacement velocities against GNSS and geodetic leveling monitoring data. Remote Sensing, 2021, 13(23), 4800.
25. Ohenhen, L.O., Shirzaei, M. and Barnard, P.L., Slowly but surely: Exposure of communities and infrastructure to subsidence on the US east coast. PNAS nexus, 2024, 3(1), 426.
26. Razak, K.A., Santangelo, M., Van Westen, C.J., Straatsma, M.W. and de Jong, S.M., Generating an optimal DTM from airborne laser scanning data for landslide mapping in a tropical forest environment. Geomorphology, 2013, 190, 112-125.
27. Intrieri, E., Raspini, F., Fumagalli, A., Lu, P., Del Conte, S., Farina, P., Allievi, J., Ferretti, A. and Casagli, N. The Maoxian landslide as seen from space: detecting precursors of failure with Sentinel-1 data. Landslides, 2018, 15, 123-133.
28. Bianchini, S., Ciampalini, A., Raspini, F., Bardi, F., Di Traglia, F., Moretti, S. and Casagli, N. Multi-temporal evaluation of landslide movements and

impacts on buildings in San Fratello (Italy) by means of C-band and X-band PSI data. Pure and Applied Geophysics, 2015, 172, 3043-3065.

29. Lu, Z. and Kim, J.. A framework for studying hydrology-driven landslide hazards in northwestern US using satellite InSAR, precipitation and soil moisture observations: Early results and future directions. GeoHazards, 2021, 2(2), 17-40.
30. Yunjun, Z., Fattahi, H. and Amelung, F. Small baseline InSAR time series analysis: Unwrapping error correction and noise reduction. Computers & Geosciences, 2019, 133, 104331.
31. Emberson, R., Kirschbaum, D., & Stanley, T. New global characterisation of landslide exposure. *Natural Hazards and Earth System Sciences*, 2020. 20(12), 3413-3424.
32. Froude, M. J., & Petley, D. N. Global fatal landslide occurrence from 2004 to 2016. Natural Hazards and Earth System Sciences, 2018. 18(8), 2161-2181.
33. Paerl, H. W., Hall, N. S., Hounshell, A. G., Rossignol, K. L., Barnard, M. A., Luettich, R. A., ... & Harding, L. W. Recent increases of rainfall and flooding from tropical cyclones (TCs) in North Carolina (USA): implications for organic matter and nutrient cycling in coastal watersheds. Biogeochemistry, 2020. 150, 197-216.
34. Rahardjo, H., Nistor, M. M., Gofar, N., Satyanaga, A., Xiaosheng, Q., & Chui Yee, S. I. Spatial distribution, variation and trend of five-day antecedent rainfall in Singapore. Georisk: Assessment and Management of Risk for Engineered Systems and Geohazards, 2020. 14(3), 177-191.
35. Cevasco, A., Pepe, G., & Brandolini, P. (2014). The influences of geological and land use settings on shallow landslides triggered by an intense rainfall event in a coastal terraced environment. Bulletin of Engineering Geology and the Environment, 2014. 73, 859-875.
36. Glade, T., Anderson, M. G., & Crozier, M. J. (Eds.). Landslide hazard and risk (Vol. 807). Chichester: Wiley. 2005.
37. Zêzere, J. L., Trigo, R. M., & Trigo, I. F. Shallow and deep landslides induced by rainfall in the Lisbon region (Portugal): assessment of relationships with the North Atlantic Oscillation. Natural Hazards and Earth System Sciences, 2005. 5(3), 331-344.
38. Özçelik, F. V., & Selçuk, M. E. Parametric Analysis of Factors that Affects the Rainfall Induced Slope Stability. Turkish Journal of Geosciences, 2022. 3(2), 49-57.
39. Wu, L., & Zhou, J. Rainfall Infiltration in Unsaturated Soil Slope Failure (p. 130). Springer Nature. 2023.
40. Zhang, L., Wu, F., Zhang, H., Zhang, L., & Zhang, J. Influences of internal erosion on infiltration and slope stability. Bulletin of Engineering Geology and the Environment, 2019. 78, 1815-1827.
41. Liu, Q., Su, L., Zhang, C., Hu, B., & Xiao, S. Dynamic variations of interception loss-infiltration-runoff in three land-use types and their influence on slope stability: An example from the eastern margin of the Tibetan Plateau. Journal of Hydrology, 2022. 612, 128218.

42. Tung, Y. K., Zhang, H., Ng, C. W. W., & Kwok, Y. F. Transient seepage analysis of rainfall infiltration using a new conjunctive surface-subsurface flow model. In Proceedings of the 57th Canadian Geotechnical Conference and the 5th Joint CGS-IAH Conference, 2004. 7, 17-22.
43. Chen, R. H., Chen, H. P., Chen, K. S., & Zhung, H. B. Simulation of a slope failure induced by rainfall infiltration. *Environmental Geology*, 2009. 58, 943-952.
44. Mukhlisin, M., & Taha, M. R. Numerical model of antecedent rainfall effect on slope stability at a hillslope of weathered granitic soil formation. Journal of the Geological Society of India, 2012. 79, 525-531.
45. Zhang, J., Huang, H. W., Zhang, L. M., Zhu, H. H., & Shi, B. Probabilistic prediction of rainfall-induced slope failure using a mechanics-based model. Engineering Geology, 2014. 168, 129-140.
46. He, W., Ishikawa, T., & Yulong, Z. H. U. Wide/narrow-area slope stability analysis considering infiltration and runoff during heavy precipitation. Soils and Foundations, 2023. 63(1), 101248.
47. Belhadj, N., Joannis, C., & Raimbault, G. Modelling of rainfall induced infiltration into separate sewerage. Water Science and Technology, 1995. 32(1), 161-168.
48. Chu, X., & Mariño, M. A. Determination of ponding condition and infiltration into layered soils under unsteady rainfall. Journal of Hydrology, 2005. 313(3-4), 195-207.
49. Ebel, B. A. Temporal evolution of measured and simulated infiltration following wildfire in the Colorado Front Range, USA: Shifting thresholds of runoff generation and hydrologic hazards. Journal of Hydrology, 2020. 585, 124765.
50. Hawkins, R. H., & Cundy, T. W. Steady-state analysis of infiltration and overland flow for spatially-varied hillslopes 1. JAWRA Journal of the American Water Resources Association, 1987. 23(2), 251-256.
51. Jain, A., Sudheer, K. P., & Srinivasulu, S. Identification of physical processes inherent in artificial neural network rainfall runoff models. Hydrological processes, 2004. 18(3), 571-581.
52. Mardhel, V., Pinson, S., & Allier, D. Description of an indirect method (IDPR) to determine spatial distribution of infiltration and runoff and its hydrogeological applications to the French territory. Journal of Hydrology, 2021. 592, 125609.
53. Qi, J., Lee, S., Zhang, X., Yang, Q., McCarty, G. W., & Moglen, G. E. Effects of surface runoff and infiltration partition methods on hydrological modeling: A comparison of four schemes in two watersheds in the Northeastern US. Journal of Hydrology, 2020. 581, 124415.
54. Cho, S. E., & Lee, S. R. Evaluation of surficial stability for homogeneous slopes considering rainfall characteristics. Journal of Geotechnical and Geoenvironmental Engineering, 2002. 128(9), 756-763.
55. Chleborad, A. F., Baum, R. L., & Godt, J. W. Rainfall thresholds for forecasting landslides in the Seattle, Washington, area: Exceedance and probability. US Geological Survey Open-File Report, 2006. 1064, 31.

56. Godt, J. W., Baum, R. L., & Chleborad, A. F. Rainfall characteristics for shallow landsliding in Seattle, Washington, USA. Earth Surface Processes and Landforms: The Journal of the British Geomorphological Research Group, 2006. 31(1), 97-110.
57. Guzzetti, F., Peruccacci, S., Rossi, M., & Stark, C. P. The rainfall intensity–duration control of shallow landslides and debris flows: an update. Landslides, 2008. 5, 3-17.
58. Aydilek, A., & Ramanathan, R. S. Slope failure investigation management system (No. MD-13-SP009B4N). Maryland. State Highway Administration. Office of Policy & Research. 2013.
59. Pennington, C., Dijkstra, T., Lark, M., Dashwood, C., Harrison, A., & Freeborough, K. Antecedent precipitation as a potential proxy for landslide incidence in South West United Kingdom. In Landslide Science for a Safer Geoenvironment: Vol. 1: The International Programme on Landslides (IPL) (pp. 253-259). Springer International Publishing. 2014.
60. Ramanathan, R., Aydilek, A. H., & Tanyu, B. F. Development of a GIS-based failure investigation system for highway soil slopes. Frontiers of Earth Science, 2015. 9, 165-178.
61. Lee, W. Y., Park, S. K., & Sung, H. H. The optimal rainfall thresholds and probabilistic rainfall conditions for a landslide early warning system for Chuncheon, Republic of Korea. Landslides, 2021. 18, 1721-1739.
62. Bezak, N., & Mikoš, M. Changes in the rainfall event characteristics above the empirical global rainfall thresholds for landslide initiation at the pan-European level. Landslides, 2021. 18(5), 1859-1873.
63. Abraham, M. T., Satyam, N., Rosi, A., Pradhan, B., & Segoni, S. Usage of antecedent soil moisture for improving the performance of rainfall thresholds for landslide early warning. Catena, 2021. 200, 105147.
64. Chiu, Y. Y., Chen, H. E., & Yeh, K. C. Investigation of the influence of rainfall runoff on shallow landslides in unsaturated soil using a mathematical model. Water, 2019. 11(6), 1178.
65. Dolojan, N. L. J., Moriguchi, S., Hashimoto, M., & Terada, K. Mapping method of rainfall-induced landslide hazards by infiltration and slope stability analysis: A case study in Marumori, Miyagi, Japan, during the October 2019 Typhoon Hagibis. Landslides, 2021. 18, 2039-2057.
66. Chansorn, R., Chotpantarat, S., & Klongvessa, P. Hydrological model of landslide risk in Huai Nam Phung subbasin, Thailand. Bulletin of Engineering Geology and the Environment, 2023. 82(4), 140.
67. Cui, H., Ji, J., Hürlimann, M., & Medina, V. Probabilistic and physically-based modelling of rainfall-induced landslide susceptibility using integrated GIS-FORM algorithm. Landslides, 2024. 21(6), 1461-1481.
68. Devereux, O. H., Prestegaard, K. L., Needelman, B. A., & Gellis, A. C. Suspended-sediment sources in an urban watershed, Northeast Branch Anacostia River, Maryland. Hydrological Processes: An International Journal, 2010. 24(11), 1391-1403.
69. Warner, A., Shepp, D., Corish, K., & Galli, J. An existing source assessment of pollutants to the Anacostia watershed (No. 98708). 1997.

70. Hwang, H. M., & Foster, G. D. Characterization of polycyclic aromatic hydrocarbons in urban stormwater runoff flowing into the tidal Anacostia River, Washington, DC, USA. Environmental Pollution, 2006. 140(3), 416-426.
71. Hosni, A. A., Pauzi, N. I. M., & Shariffuddin, A. S. Geotechnical properties of waste soil from closed construction dumping area in Serdang, Selangor, Malaysia. Elect. J. Geotech. Eng.(EJGE), 2015. 17, 2015.
72. Williams, J. R., Arnold, J. G., Kiniry, J. R., Gassman, P. W., & Green, C. H. History of model development at Temple, Texas. Hydrological sciences journal, 2008. 53(5), 948-960.
73. Gassman, P. W., Sadeghi, A. M., & Srinivasan, R. Applications of the SWAT model special section: overview and insights. Journal of Environmental Quality, 2014. 43(1), 1-8.
74. Gassman, P. W., Reyes, M. R., Green, C. H., & Arnold, J. G. The soil and water assessment tool: historical development, applications, and future research directions. Transactions of the ASABE, 2007. 50(4), 1211-1250.
75. Akoko, G., Le, T. H., Gomi, T., & Kato, T. A review of SWAT model application in Africa. Water, 2021. 13(9), 1313.
76. Neitsch, S. L., Arnold, J. G., Kiniry, J. R., & Williams, J. R. Soil and water assessment tool theoretical documentation version 2009. Texas Water Resources Institute. 2011.
77. USDA Soil Conservation Service. National engineering handbook, section 4: Hydrology. Washington, DC. 1972.
78. Green, W. H., & Ampt, G. A. Studies on Soil Phyics. The Journal of Agricultural Science, 1911. 4(1), 1-24.
79. Williams, J. R., Kannan, N., Wang, X., Santhi, C., & Arnold, J. G. Evolution of the SCS runoff curve number method and its application to continuous runoff simulation. Journal of Hydrologic Engineering, 2012. 17(11), 1221-1229.
80. Mishra, S. K., & Singh, V. Soil conservation service curve number (SCS-CN) methodology (Vol. 42). Springer Science & Business Media. 2003.
81. McNaughton, K. G., & Jarvis, P. G. Using the Penman-Monteith equation predictively. Agricultural Water Management, 1984. 8(1-3), 263-278.
82. Widmoser, P. A discussion on an alternative to the Penman–Monteith equation. Agricultural Water Management, 2009. 96(4), 711-721.
83. Arnold, J. G., Moriasi, D. N., Gassman, P. W., Abbaspour, K. C., White, M. J., Srinivasan, R., ... & Jha, M. K. SWAT: Model use, calibration, and validation. Transactions of the ASABE, 2012. 55(4), 1491-1508.
84. Rostamian, R., Jaleh, A., Afyuni, M., Mousavi, S. F., Heidarpour, M., Jalalian, A., & Abbaspour, K. C. Application of a SWAT model for estimating runoff and sediment in two mountainous basins in central Iran. Hydrological sciences journal, 2008. 53(5), 977-988.
85. Moriasi, D. N., Arnold, J. G., Van Liew, M. W., Bingner, R. L., Harmel, R. D., & Veith, T. L. Model evaluation guidelines for systematic quantification of accuracy in watershed simulations. Transactions of the ASABE, 2007. 50(3), 885-900.

86. Singh, J., Knapp, H.V., & Demissie, M. Hydrologic Modeling of the Iroquois River Watershed Using HSPF and SWAT. Illinois Department of Natural Resources and the Illinois State Geological Survey. Illinois State Water Survey Contract Report 2004-08. 2004.
87. Gupta, H. V., Sorooshian, S., & Yapo, P. O. Status of automatic calibration for hydrologic models: Comparison with multilevel expert calibration. Journal of hydrologic engineering, 1999. 4(2), 135-143.
88. Moore, I. D., Gessler, P. E., Nielsen, G. A. E., & Peterson, G. A. Soil attribute prediction using terrain analysis. Soil science society of america journal, 1993. 57(2), 443-452.
89. Lee, K. T., & Ho, J. Y. Prediction of landslide occurrence based on slope-instability analysis and hydrological model simulation. Journal of Hydrology, 2009. 375(3-4), 489-497.
90. Ho, J. Y., Lee, K. T., Chang, T. C., Wang, Z. Y., & Liao, Y. H. Influences of spatial distribution of soil thickness on shallow landslide prediction. Engineering Geology, 2012. 124, 38-46.
91. Olyphant, J., Pelletier, J. D., & Johnson, R. Topographic correlations with soil and regolith thickness from shallow-seismic refraction constraints across upland hillslopes in the Valles Caldera, New Mexico. Earth Surface Processes and Landforms, 2016. 41(12), 1684-1696.
92. Cardoso de Salis, H. H., Monteiro da Costa, A., Moreira Vianna, J. H., Azeneth Schuler, M., Künne, A., Sanches Fernandes, L. F., & Leal Pacheco, F. A. Hydrologic modeling for sustainable water resources management in urbanized karst areas. International journal of environmental research and public health, 2019. 16(14), 2542.
93. Baum, R. L., Savage, W. Z., & Godt, J. W. TRIGRS: A Fortran program for transient rainfall infiltration and grid-based regional slope-stability analysis, version 2.0., Open-File Report 2008–1159, Reston, VA: US Geological Survey, 2008.
94. Iverson, R. M. Landslide triggering by rain infiltration. *Water Resources Research*, 2000, 36(7), 1897-1910.
95. Jibson, R. W. Landslide hazards at La Conchita, California (p. 12). US Department of the Interior, Open-File Report 2005-1067. US Geological Survey. 2005.
96. Godt, J. W., Baum, R. L., Savage, W. Z., Salciarini, D., Schulz, W. H., & Harp, E. L. Transient deterministic shallow landslide modeling: requirements for susceptibility and hazard assessments in a GIS framework. *Engineering Geology*, 2008, 102(3-4), 214-226.
97. Ciurleo, M., Ferlisi, S., Foresta, V., Mandaglio, M. C., & Moraci, N. Landslide susceptibility analysis by applying TRIGRS to a reliable geotechnical slope model. *Geosciences*, 2021, 12(1), 18.
98. Zhang, S., Jiang, Q., Xu, X., Tao, G., Zhang, Z., Gao, X., & He, C. Influence of soil mechanical and hydraulic parameters on the definition of rainfall intensity and duration thresholds based on transient rainfall infiltration and grid-based regional slope-stability model (TRIGRS). *Frontiers in Earth Science*, 2022, 10, 971655.

99. Liao, Z., Hong, Y., Kirschbaum, D., Adler, R. F., Gourley, J. J., & Wooten, R. Evaluation of TRIGRS (transient rainfall infiltration and grid-based regional slope-stability analysis)'s predictive skill for hurricane-triggered landslides: A case study in Macon County, North Carolina. Natural Hazards, 2011, 58, 325-339.
100. Hsu, Y. C., & Liu, K. F. Combining TRIGRS and DEBRIS-2D models for the simulation of a rainfall infiltration induced shallow landslide and subsequent debris flow. Water, 2019, 11(5), 890.
101. Yang, L., Cui, Y., Xu, C., & Ma, S. Application of coupling physics-based model TRIGRS with random forest in rainfall-induced landslide-susceptibility assessment. *Landslides*, 2024, 1-15.
102. Abbas, J. M. Slope stability analysis using numerical methods. *Journal of Applied Sciences*, 2014, 14(9), 846-859.
103. Sungkar, M., Munirwansyah, M., Munirwan, R. P., & Safrina, D. (2020). Slope stability analysis using Bishop and finite element methods. In IOP conference series: materials science and engineering, 2020, 933(1), 012035. IOP Publishing.
104. Brezinski, D. K., Adams, R. K., & Sylvia, E. R. (2020). Allegany County highway rock cut inventory and slope failure potential. Maryland. State Highway Administration. SPR-B Final Report (May 14, 2018-May 11, 2020), DNR Publication No. DNR 12-041720-227.
105. O'Malley, E. S., Saunders, S. A., & Ecker, J. J. (2004). Slope rehabilitation at the Baltimore-Washington Parkway with rammed aggregate piers. Transportation research record, 1874(1), 136-146.
106. Winter, M.G., & Bromhead, E.N. Landslide risks: some issues that determine societal acceptance. Natural Hazards, 2012, 62, 169-187.
107. Winter M.G., Shearer B., Palmer, D., Peeling D., Harmer, C. & Sharpe J. The Economic Impacts of Landslides and Floods on the Road Network. Procedia Engineering. 2016.
108. Galbraith, R.M., Price, D.J., & Shackman, L. (Eds). Scottish road network climate change study, 2005. 100p. Scottish Executive, Edinburgh.
109. Anon., Scottish road network climate change study: UKCP09 update. Transport Scotland. Edinburgh. 2011. (https://www.transport.gov.scot/.)
110. Winter, M.G., Dent, J., Macgregor, F., Dempsey, P., Motion, A., & Shackman, L. Debris flow, rainfall, and climate change in Scotland. Quarterly Journal of Engineering Geology and Hydrogeology, 2010, 43, 429-446.
111. Winter, M.G., & Shearer, B. Climate change and landslide hazard and risk – a Scottish perspective. Published Project Report PPR 650, 2013, Transport Research Laboratory, Wokingham.
112. Schuster, R.L. Socioeconomic significance of landslides. Landslides-Investigation and Mitigation. Transportation Research Board Special Report 247, 1996, 36-75. Washington, DC.
113. Highland, L.M. Estimating landslide losses- preliminary result of a seven-state pilot project. US Geological Survey Open File Report 2006-1032. 2006, USGS, Reston, VA.
114. Schuster, R.L., & Highland, L.M. (2007). The Third Hans Cloos Lecture.

Urban landslides: socioeconomic impacts and overview of mitigative strategies. Bulletin of Engineering Geology and the Environment, 66, 1-27.

115. Klose, M., Damn, B. & Terhorst, B. Landslide cost modelling for transportation infrastructures: a methodological approach. *Landslides*, 2015, 12, 321-334.

116. Highland, L.M. Landslides in Colorado, USA: impacts and loss estimation for the year 2010. US Geological Survey Open File report 2012-1204. , 2012, USGS, Reston, VA.

117. Porter M., Hove, J.V., Barlow, P., Froese, C., & Bunce, C. The Estimated Economic Impacts of Prairie Landslides in Western Canada. 2019, GEO St Johns'.

118. Schuster, R.L. & Highland, L.M. Socioeconomic and Environmental Impacts of Landslides in the Western hemisphere. U.S. Geological Survey, 2001.

119. Krohn, J.P., and Slosson, J. E. Landslide potential in the United States: California Geology, 1976, 29(10), 224-231.

120. Jahns, R.H. Landslides, in Geophysical predictions: National Academy of Sciences,1978, 58-65.

121. Walkinshaw, J. Landslide correction costs on US state highway systems. Transportation Research Record, 1992, 36-36.

122. Duranton, G., Nagpal, G., & Turner, M. Transportation Infrastructure in the US (No. c14352). National Bureau of Economic Research. 2020.

123. Srinivasan, H. U.S. Inflation Rate by Year: 1929 to 2024. n/a, n/a, United States of America, 2024.

124. Fleming, R. W., & Taylor, F. A. Estimating the costs of landslide damage in the United States (Vol. 832). US Department of the Interior, Geological Survey. 1980

125. Slosson, J. E., and Krohn, J. P., AEG building code review -- Mudflow/debris flow damage. February 1978 storm -- Los Angeles area: California Geology, 1979, 32(1), 8-11.

126. Hammond, C.M. Meyer, M.R., Vessely, D.A, Machan, G., & Black B.A. How Much Can it Cost to Remediate a Large Landslide? Theme Session No. 10, GSA Cordilleran Sec. Mtg. 2002.

127. Mirus, B. B., Jones, E. S., Baum, R. L., Godt, J. W., Slaughter, S., Crawford, M. M., ... McCoy,K. M. Landslides across the USA: occurrence, susceptibility, and data limitations. Landslides 2020, 17.

128. Schuster, R. L. & Krizek, R. J. Special Report 176; Landslides: Analysis and Control, 1978, TRB, National Research Council, Washington D.C.

129. Lukashov, S. G., Lancaster, J. T., Oakley, N. S., & Swanson, B. J. Post-fire debris flows of 9 January 2018, Thomas Fire, southern California: Initiation areas, precipitation and impacts. Association of Environmental and Engineering Geologists; special publication 28. 2019.